Supporting Information

Enhancing the Photocatalytic Upcycling of Polystyrene to Benzoic Acid: A Combined Computational-Experimental Approach for Acridinium Catalyst Design

Albert Ong [a]‡, Zi Cheng Wong[b]‡, Kang Le Osmund Chin[c], Wei Wei Loh[a], Ming Hui Chua[c]*, Shi Jun Ang[b,c]*, Jason Y.C. Lim[a,d]*

---

[a] Institute of Materials Research and Engineering (IMRE)
Agency for Science, Technology and Research (A*STAR)
2 Fusionopolis Way, Innovis #08-03, Singapore 138634
Republic of Singapore
E-mail: jason_lim@imre.a-star.edu.sg

[b] Institute of High Performance Computing (IHPC)
Agency for Science, Technology and Research (A*STAR)
1 Fusionopolis Way, Connexis, #16-16, Singapore 138632
Republic of Singapore
Email: ang_shi_jun@ihpc.a-star.edu.sg

[c] Institute of Sustainability for Chemicals, Energy and Environment (ISCE2)
Agency for Science, Technology and Research (A*STAR)
1 Pesek Road, Jurong Island, Singapore 627833
Republic of Singapore
Email: chua_ming_hui@isce2.a-star.edu.sg

[d] Department of Materials Science and Engineering
National University of Singapore (NUS)
9 Engineering Drive 1, Singapore 117576
Republic of Singapore

This document contains 55 pages with 83 figures and 7 tables.

Table of Contents

S1. Materials and Instrumentation

All reagents were purchased from commercial sources and used without further purification unless stated otherwise. Polystyrene (PS, M_n ~140 kDa, M_w ~230 kDa), 1,2-Dichloroethane (DCE, ≥ 99%), Acetonitrile (MeCN, 99.8%), Tetrahydrofuran (THF, anhydrous, ≥99.9%, inhibitor-free), N,N-Dimethylformamide (DMF, anhydrous, 99.8%), 1,3,5-Trimethoxybenzene (TMB, ≥ 99%), 9-Mesityl-10-methylacridinium tetrafluoroborate (**Mes-Acr-Me**), Hydrochloric acid (~37% in H_2O), Hydrobromic acid (~47% in H_2O), Tetrabutylammonium chloride (TBACl, ≥97.0%), 9(10H)-Acridone (99%), 10-Phenyl-9(10H)-acridone (95%), Copper(I) iodide (≥99.5%), Ammonium chloride (NH$_4$Cl,≥99.5%), Potassium carbonate (K$_2$CO$_3$,≥99.0%), 4-Fluorophenylmagnesium bromide solution (1.0 M in THF) and 2-Bromonaphthalene (97%) were all purchased from Sigma-Aldrich. Dipivaloylmethane (97.0+%) were sourced from Tokyo Chemical Industry (TCI). Tetrafluoroboric acid-diethyl ether complex (50-55% w/w HBF$_4$) were sourced from Alfa Aesar. Diethyl ether (≥98%), Hexane (95%), Dichloromethane (DCM, ≥99.5%), Ethyl acetate (EA, 99.9%) were sourced from J.T. Baker. Chloroform-d (CDCl$_3$, 99.5%), Methylene Chloride-d (CD$_2$Cl$_2$, 99.8%) were purchased from Cambridge Isotope Laboratories.

All PS commercial products were obtained from real-life plastic waste (SPI code 6). Black and clear cup lids were obtained from disposable cups, PS weighing boat was obtained from lab waste and commercial expanded polystyrene was obtained from commercial food packaging containers. All PS products were used after washing with water, without further purification and mechanical treatment other than cutting into smaller fragments such that they fit into the reaction tube.

^{1}H nuclear magnetic resonance (NMR) was recorded using a JEOL 500 MHz spectrometer (Tokyo, Japan) in CDCl$_3$, CD$_2$Cl$_2$. The chemical shift was recorded in ppm and the following abbreviations were used to explain the multiplicities: s = singlet, d = doublet, t = triplet, m = multiplet, br = broad. ESI mass was performed with 6200 series TOF/6500 series Q-TOF B.09.00 (B9044.1 SP1). Gel permeation chromatography (GPC) was performed in THF using the Agilent 1260 Infinity II GPC/SEC System with refractive index detector and calibration was performed using monodisperse polystyrene standards. UV-visible absorption spectra were recorded with Shimadzu UV-2501 spectrophotometer (Kyoto, Japan) over the wavelength range of 200 to 600 nm. Fluorescence emission and excitation spectra were recorded with Shimadzu RF-5301 spectrofluorophotometer (Kyoto Japan). Cyclic voltammetry experiments were performed in dry solvents (DCE or MeCN) with a Metrohm Autolab PGSTAT128N potentiostat/ galvanostat with a three-electrode cell, using 0.1 M tBu$_4$NPF$_6$ as supporting electrolyte, AgCl/Ag as reference electrode, glassy carbon as working electrode, and Pt wire as counter electrode. The potential was externally calibrated against the ferrocene/ferrocenium (F$_c$/F$_c^+$) couple.

S2. Methods and Procedures

Synthesis of Acridinium catalyst

Different acridinium catalysts were synthesised based on the procedure as shown in **Scheme S1** (**FPh-Acr-Np** was shown as an example).
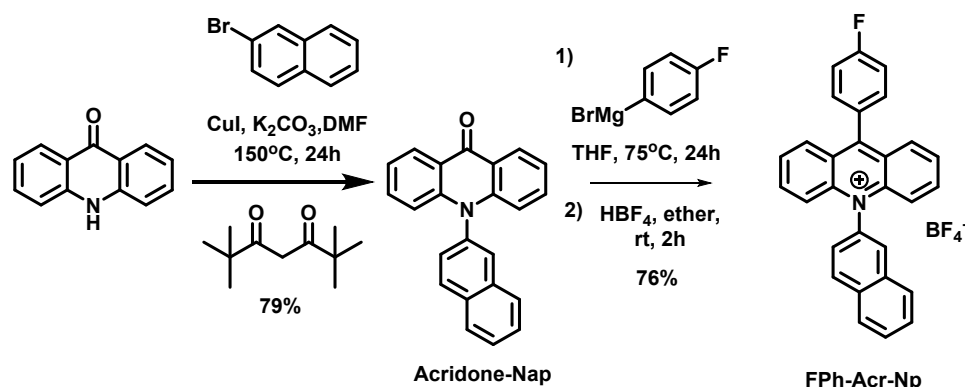
Scheme S1: Synthesis route of **FPh-Acr-Np**

The products were characterised by ^{1}H, ^{13}C, ^{19}F NMR spectroscopy (if applicable) and ESI high resolution mass spectroscopy.

General procedure for Ullmann coupling of acridone (Acridone-Nap was shown as an example).

9(10H)-Acridone (390 mg, 2 mmol), 2-bromonapthalene (415 mg, 2 mmol), K_2CO_3 (690 mg, 5 mmol), and CuI (19 mg, 0.1 mmol) was added to a 100 mL Schleck flask. The reaction vessel was then evacuated by applying vacuum and was refilled with Ar gas 3 times. Dipivaloylmethane (75 μL, 0.36 mmol) and anhydrous DMF (10 mL) was added to the reaction mixture and was heated at 150 °C for 24 h in the sealed Schleck flask. The resulting mixture was dried under reduced pressure and was subjected to a silica column using DCM/hexane (1:1) mixture as the eluent. The product was dried under reduced pressure to obtain **Acridone-Nap** as a pale-yellow solid (507 mg, 79 % yield). ^{1}H NMR (500 MHz, CDCl$_3$) δ 8.64 – 8.62 (m, 2H), 8.20 – 8.18 (d, 1H), 8.06 – 8.04 (d, 1H), 7.94 – 7.92 (m, 2H), 7.70 – 7.63 (m, 2H), 7.49 – 7.46 (m, 2H), 7.43 – 7.41 (m, 1H), 7.31 – 7.28 (m, 2H), 6.81– 6.79 (d, 2H);^{13}C NMR (125 MHz, CDCl3) δ178.71, 143.74, 136.63, 134.79, 133.83, 133.79, 131.93, 129.75, 128.69, 128.57, 128.10, 127.82, 127.75, 127.54, 122.34, 122.08, 117.42; HR-MS (ESI): calc. for $C_{23}H_{16}NO$ [M+H]: 321.1154, found: 321.1142 (error: 0.0012 ppm).

General procedure for nucleophilic reaction on acridone (FPh-Acr-Np was shown as an example).

100 mL two-neck round bottom flask with a stirring bar was attached with a condenser and flame-dried under vacuum. The reaction vessel was cooled to ambient temperature and was filled with Ar (g). **Acridone-Nap** (500 mg, 1.55 mmol) and anhydrous THF (20 mL) was then added under inert conditions. 4-Fluorophenylmagnesium bromide solution (1M in THF) (6 mL) was added dropwise with a syringe, and the reaction mixture was heated to reflux for 24 h under inert conditions. After 24 h, the reaction was cooled ambient temperature and then quenched with aqueous NH$_4$Cl. The mixture was extracted with EA and the combined organic layer dried under reduced pressure. The crude mixture was purification via flash column chromatography with neutral alumina column and pure EA as eluent. The combined solution was dried under reduced pressure to obtain a pale-yellow oil. The crude pale-yellow oil was dissolved in diethyl ether (20 mL) with stirring. HBF$_4$ (50 % in ether) (0.9 mL, 3.1 mmol) was added dropwise, and yellow precipitation can be observed. The mixture was stirred for 2 h in room temperature. After 2 h, the reaction was filtered and the residue solid was washed with diethyl ether, collected, and dried to obtain **FPh-Acr-Np** as a bright yellow solid (573 mg, 76 %). $λ_{max}$ in DCE: 437 nm; Ɛ in DCE: 0.647 x 10^4 M^{-1} cm^{-1}; ^{1}H NMR (500 MHz, CD$_2$Cl$_2$) δ 8.42 – 8.49 (m, 1H), 8.21 – 8.10 (m, 7H), 7.88 – 7.79 (m, 4H), 7.68 – 7.62 (m, 5H), 7.54 – 7.52 (m, 2H) ;^{13}C NMR (125 MHz, CD$_2$Cl$_2$) δ163.23, 162.51, 142.37, 138.84, 134.32, 134.10, 133.70, 132.38, 132.32, 130.02, 129.09, 128.75, 128.62, 128.62, 128.45, 128.33, 127.72, 126.29, 123.98; ^{19}F NMR (470 MHz CD$_2$Cl$_2$) δ -109.61 − -109.67, -153.36, -153.41; HR-MS (ESI): calc. for $C_{29}H_{19}FN$ [M]$^+$: 400.1496, found: 400.1506 (error: 0.0010 ppm).

Ph-Acr-Ph (Synthesized from commercial 10-Phenyl-9(10H)-acridone) Yield: 86 %. $λ_{max}$ in DCE: 434 nm; Ɛ in DCE: 0.450 x 10^4 M^{-1} cm^{-1}; ^{1}H NMR (500 MHz, CDCl$_3$) δ 8.10 – 8.06 (m, 4H), 7.90 – 7.86 (*m*, 3H), 7.78 – 7.70 (*m*, 9H), 7.56 – 7.55 (*d*, 2H). ^{13}C NMR (125 MHz, CDCl$_3$) δ 165.67, 163.17, 162.90, 142.77, 138.60, 137.78, 132.87, 132.78, 132.21, 132.94, 130.47, 129.57, 128.69, 128.22, 126.99, 120.18, 116.89. ^{19}F NMR (470 MHz, CDCl$_3$) δ -154.58, -154.63. HR-MS (ESI): caldc for $C_{25}H_{18}N$ [M]$^+$: 332.1434, found: 332.1428 (error: 0.0006 ppm).

Ph-Acr-Me: (Synthesized from commercial 10-Methyl-9(10H)-acridone) Yield: 89 %. $λ_{max}$ in DCE: 430 nm; Ɛ in DCE: 0.432 x 10^4 M^{-1} cm^{-1}; ^{1}H NMR (500 MHz, CDCl$_3$) δ 8.76 – 8.74 (*d*, 2H), 8.40 – 8.37 (*t*, 2H), 8.01 – 7.99 (*d*, 2H), 7.81 – 7.78 (*m*, 2H), 7.74 – 7.70 (*m*, 3H), 7.50 – 7.48 (*m*, 2H), 5.05 (*s*, 3H). ^{13}C NMR (125 MHz, CDCl$_3$) δ 161.88, 142.19, 139.67, 133.54, 130.93, 130.61, 130.38, 129.50, 128.36, 126.58, 119.51, 66.34. ^{19}F NMR (470 MHz, CDCl$_3$) δ −153.06, −153.11. HR-MS (ESI): caldc for C20H16FN [M-BF4]: 270.1277, found: 270.1273 (error: 0.0004 ppm).

MeOPh-Acr-Ph: (Synthesized from commercial 10-Phenyl-9(10H)-acridone) Yield: 93%. $λ_{max}$ in DCE: 454 nm; Ɛ in DCE: 1.051 x 10^4 M^{-1} cm^{-1}; ^{1}H NMR (500 MHz, CD$_2$Cl$_2$) δ 8.26 – 8.24 (*dd*, 2H), 8.16 – 8.13 (*m*, 2H), 7.95 − 7.93 (*m*, 3H), 7.87 − 7.83 (*m*, 2H), 7.60 – 7.56 (*m*, 6H), 7.32 – 7.30 (*d*, 2H), 4.01 (*s*, 3H). ^{13}C NMR (125 MHz, CDCl$_3$) δ 164.23, 162.00, 142.60, 138.72, 137.62, 132.59, 132.26, 132.06, 130.87,

128.54, 128.17, 126.79, 125.36, 120.03, 115.03, 56.15. ^{19}F NMR (470 MHz, CDCl$_3$) δ -154.59, -154.64. HR-MS (ESI): caldc for C26H20NO [M-BF4]: 362.1539, found: 362.1529 (error: 0.0010 ppm).

The characterisation data of **Ph-Acr-Ph**,[1] **Ph-Acr-Me**[1] and **MeOPh-Acr-Ph**[2] matches those previously reported.

Mes-Acr-Me: (From Sigma Aldrich) $λ_{max}$ in DCE: 429 nm; ℇ in DCE: 0.527 x 10^4 M^{-1} cm^{-1}

Reaction Set-up for Photoredox PS Degradation

390 nm (max 52 W) 440 nm (max 45 W) LEDs used were purchased from Kessil PR160L series. The specifications for the lights are as follows: Beam Angle of 56 °. A model experimental setup is shown in **Figure S1**.
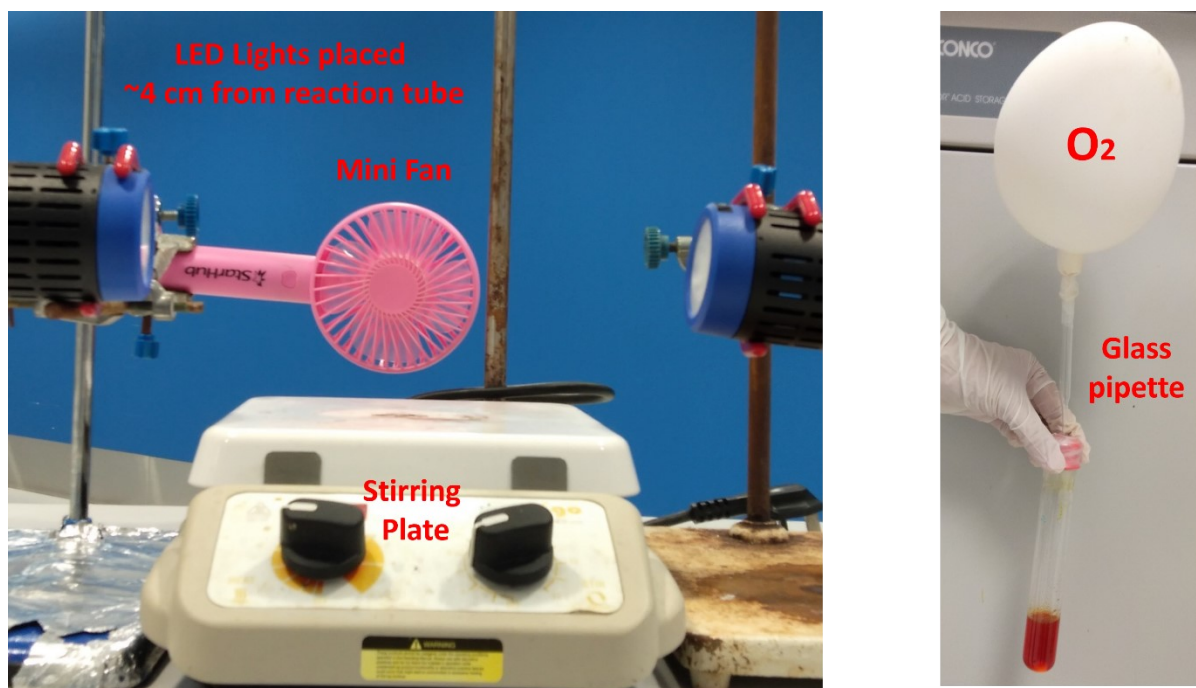
Figure S1: (Left) Model experimental setup used. Lights were placed at ~ 4 cm from the reaction tube and was set to the maximum intensity. A small fan was left on throughout the whole reaction to maintain the reaction at near-ambient temperature (~35 ± 1 °C). (Right) Image of the reaction tube. O$_2$ at 1 atmospheric pressure (not a flow of O$_2$) was supplied to the reaction vessel with a balloon connected by a glass pipette. A glass pipette was used rather than a stainless steel needle due to the presence of HCl within the reaction vessel, to avoid inadvertent contamination of the reaction from corrosion of the needle.
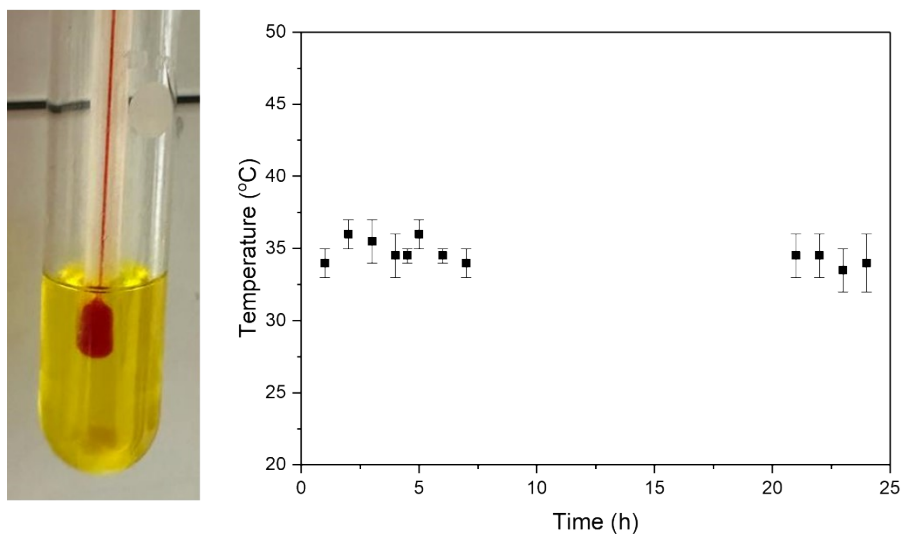
Figure S2: (Left) Reaction set-up to measure the temperature of the reaction solution. (Right) Recorded temperature at constant time intervals (values presented is an average of two different experiments). The temperature increases from the initial room temperature (~23 °C) to ~34 ± 1 °C within the first hour. After that, the temperature was maintained constantly at ~35 ± 1 °C

General Procedure for the aerobic degradation of PS products

1 mmol (styrene repeating unit) of PS beads (104 mg) and appropriate quantities of acridinium catalyst (0.10 mmol) were added to a 10 mL Schleck tube with a stirring bar. The atmosphere within the reaction tube was evacuated and refilled with O_2 using a balloon. 6 mL of DCE, 1 mL of MeCN and appropriate quantities of aqueous HCl (~37%) (0.10 – 2 mmol) were added. The reaction tube was place in the experimental setup (see **Figure S1**) with an appropriate LED light (390 nm or 440 nm) and was stirred for 24 h without external heating under O_2 atmosphere. The atmosphere was maintained via an O_2 balloon while the temperature was maintained via a cooling fan (~35 ± 1 °C throughout the reaction). After 24 h, the reaction was dried under reduced pressure. The solid residue was collected, and the yield of benzoic acid was determined via ^{1}H NMR using CDCl$_3$ as the solvent and TMB as the internal standard.

Procedure for the aerobic degradation of commercial PS products using FPh-Acr-Np

1 mmol (styrene repeating unit) of commercial PS product (SPI code 6) (104 mg) and **FPh-Acr-Np** (24.4 mg, 0.05 mmol) were added to a 10 mL Schleck tube with a stirring bar. The atmosphere within the reaction tube was evacuated and refilled with O_2 using a balloon. 6 mL of DCE, 1 mL of MeCN and aqueous HCl (~37%) (140 µL, 2 mmol) were added. The reaction tube was place in the experimental setup (see **Figure S1**) with 390 nm LED light and was stirred for 24 h at near-ambient temperatures under O_2 atmosphere. The atmosphere was maintained via an O_2 balloon while the temperature was maintained via a cooling fan. After 24 h, the reaction was dried under reduced pressure. The solid residue was collected, and the yield of benzoic acid was determined via ^{1}H NMR using CDCl$_3$ as the solvent and TMB as the internal standard.

Yields of BA for the PS weighing boat and black cup lid in parentheses (**Figure 2Cii**) were obtained after determining the "actual amount" of PS content within the commercial products as additives were observed to be present in substantial amounts. The additives were observed to be insoluble in DCE. Hence, the PS content was determined via the following procedure:

500 mg of either PS weighing boat or black cup lid was dissolved thoroughly in 10 mL of DCE. The resulting solution was filtered through celite and the celite layer was washed thoroughly with DCE. The

resulting filtrate was first vaporised under reduced pressure, then dried under in a vacuum oven at 60 °C overnight. The mass of the resulting PS solid obtained from PS weighing boat and black cup lid was determined to be 403 mg and 375 mg respectively.

The yields BA for the PS weighing boat and black cup lid in parentheses (**Figure 2Cii**) were determined via calculations as shown below:

$$Actual\ yield\ of\ benzoic\ acid\ (Weighing\ boat) = \frac{500}{403} \times 32.5\ \% = 40\ \%$$

$$Actual\ yield\ of\ benzoic\ acid\ (Black\ lid) = \frac{500}{375} \times 31.5\ \% = 42\ \%$$

S3. Further PS Oxidation Experiments

Table S1. Summary of reaction outcomes for acridinium-catalysed PS photoredox degradation
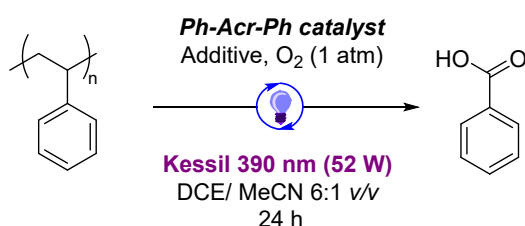
S/N	Catalyst (loading)	Additive (loading)	Deviation from conditions	BA yield/ %	M_n^b/ kDa	Spectra
1	**Ph-Acr-Ph** (10 mol%)	HCl (10 mol%)	Air (21 % O_2, 1 atm pressure) used instead of O_2	8	1.71	**Figure S24, S25**
2	**Ph-Acr-Ph** (10 mol%)	water (7 μL) [a]	-	17	1.41	**Figure S26, S27**
3	-	HCl (200 mol%)	-	6	3.01	**Figure S28, S29**
4	**Ph-Acr-Ph** (5 mol%)	HCl (200 mol%)	CHCl$_3$ used as solvent	36	0.47	**Figure S30, S31**
5	**Ph-Acr-Ph** (5 mol%)	HCl (200 mol%)	MeCN used as solvent	0	42.4	**Figure S32, S33**
6	**Ph-Acr-Ph** (5 mol%)	HCl (200 mol%)	DCE/MeCN 4:3 v/v	9	1.25	**Figure S34, S35**
7	**Ph-Acr-Ph** (5 mol%)	HCl (200 mol%)	EA/ DCE 1:1 v/v	20	0.58	**Figure S36, S37**
8	**Ph-Acr-Ph** (5 mol%)	TBACl (200 mol%)	-	0	6.90	**Figure S38, S39**
9	**Mes-Acr-Me** (5 mol%)	HCl (200 mol%)	-	18	0.54	**Figure S40, S41**
10	**MeOPh-Acr-Ph** (5 mol%)	HCl (200 mol%)	-	0	3.79	**Figure S42, S43**
11	**MeOPh-Acr-Ph** (5 mol%)	HCl (200 mol%)	440 nm irradiation used instead	0	3.76	**Figure S44, S45**

[a] An equivalent amount of deionised water as compared to 10 mol% HCl; [b] Determined by GPC analysis in THF against polystyrene standards. M_n of the PS starting material determined by GPC analysis is 42.7 kDa.

S4. Supporting Spectra

Characterization of products from PS

The compositions of the product mixture were analysed via ^{1}H NMR and yields were determined using TMB as the internal standard. The spectra generally contain a mixture of benzoic acid with peaks at δ (ppm): 7.45 − 7.49 (*t*), 7.59 − 7.64 (*t*), 8.08 − 8.11 (*d*)

The full spectrum for degraded expanded polystyrene mixture is shown as an example in **Figure S3**.

To quantify the yields of benzoic acid, TMB (50.4 mg, 0.3 mmol) was added to the dried crude reaction mixture as an internal standard. The mixture was then dissolved in CDCl$_3$ and was analysed by ^{1}H NMR. Typically, the relative integrations of peaks **(a)** and **(d)** were used for the yield calculation of benzoic acid. In the case of **Figure S3**,

$$Yield\ of\ benzoic\ acid = \frac{2.18}{2} \times 0.3 \times 100 = 33\ \%$$
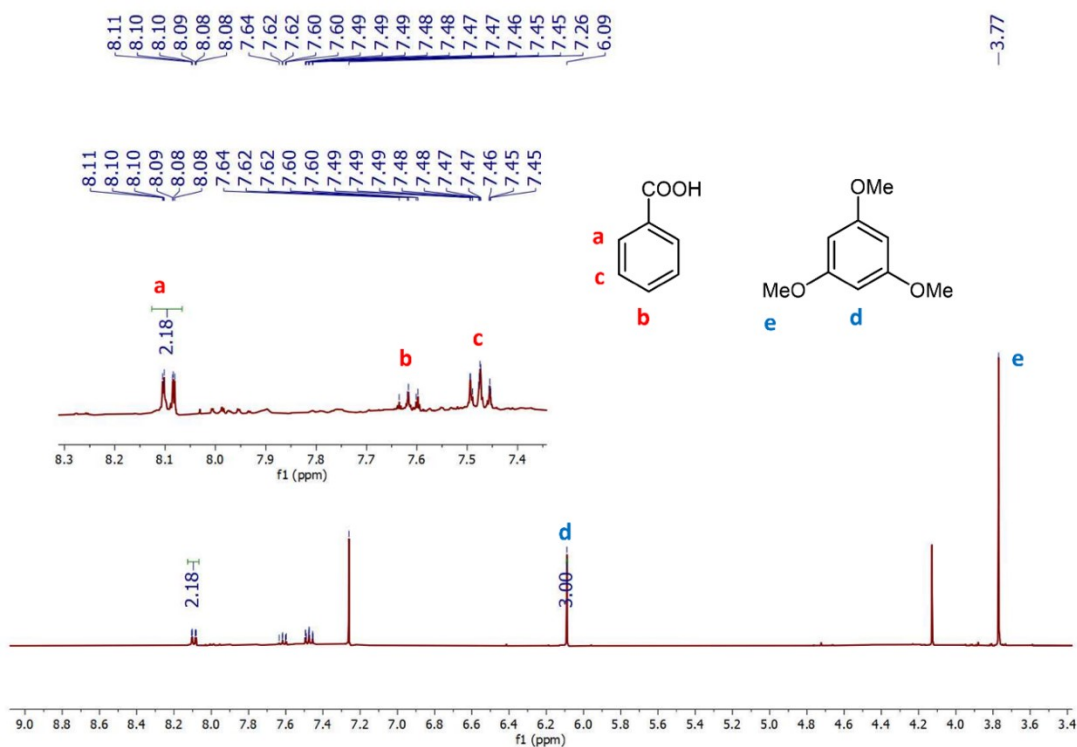
Figure S3. ^{1}H NMR spectrum of the crude reaction mixture of PS degradation catalysed by 10 mol% of **Ph-Acr-Ph** with 10 mol% of HCl (**Table 1, entry 1**) in CDCl$_3$. 0.3 mmol of TMB was added as the internal standard.
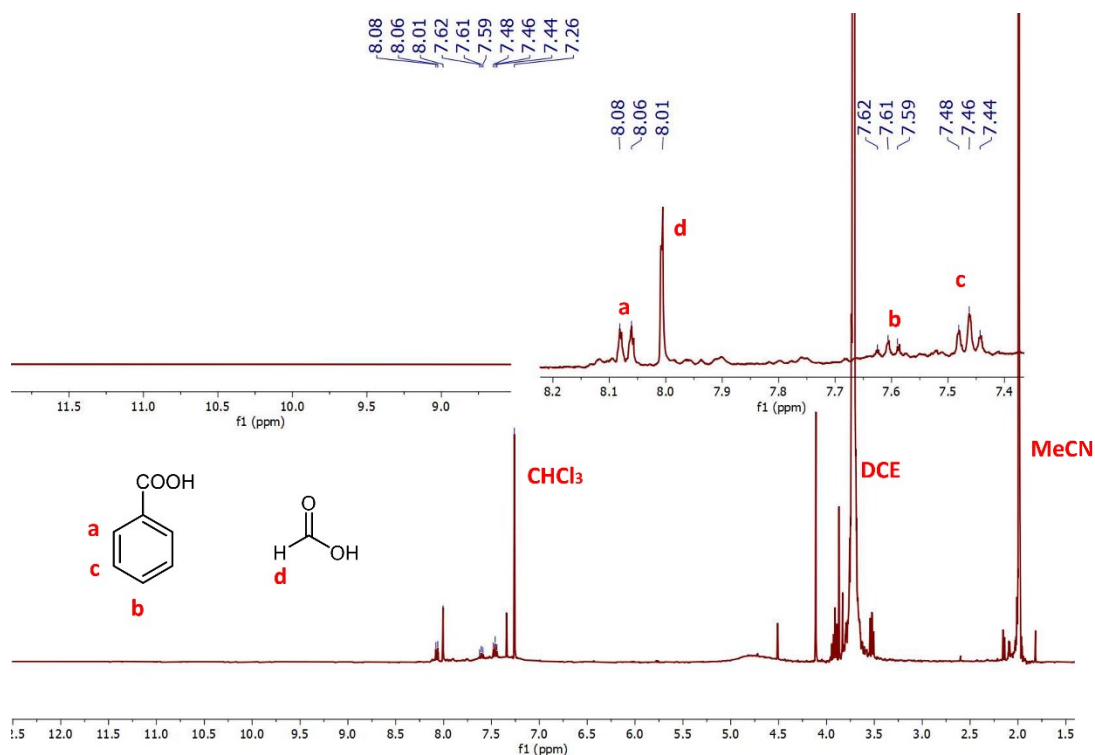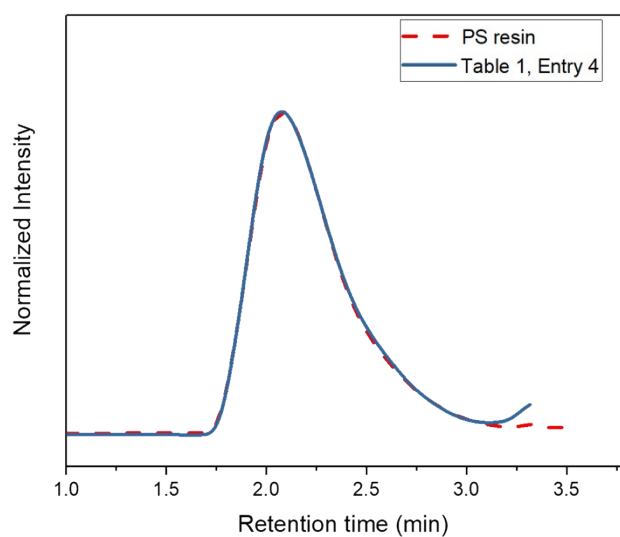
Figure S4. ^{1}H NMR spectrum of a sample of the crude reaction mixture of PS degradation catalysed by 10 mol% of **Ph-Acr-Ph** with 10 mol% of HCl (**Table 1, entry 1**), without removal of any of the volatiles from the reaction in CDCl$_3$. The presence of benzoic acid and formic acid are indicated in the spectrum.
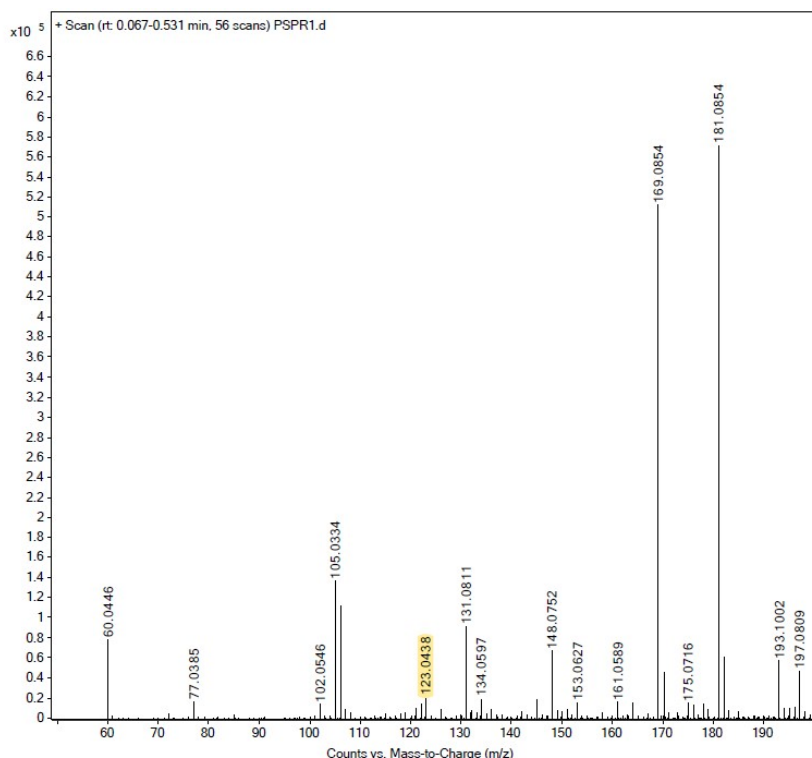
Figure S5. ESI-MS spectrum showing the unequivocal presence of benzoic acid formed under the catalytic conditions in **Table 1, entry 1**. [M+H] peak at m/z = 123.0438 (error: 0.0008 ppm). Postulated aromatic small molecules that are potentially present but not detectable by ^{1}H NMR are: benzaldehyde [M-H] peak at m/z = 105.0341 (error: 0.0007 ppm)
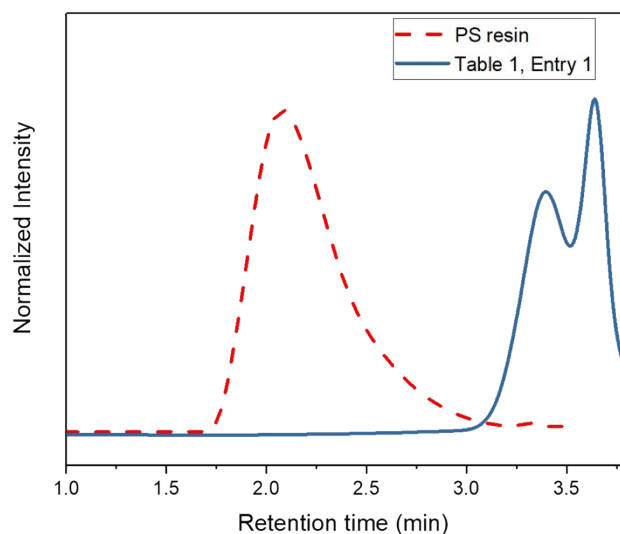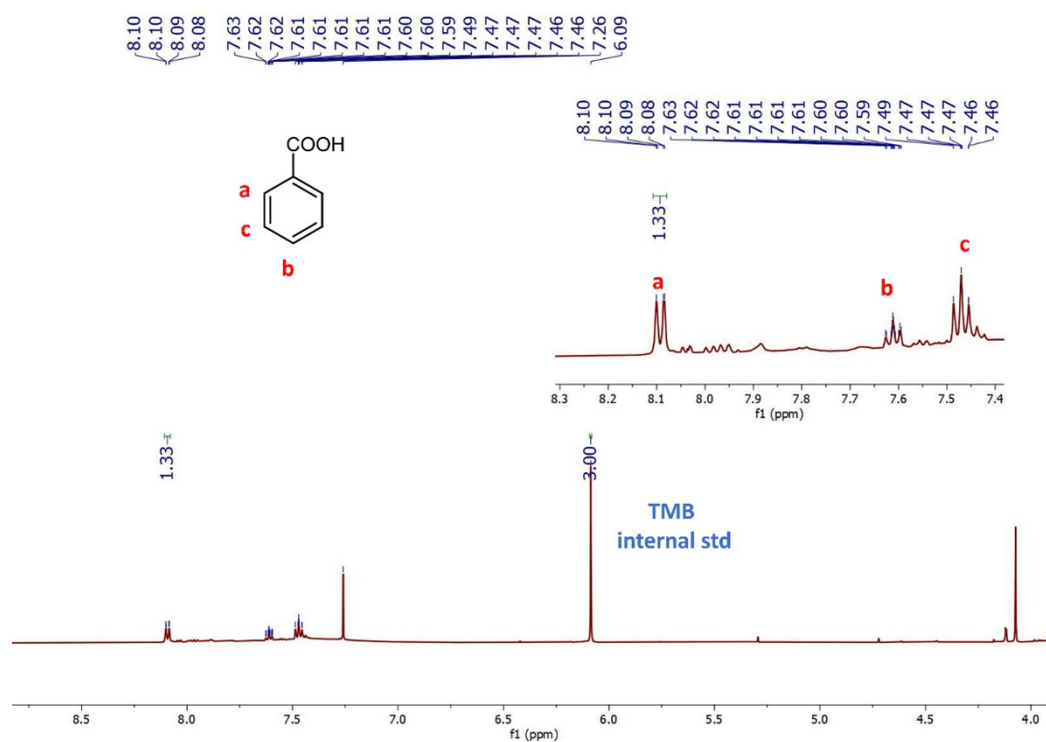
Figure S6. GPC chromatogram for the degraded PS catalysed by 10% mol of **Ph-Acr-Ph** in O_2 with 10% mol HCl (aq) (**Table 1, entry 1**).
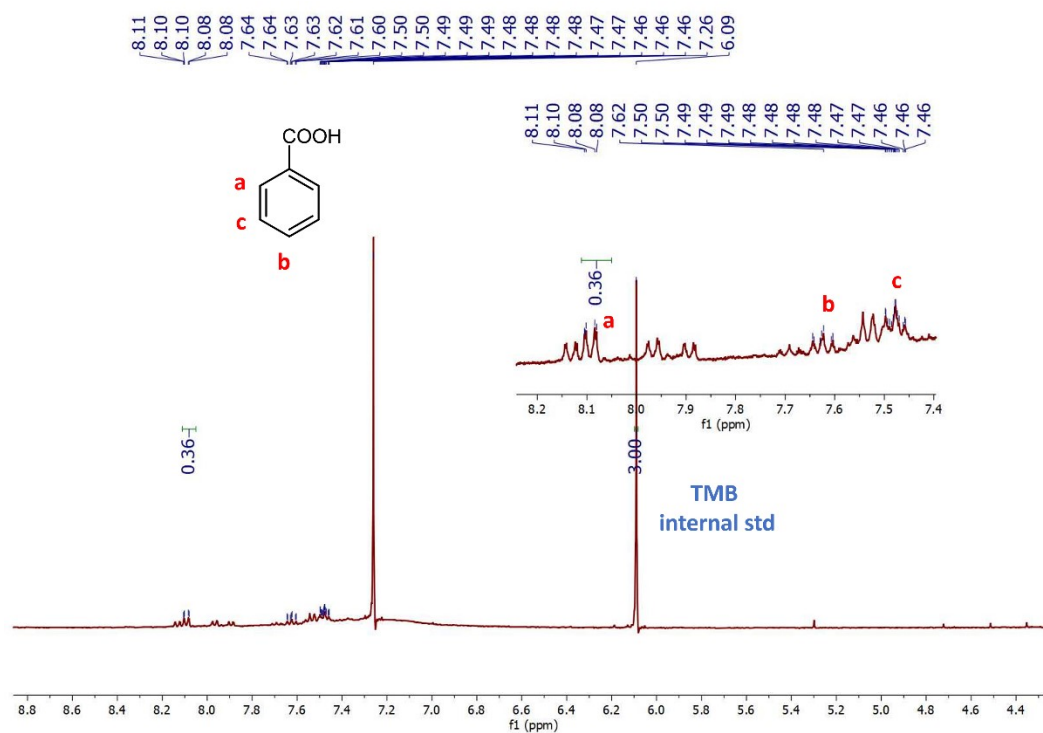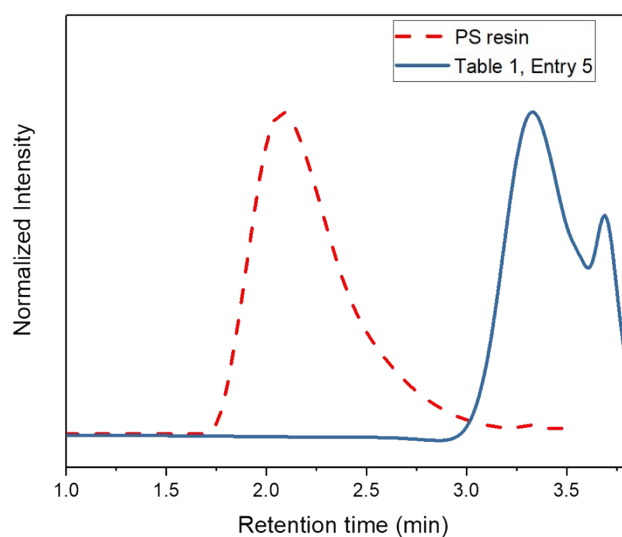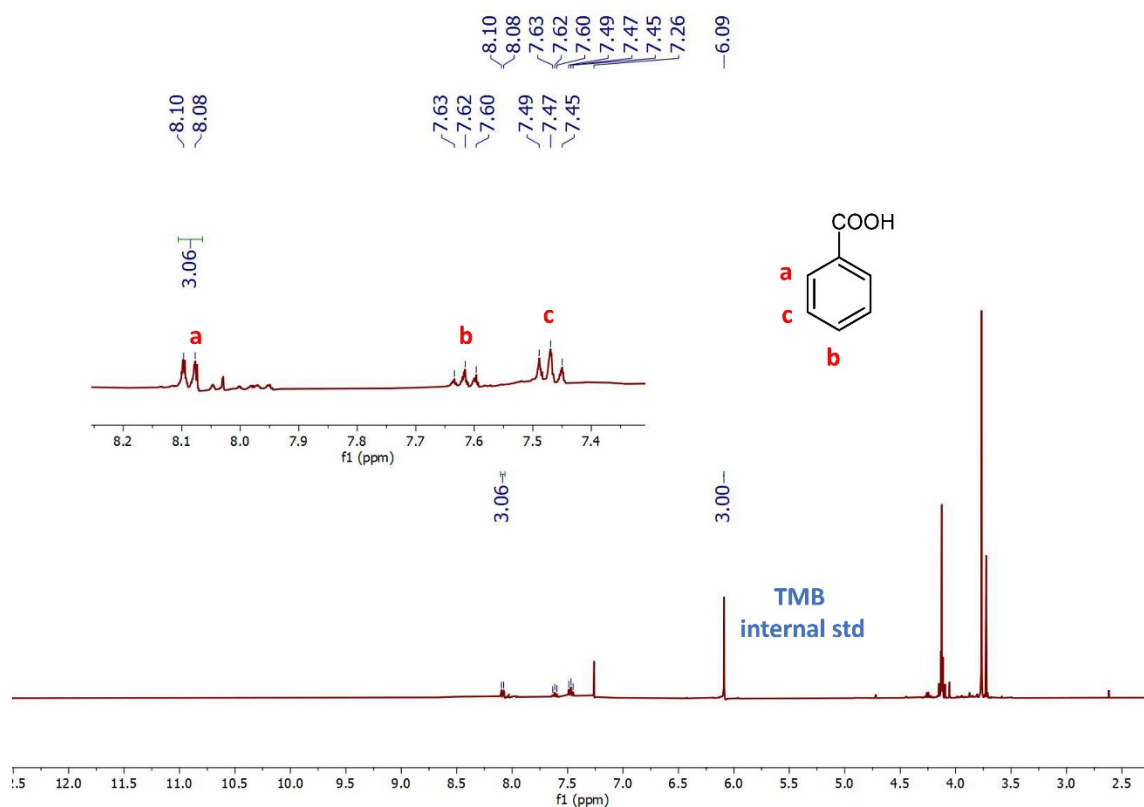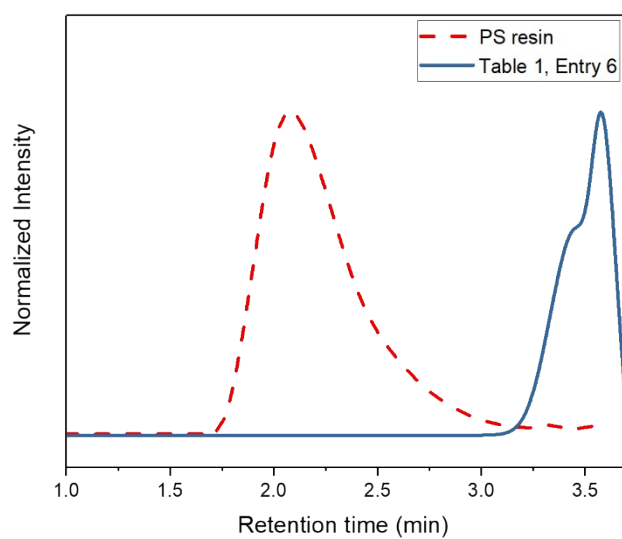

Figure S7. ^{1}H NMR spectrum of the crude reaction mixture of PS degradation with 10% mol of HCl (aq) in O_2 without any acridinium catalyst (**Table 1, entry 2**) in CDCl$_3$. 0.3 mmol of TMB was added as the internal standard.
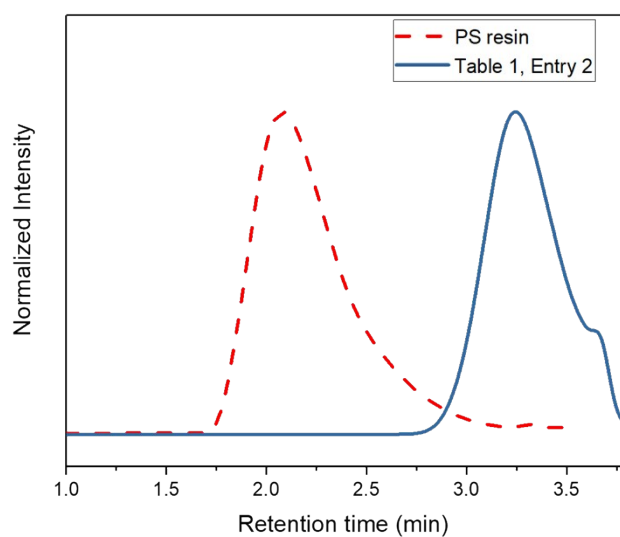
Figure S8. GPC chromatogram for the degraded PS in O_2 with 10% mol HCl (aq) without any acridinium catalyst (**Table 1, entry 2**).
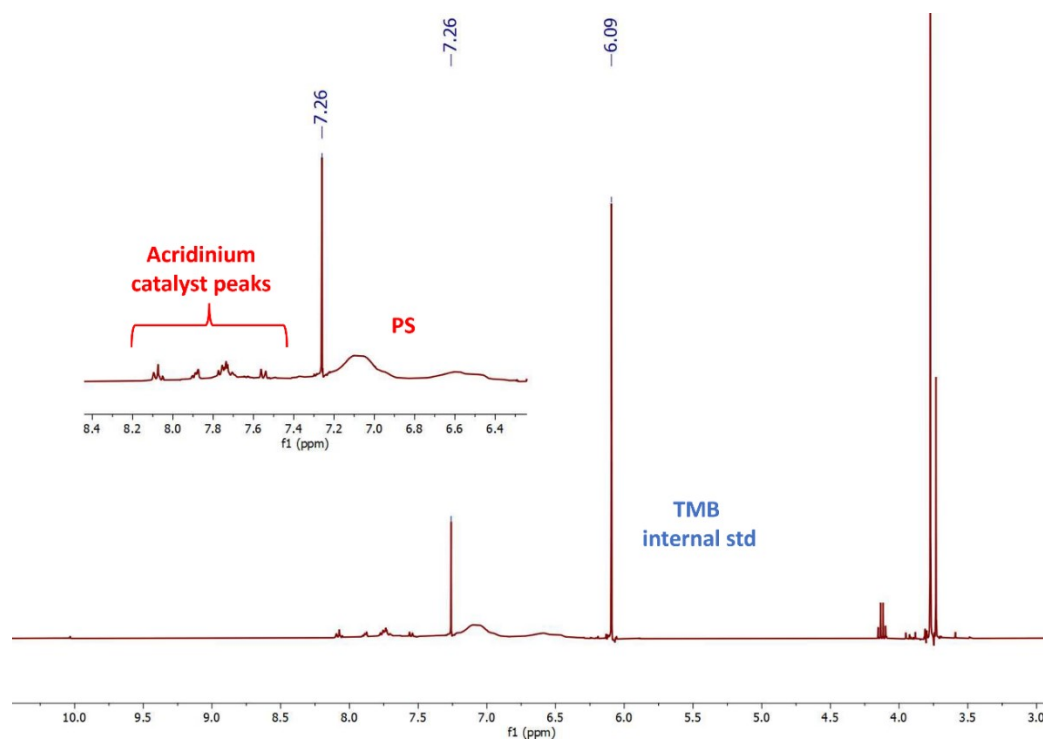
Figure S9. ^{1}H NMR spectrum of the crude reaction mixture of PS degradation catalysed by 10% mol of **Ph-Acr-Ph** in argon with 10% mol HCl (aq) (**Table 1, entry 3**) in CDCl$_3$. 0.3 mmol of TMB was added as the internal standard.
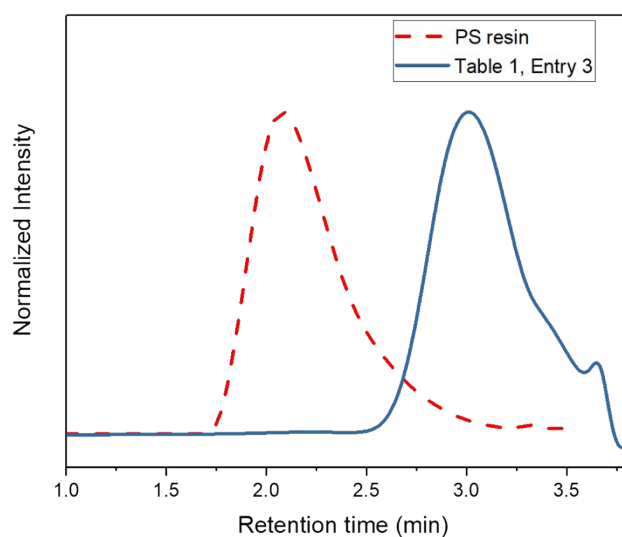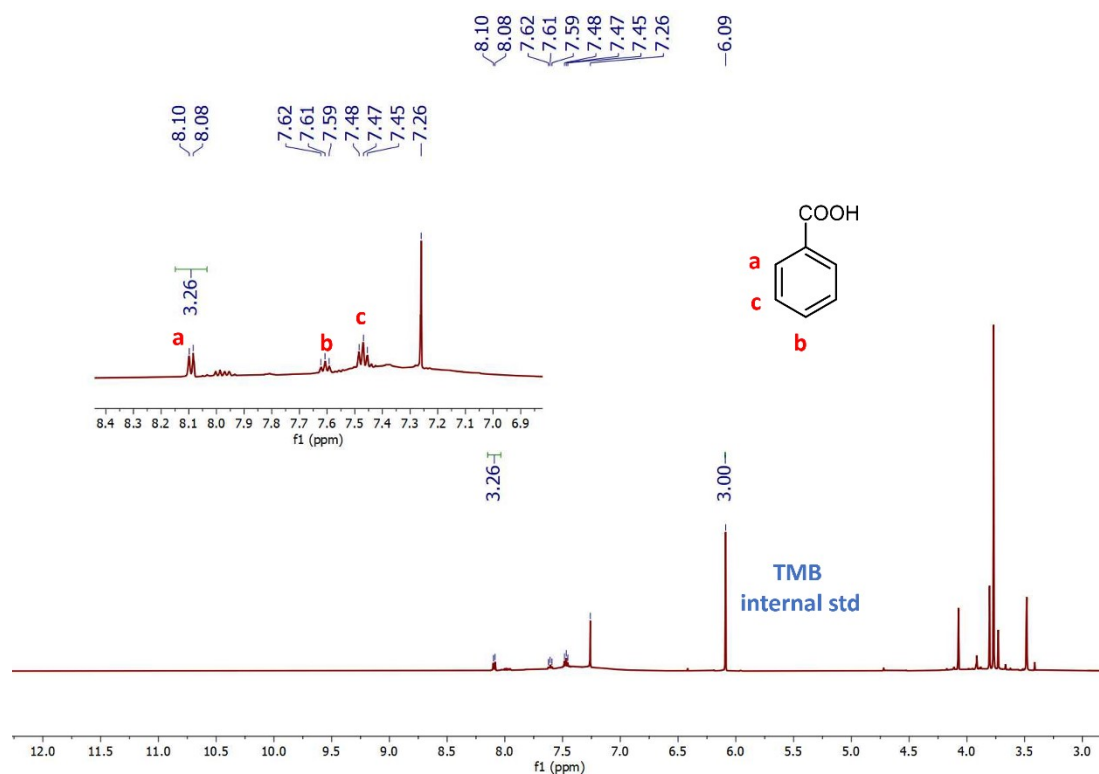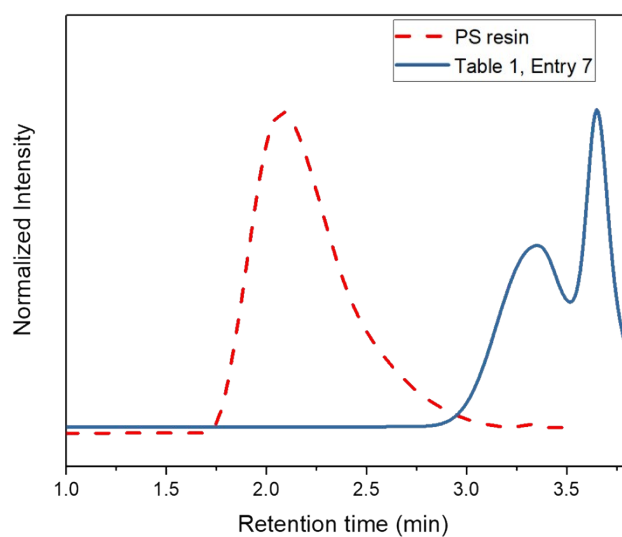
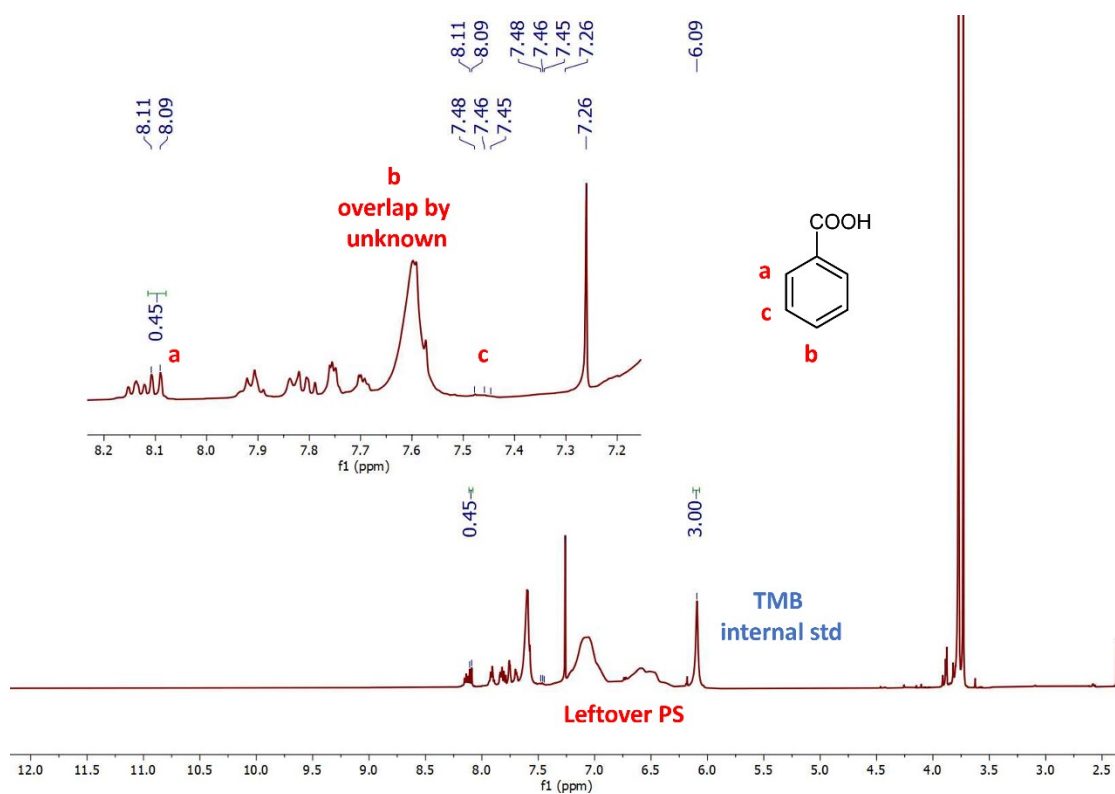**Figure S10.** GPC chromatogram for the degraded PS catalysed by 10% mol of **Ph-Acr-Ph** in argon with 10% mol HCl (aq) (**Table 1, entry 3**).
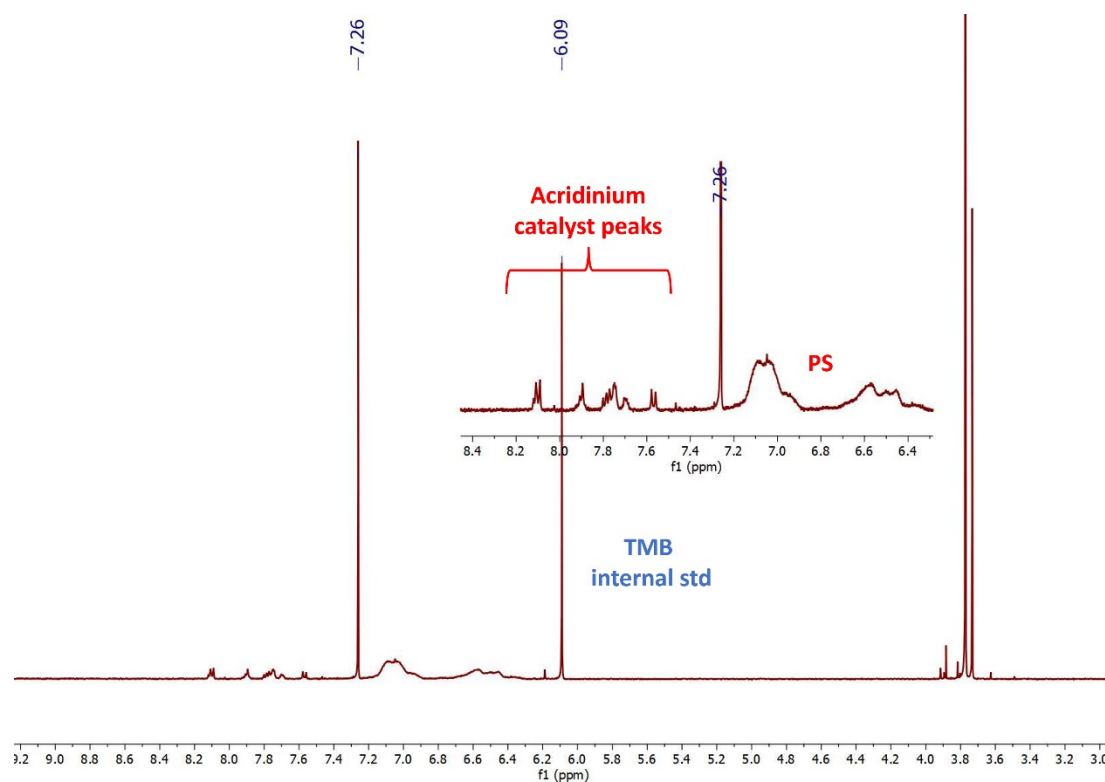
Figure S11. ^{1}H NMR spectrum of the crude reaction mixture of PS degradation in the dark catalysed by 10% mol of **Ph-Acr-Ph** in O_2 with 10% mol HCl (aq) (**Table 1, entry 4**) in CDCl$_3$. 0.3 mmol of TMB was added as the internal standard.

Figure S12. GPC chromatogram for the degraded PS in the dark catalysed by 10% mol of **Ph-Acr-Ph** in O$_2$ with 10% mol HCl (aq) (**Table 1, entry 4**).

Figure S13. ^{1}H NMR spectrum of the crude reaction mixture of PS degradation catalysed by 10% mol of **Ph-Acr-Ph** without any acid additives (**Table 1, entry 5**) in CDCl$_3$. 0.3 mmol of TMB was added as the internal standard.

Figure S14. GPC chromatogram for the degraded PS catalysed by 10% mol of **Ph-Acr-Ph** in O_2 without any acid additives (**Table 1, entry 5**).

Figure S15. ^{1}H NMR spectrum of the crude reaction mixture of PS degradation catalysed by 5% mol of **Ph-Acr-Ph** in O_2 with 200% mol HCl (aq) (**Table 1, entry 6**) in CDCl$_3$. 0.3 mmol of TMB was added as the internal standard.
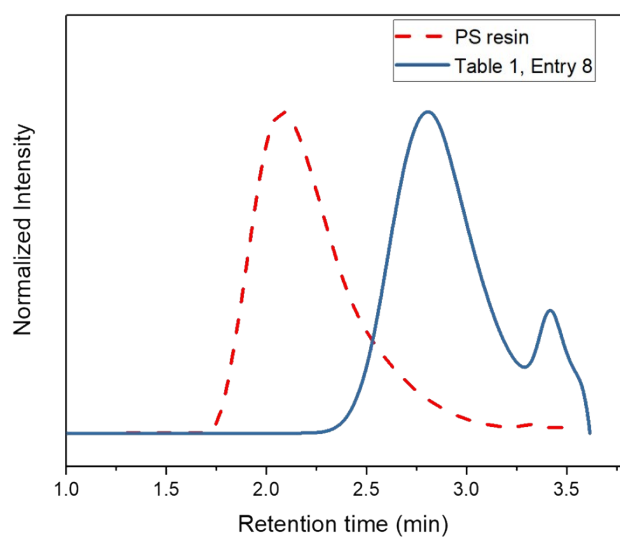
Figure S16. GPC chromatogram for the degraded PS catalysed by 5% mol of **Ph-Acr-Ph** in O_2 with 200% mol HCl (aq) (**Table 1, entry 6**).
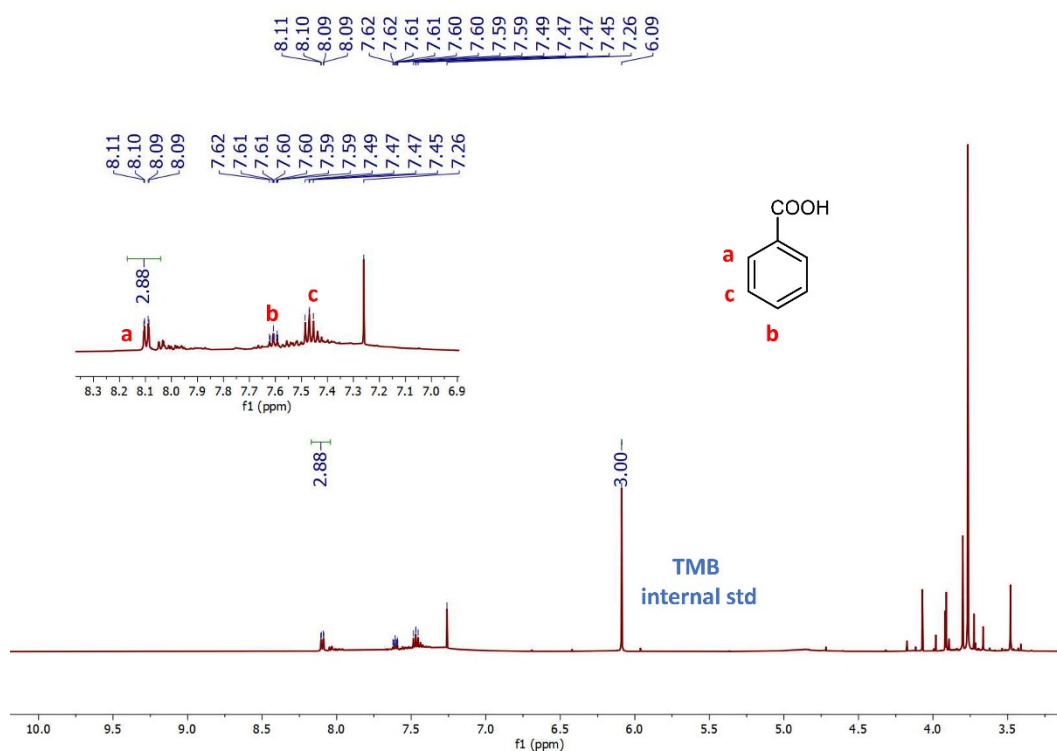

Figure S17. ^{1}H NMR spectrum of the crude reaction mixture of PS degradation catalysed by 5% mol of **Ph-Acr-Ph** in O_2 with 500% mol HCl (aq) (**Table 1, entry 7**) in CDCl$_3$. 0.3 mmol of TMB was added as the internal standard.
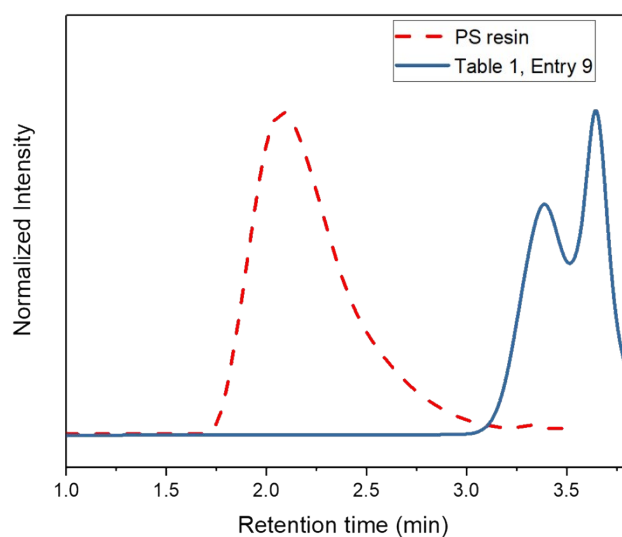
Figure S18. GPC chromatogram for the degraded PS catalysed by 5% mol of **Ph-Acr-Ph** in O_2 with 500% mol HCl (aq) (**Table 1, entry 7**).

Figure S19. ^{1}H NMR spectrum of the crude reaction mixture of PS degradation catalysed by 5% mol of **Ph-Acr-Ph** in O_2 with 200% mol HBr (aq) (**Table 1, entry 8**) in CDCl$_3$. 0.3 mmol of TMB was added as the internal standard.

Figure S20. GPC chromatogram for the degraded PS catalysed by 5% mol of **Ph-Acr-Ph** in O_2 with 200% mol HBr (aq) (**Table 1, entry 8**).
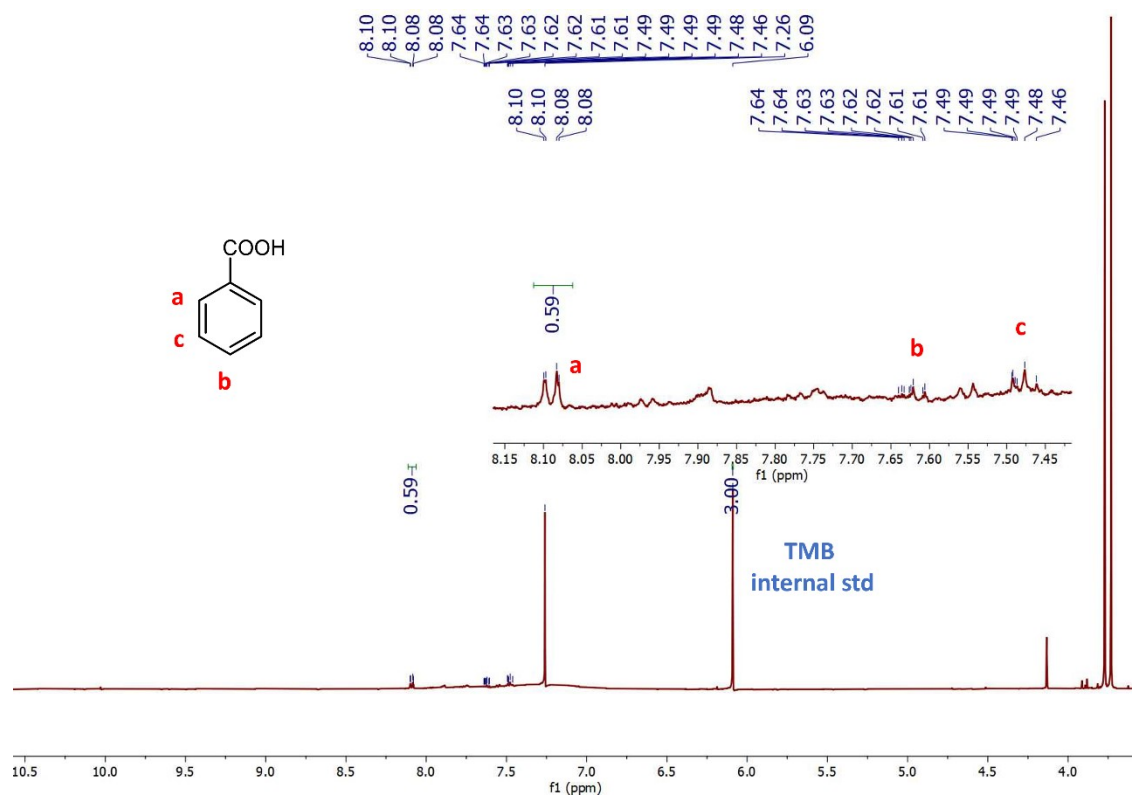

Figure S21. ^{1}H NMR spectrum of the crude reaction mixture of PS degradation catalysed by 5% mol of **Ph-Acr-Ph** in O_2 with 200% mol HCl (aq) with 440 nm irradiation (**Table 1, entry 9**) in CDCl$_3$. 0.3 mmol of TMB was added as the internal standard.
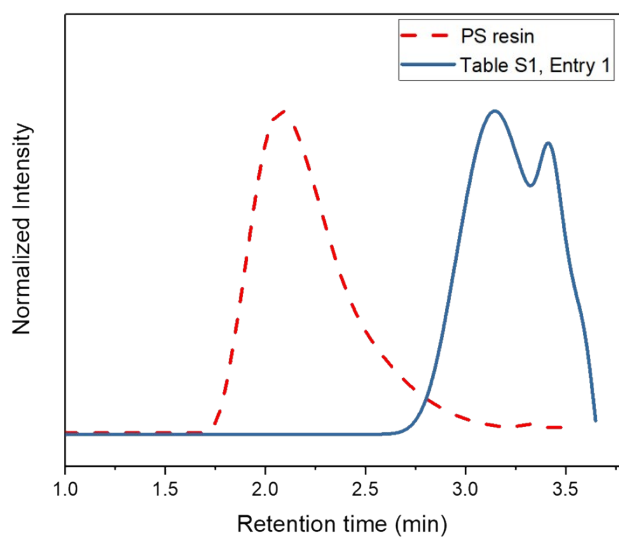
Figure S22. GPC chromatogram for the degraded PS catalysed by 5% mol of **Ph-Acr-Ph** in O_2 with 200% mol HCl (aq) with 440 nm irradiation (**Table 1, entry 9**).
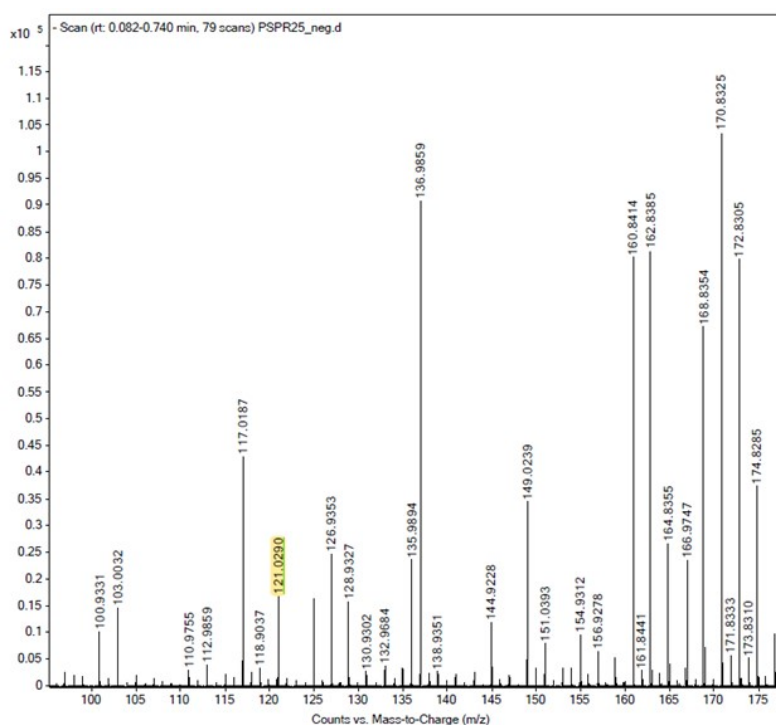

Figure S23. ESI-MS spectrum showing the unequivocal presence of benzoic acid formed under the catalytic conditions in **Table 1, entry 6**. [M-H] peak at m/z = 121.0290 (error: 0.0000 ppm). Several other compounds are also produced in trace quantities (not detectable by ^{1}H NMR), which are postulated to be mono-chlorinated benzoic acid [M-H] peak at m/z = 154.9312 (error: 0.0588 ppm) and mono-chlorinated benzaldehyde or benzoyl chloride [M-H] peak at m/z = 138.9351 (error: 0.0597ppm).
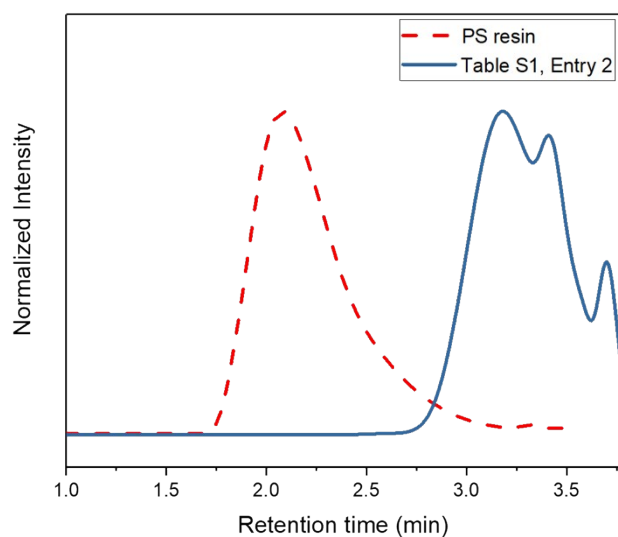
Figure S24. ^{1}H NMR spectrum of the crude reaction mixture of PS degradation catalysed by 10% mol of **Ph-Acr-Ph** in air with 10% mol HCl (aq) (**Table S1, entry 1**) in CDCl$_3$. 0.3 mmol of TMB was added as the internal standard.
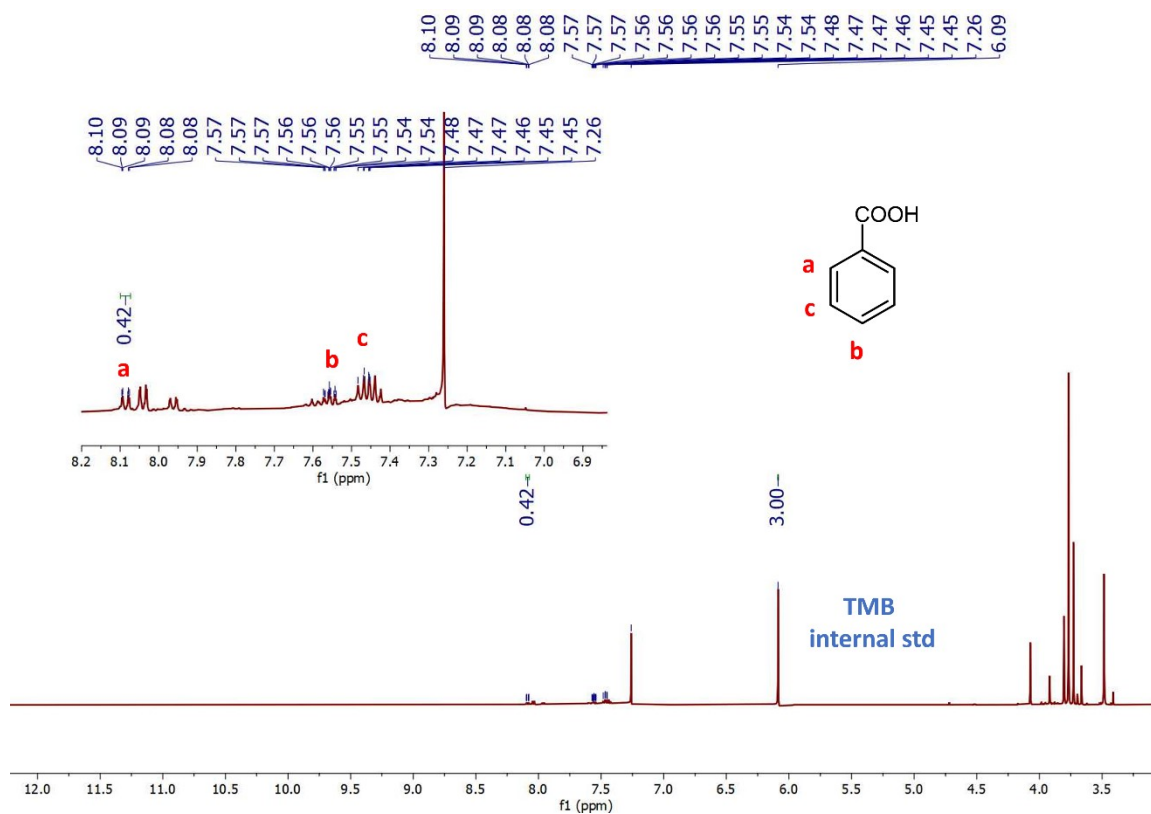

Figure S25. GPC chromatogram for the degraded PS catalysed by 10% mol of **Ph-Acr-Ph** in air with 10% mol HCl (aq) (**Table S1, entry 1**).
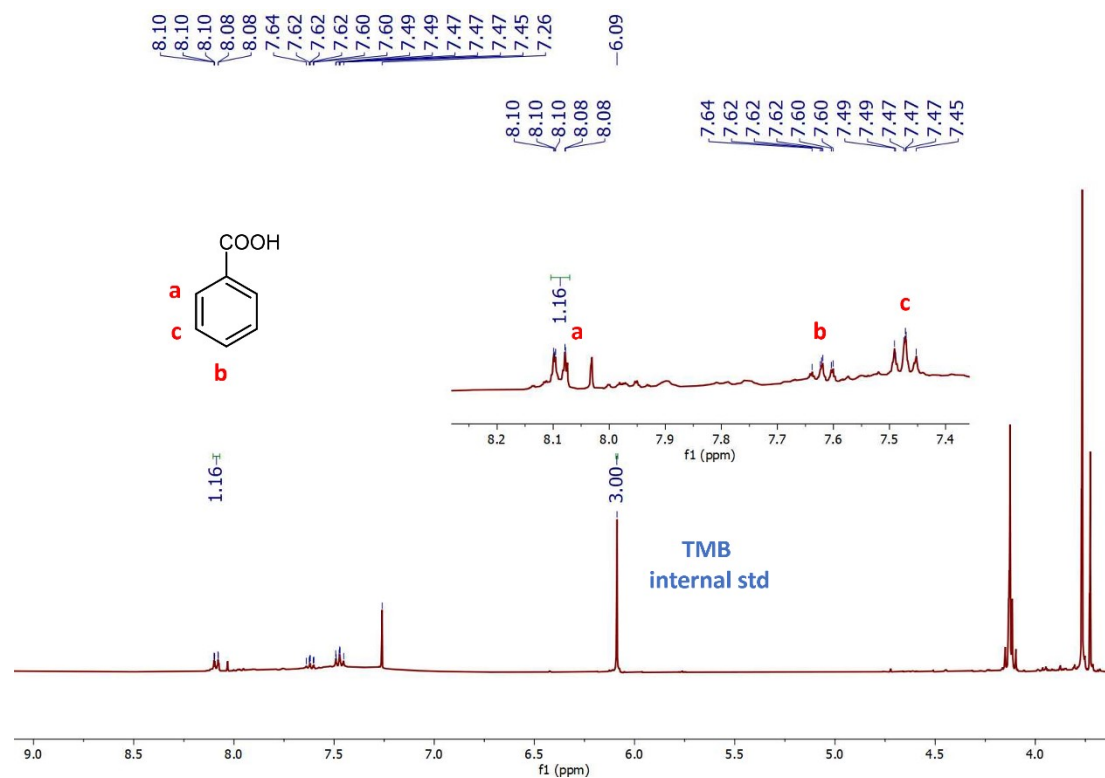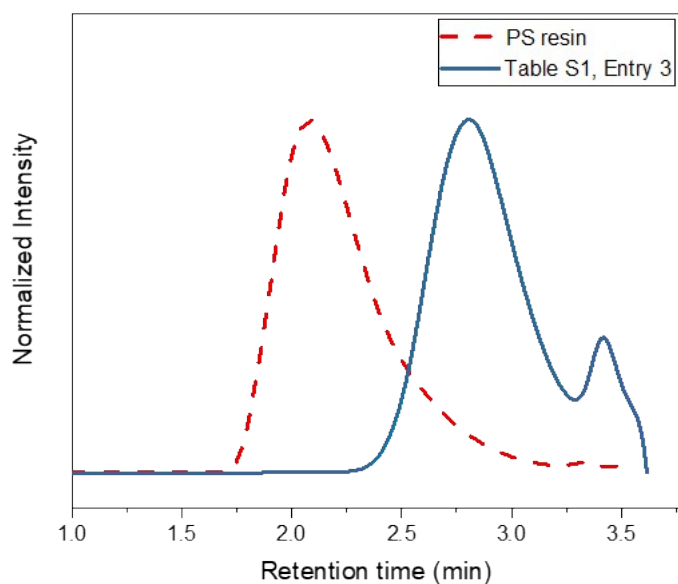
Figure S26. ^{1}H NMR spectrum of the crude reaction mixture of PS degradation catalysed by 10% mol of **Ph-Acr-Ph** in O_2 with 0.7 µL of H_2O (**Table S1, entry 2**) in $CDCl_3$. 0.3 mmol of TMB was added as the internal standard.


Figure S27. GPC chromatogram for the degraded PS catalysed by 10% mol of **Ph-Acr-Ph** in O_2 with 0.7 µL of H_2O (**Table S1, entry 2**).

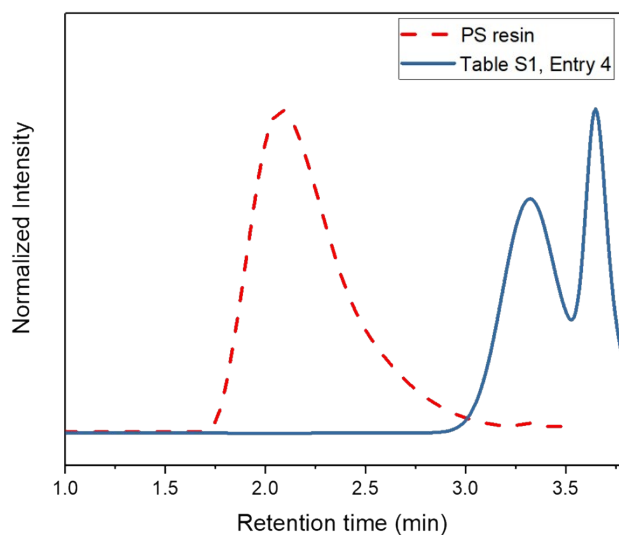**Figure S28.** ^{1}H NMR spectrum of the crude reaction mixture of PS degradation catalysed by 200% mol of HCl (aq) in O_2 (**Table S1, entry 3**) in CDCl$_3$. 0.3 mmol of TMB was added as the internal standard.
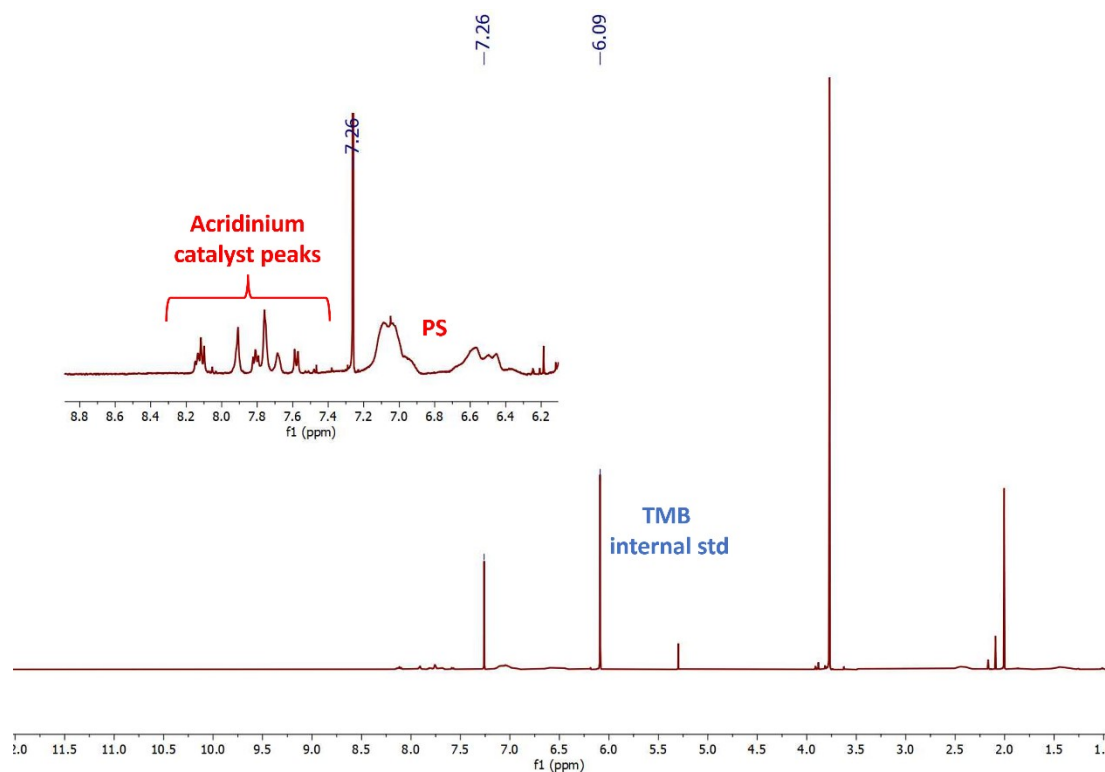

Figure S29. GPC chromatogram for the degraded PS catalysed by 200% mol of HCl (aq) in O_2 (**Table S1, entry 3**)
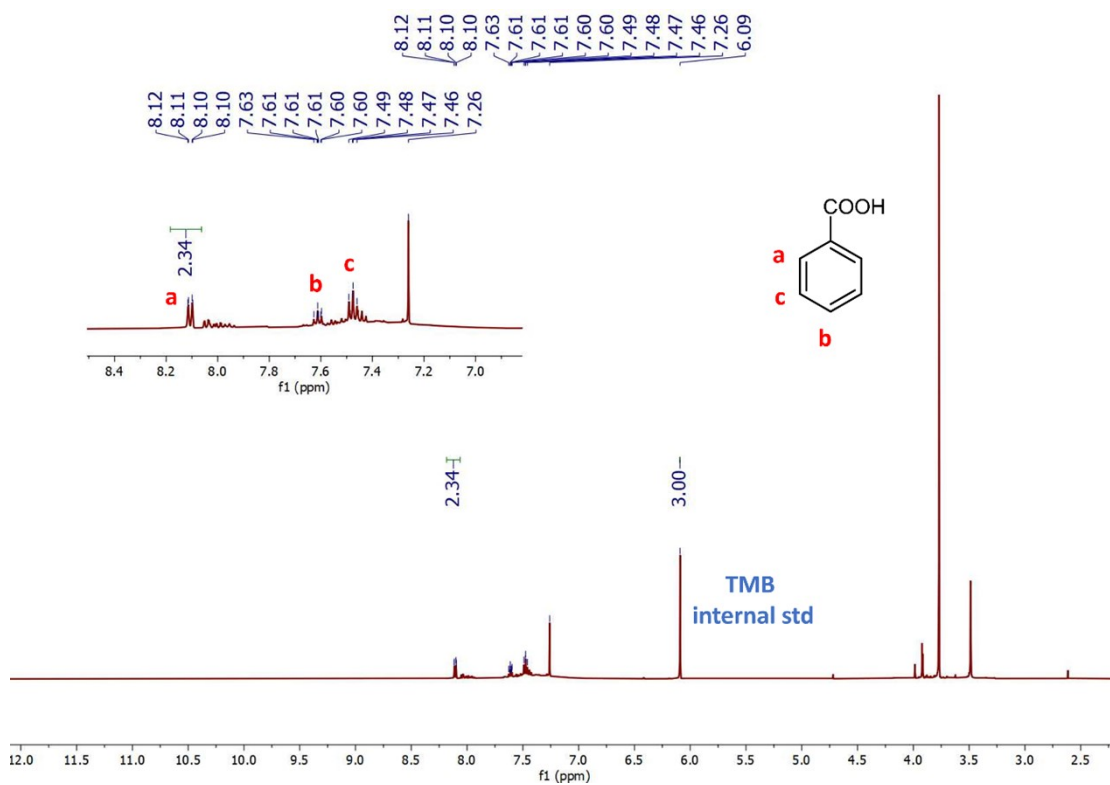
Figure S30. ^{1}H NMR spectrum of the crude reaction mixture of PS degradation catalysed by 5% mol of **Ph-Acr-Ph** in O_2 with 200% mol of HCl (aq) with CHCl$_3$ as the solvent (**Table S1, entry 4**) in CDCl$_3$. 0.3 mmol of TMB was added as the internal standard.

Figure S31. GPC for the degraded PS catalysed by 5% mol of **Ph-Acr-Ph** in O_2 with 200% mol of HCl (aq) with CHCl$_3$ as the solvent (**Table S1, entry 4**)
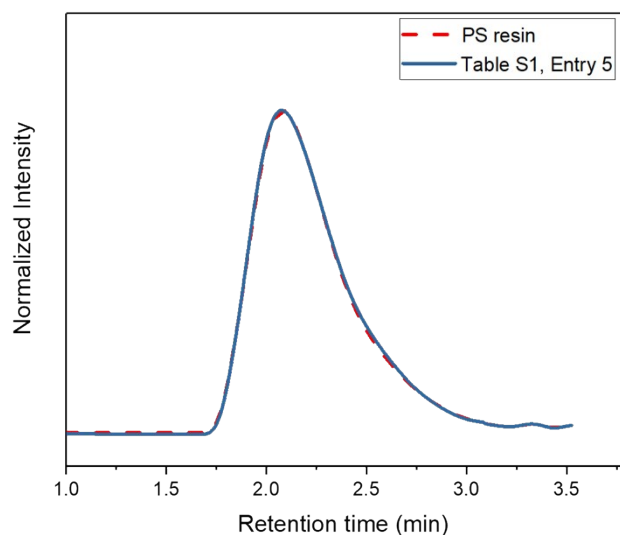
Figure S32. ^{1}H NMR spectrum of the crude reaction mixture of PS degradation catalysed by 5% mol of **Ph-Acr-Ph** in O_2 with 200% mol of HCl (aq) with MeCN as the solvent (**Table S1, entry 5**) in CDCl$_3$. 0.3 mmol of TMB was added as the internal standard.

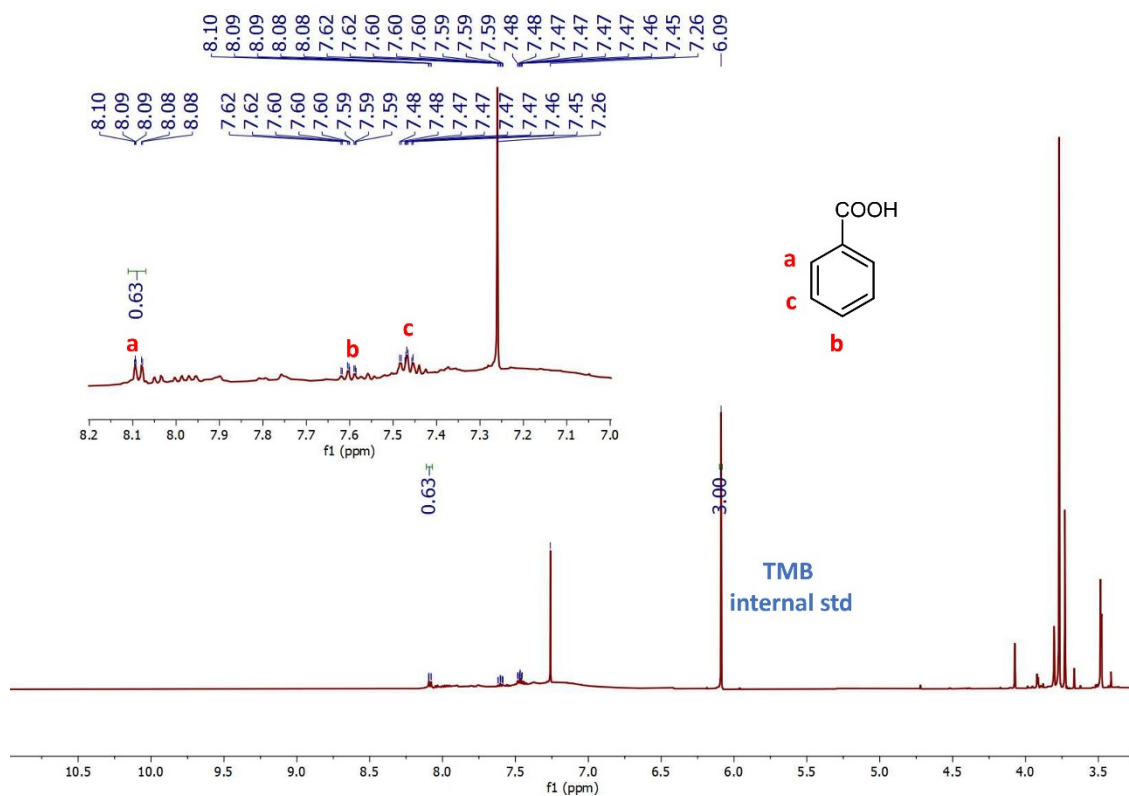**Figure S33.** GPC chromatogram for the degraded PS catalysed by 5% mol of **Ph-Acr-Ph** in O_2 with 200% mol of HCl (aq) with MeCN as the solvent (**Table S1, entry 5**)

Figure S34. ^{1}H NMR spectrum of the crude reaction mixture of PS degradation catalysed by 5% mol of **Ph-Acr-Ph** in O_2 with 200% mol of HCl (aq) with DCE/MeCN (4:3 v/v) as the solvent (**Table S1, entry 6**) in CDCl$_3$. 0.3 mmol of TMB was added as the internal standard.

Figure S35. GPC chromatogram for the degraded PS catalysed 5% mol of **Ph-Acr-Ph** in O_2 with 200% mol of HCl (aq) with DCE/MeCN (4:3 v/v) as the solvent (**Table S1, entry 6**)
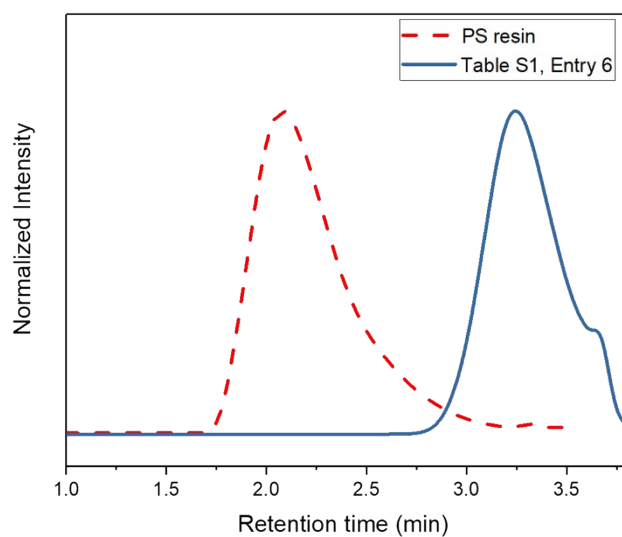
Figure S36. ^{1}H NMR spectrum of the crude reaction mixture of PS degradation catalysed by 5% mol of **Ph-Acr-Ph** in O$_2$ with 200% mol of HCl (aq) with EA/DCE (1:1 v/v) as the solvent (**Table S1, entry 7**) in CDCl$_3$. 0.3 mmol of TMB was added as the internal standard.

Figure S37. GPC chromatogram for the degraded PS catalysed by 5% mol of **Ph-Acr-Ph** in O$_2$ with 200% mol of HCl (aq) with EA/DCE (1:1 v/v) as the solvent (**Table S1, entry 7**)

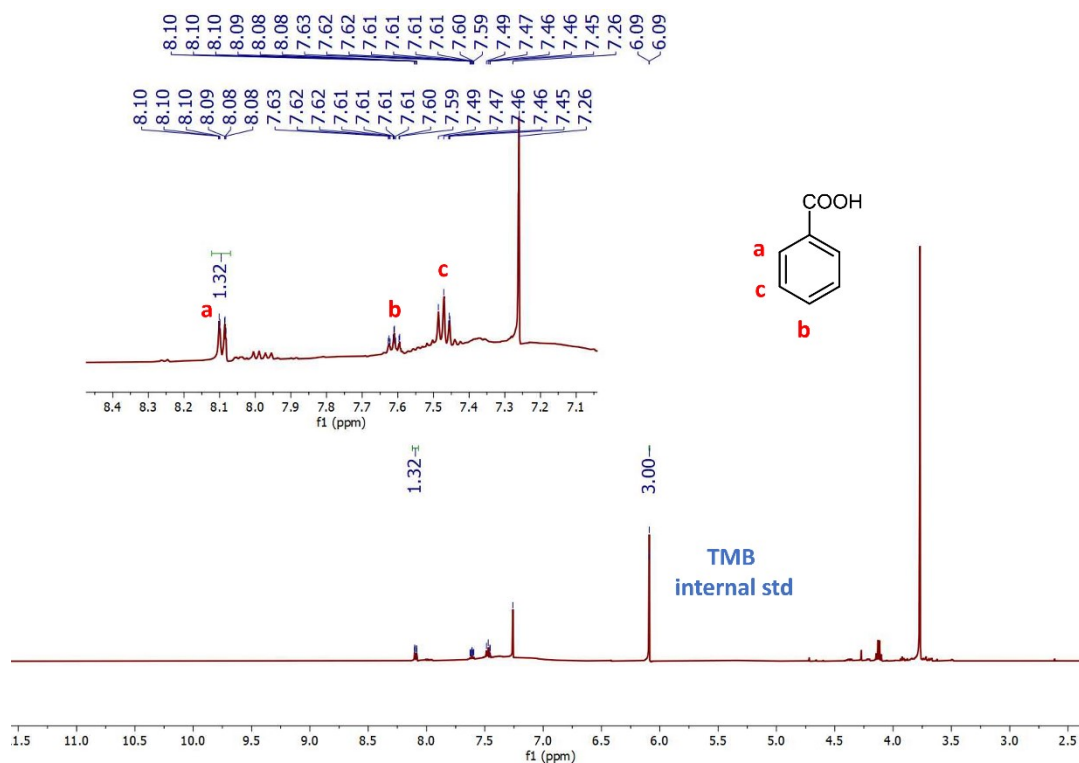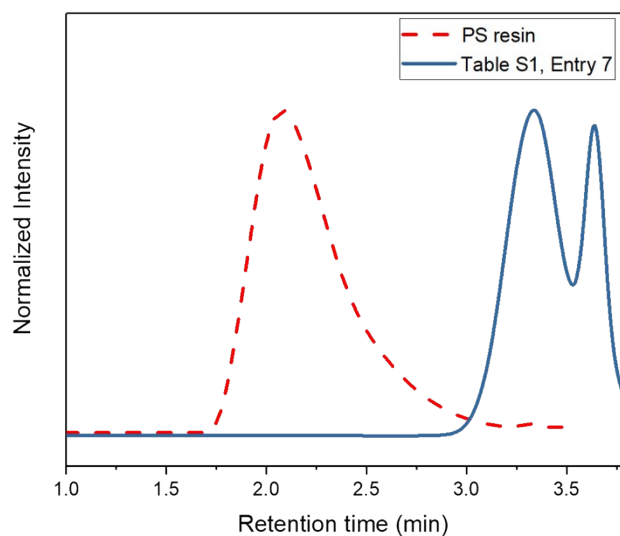**Figure S38.** ^{1}H NMR spectrum of the crude reaction mixture of PS degradation catalysed by 5% mol of **Ph-Acr-Ph** in O_2 with 200% mol of TBACl (**Table S1, entry 8**) in CDCl$_3$. 0.3 mmol of TMB was added as the internal standard.

Figure S39. GPC chromatogram for the degraded PS catalysed by 5% mol of **Ph-Acr-Ph** in O_2 with 200% mol of TBACl (**Table S1, entry 8**)
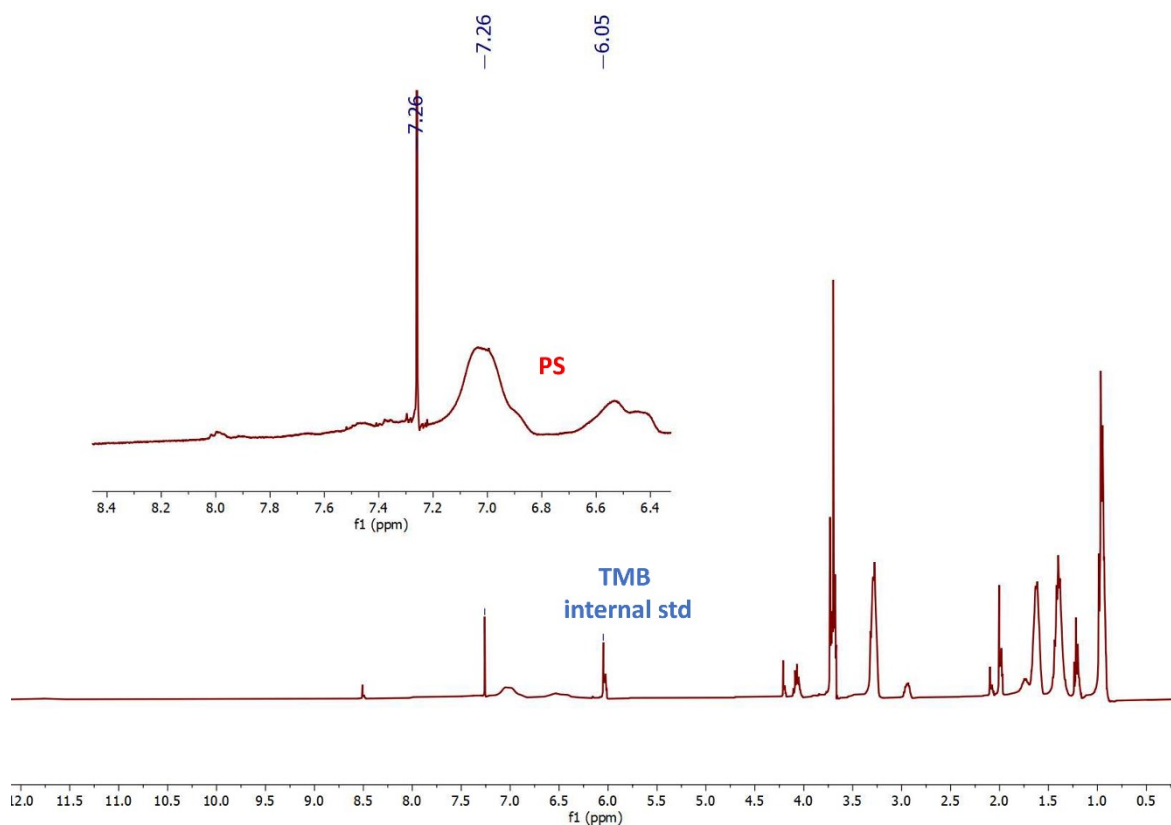
Figure S40. ^{1}H NMR spectrum of the crude reaction mixture of PS degradation catalysed by 5% mol of **Mes-Acr-Me** in O_2 with 200% mol of HCl (aq) (**Table S1, entry 9**) in CDCl$_3$. 0.3 mmol of TMB was added as the internal standard.

Figure S41. GPC chromatogram for the degraded PS catalysed by 5% mol of **Mes-Acr-Me** in O_2 with 200% mol of HCl (aq) (**Table S1, entry 9**)
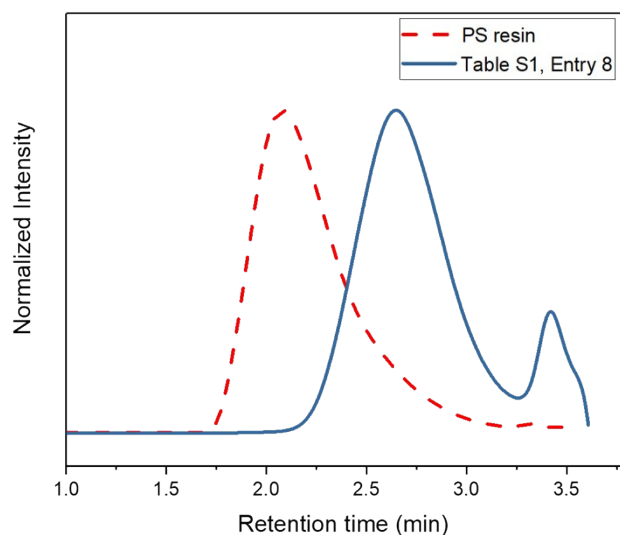
Figure S42. ^{1}H NMR spectrum of the crude reaction mixture of PS degradation catalysed by 5% mol of **MeOPh-Acr-Ph** in O_2 with 200% mol of HCl (aq) (**Table S1, entry 10**) in CDCl$_3$. 0.3 mmol of TMB was added as the internal standard.
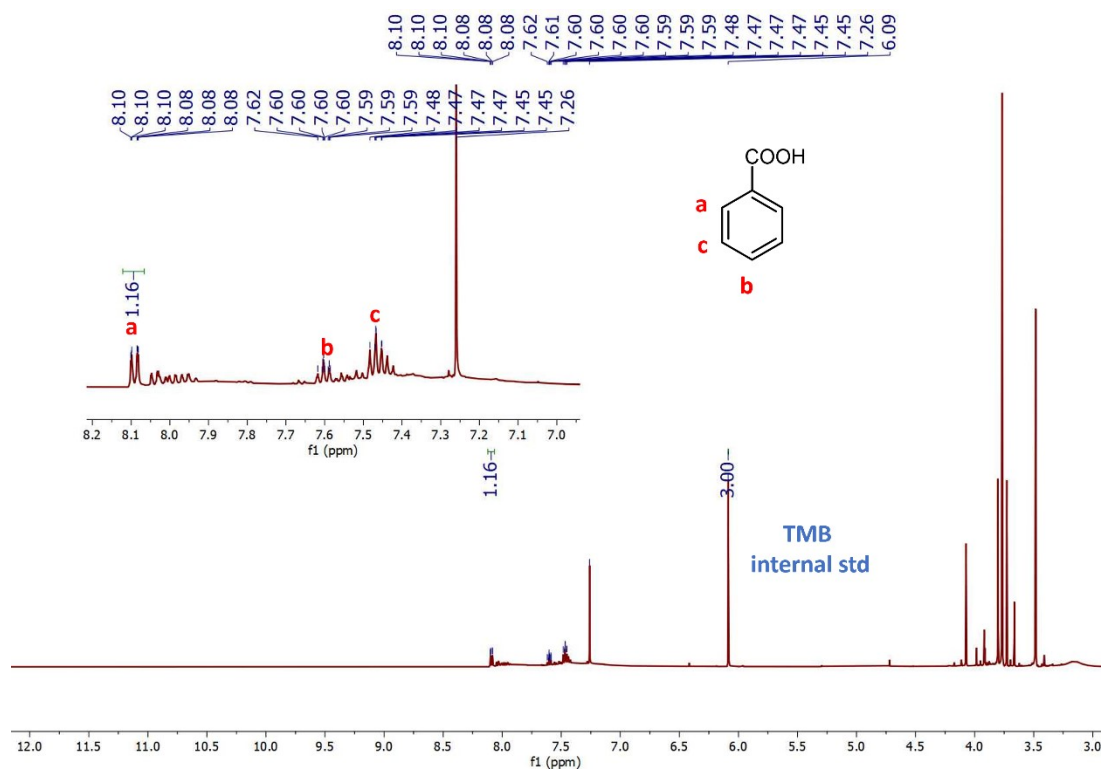

Figure S43. GPC chromatogram for the degraded PS catalysed by 5% mol of **MeOPh-Acr-Ph** in O_2 with 200% mol of HCl (aq) (**Table S1, entry 10**)
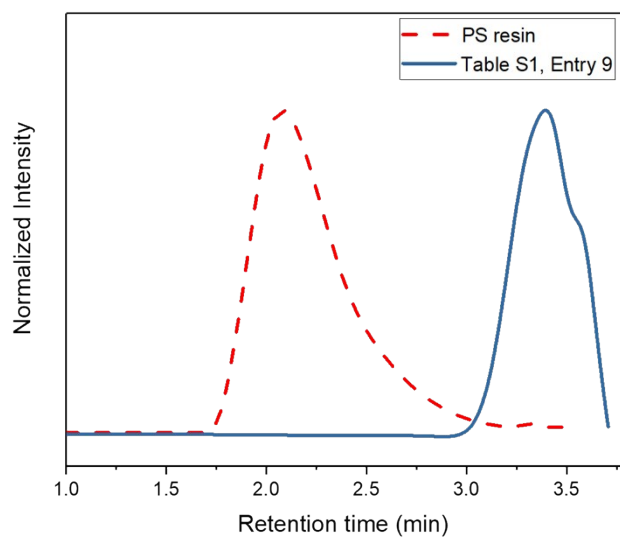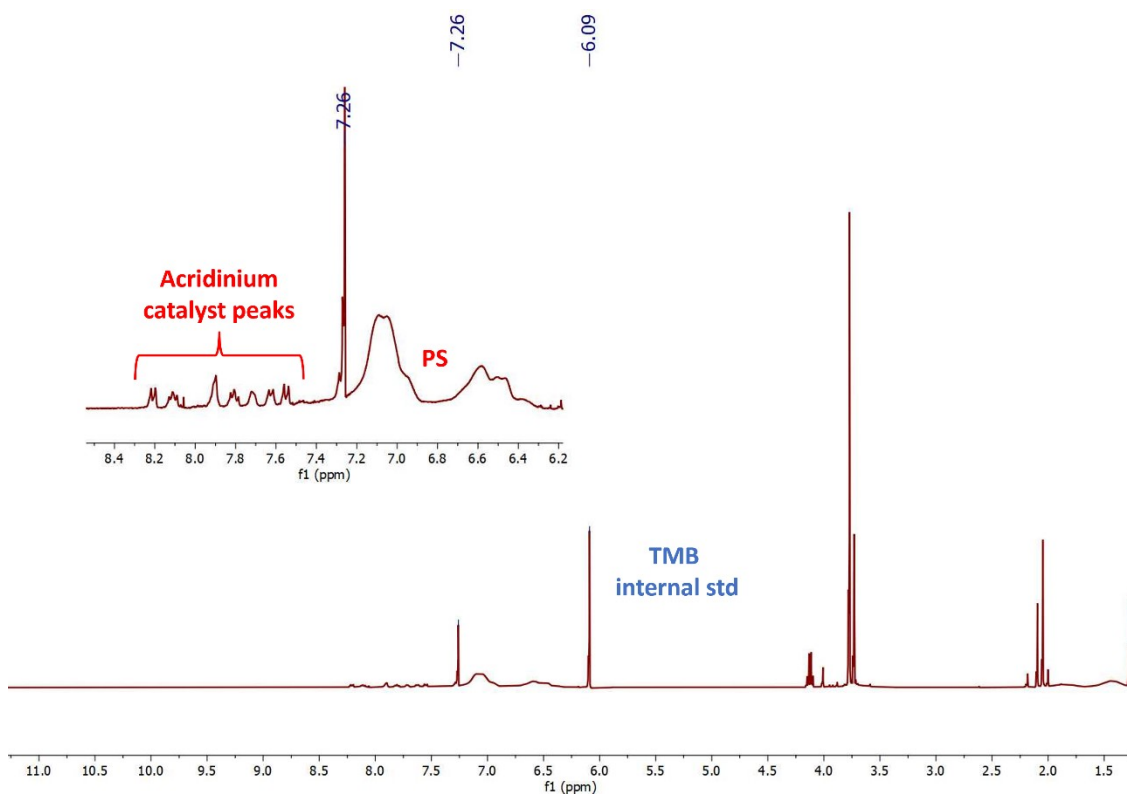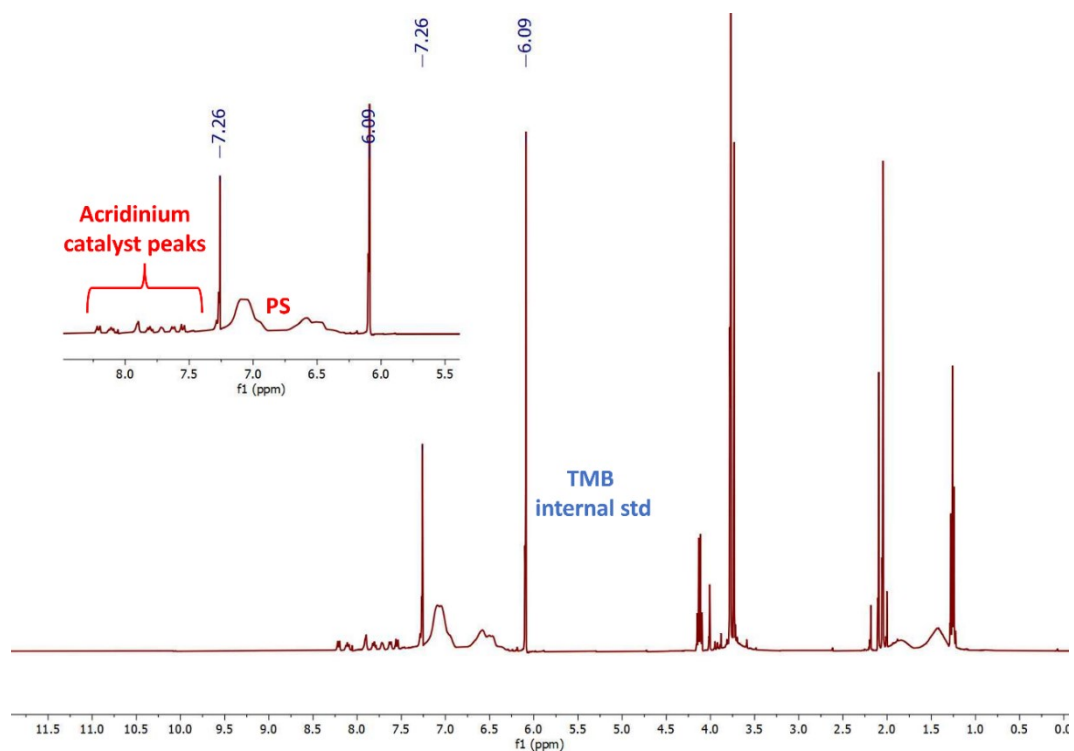
Figure S44. ^{1}H NMR spectrum of the crude reaction mixture of PS degradation catalysed by 5% mol of **MeOPh-Acr-Ph** in O_2 with 200% mol of HCl (aq) under 440 nm irradiation (**Table S1, entry 11**) in CDCl$_3$. 0.3 mmol of TMB was added as the internal standard.
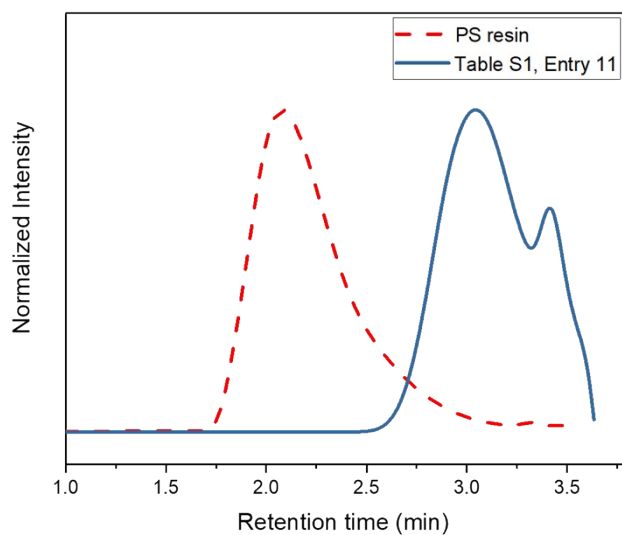
Figure S45. GPC chromatogram for the degraded PS catalysed by 5% mol of **MeOPh-Acr-Ph** in O_2 with 200% mol of HCl (aq) under 440 nm irradiation (**Table S1, entry 11**)
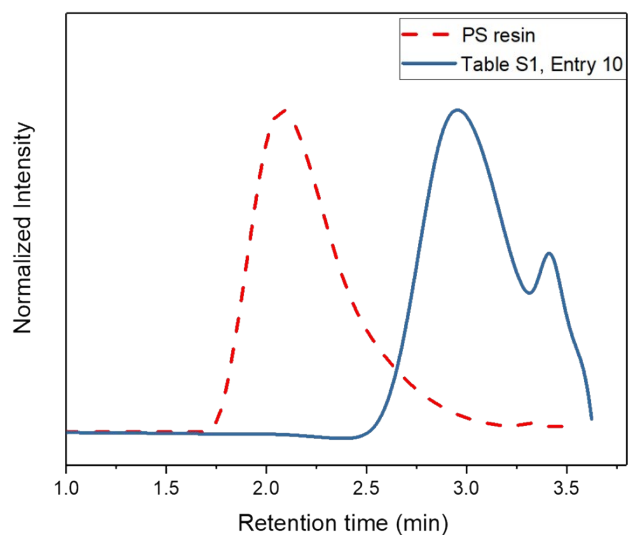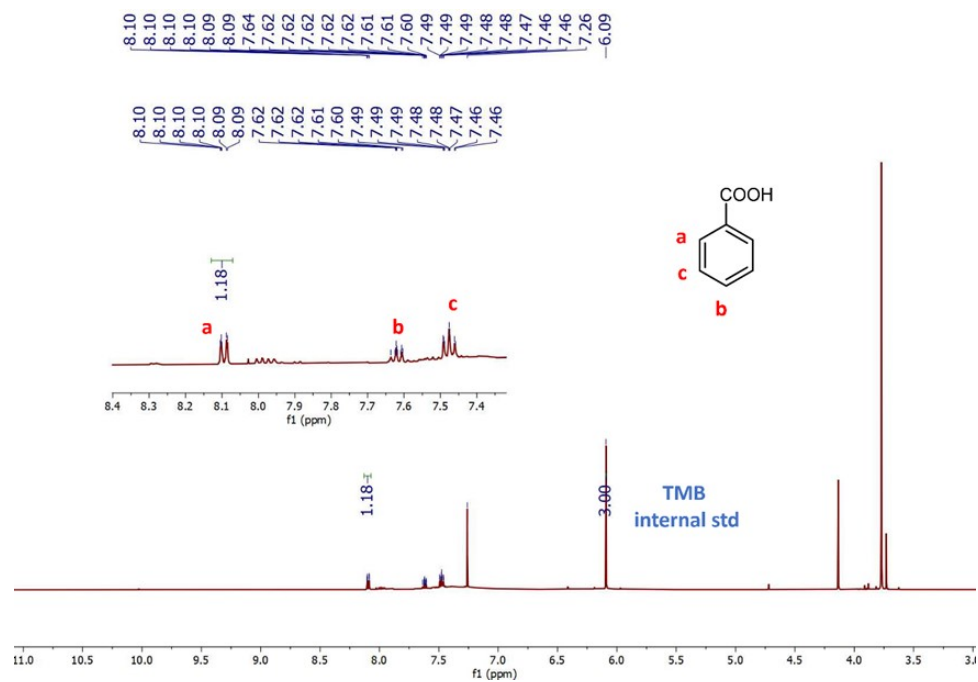
Figure S46. ¹H NMR spectrum of the crude reaction mixture of PS degradation catalysed by 1% mol of **FPh-Acr-Np** in O_2 with 200% mol of HCl (aq) under 390 nm irradiation in $CDCl_3$. 0.3 mmol of TMB was added as the internal standard.
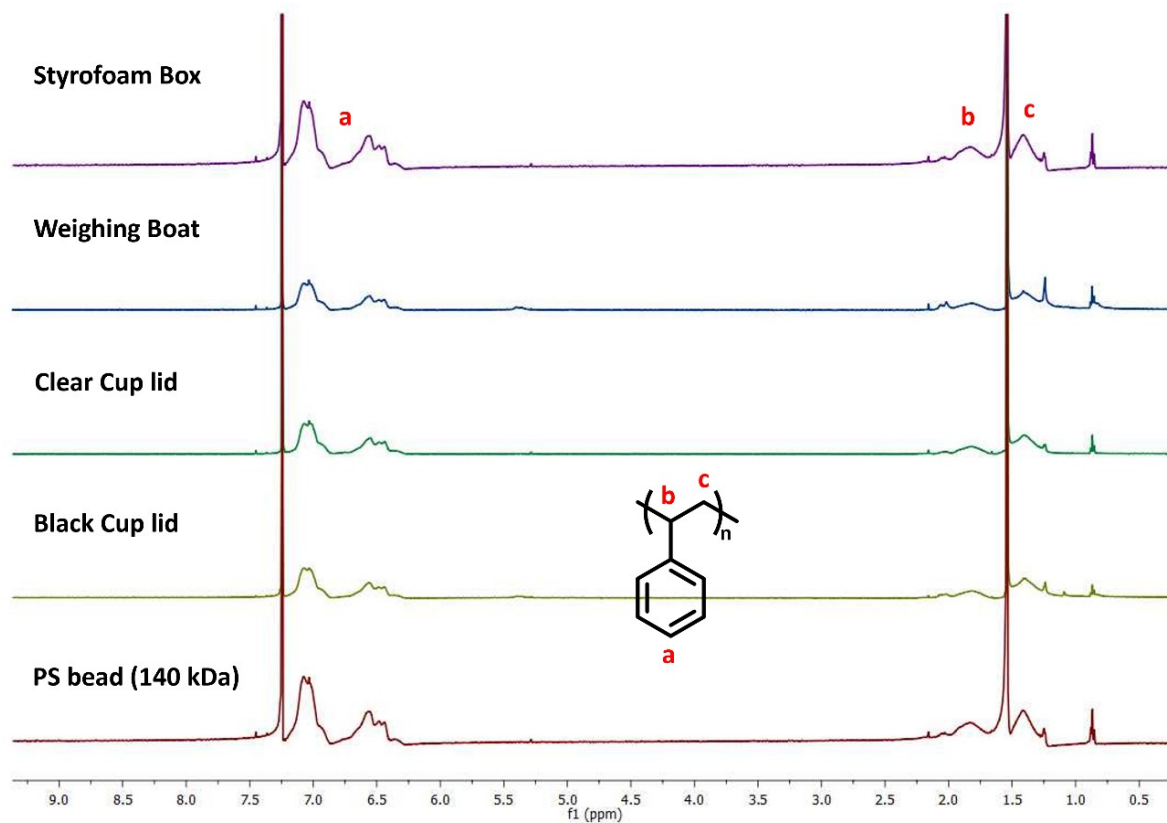
Figure S47. Stacked ¹H NMR spectra of commercial PS waste products in $CDCl_3$
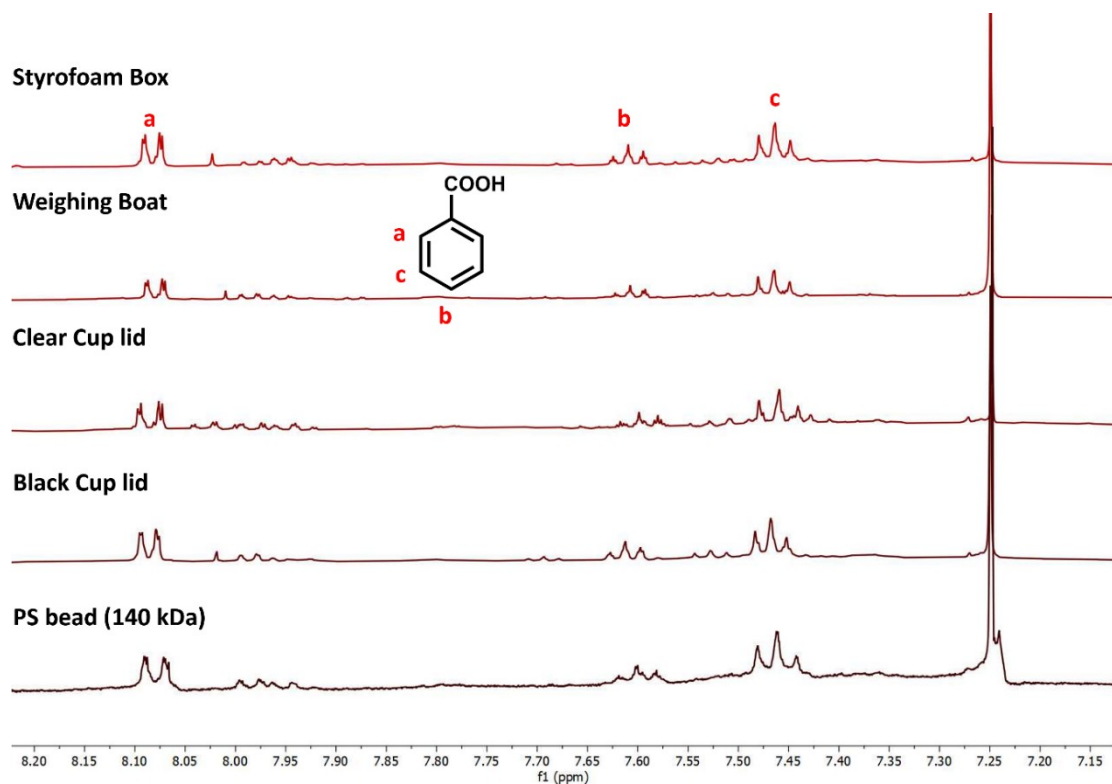
Figure S48. Stacked ^{1}H NMR spectra (CDCl$_3$) of the crude reaction mixtures of degraded commercial PS products catalysed by **FPh-Acr-Np** (**Figure 2Cii**)
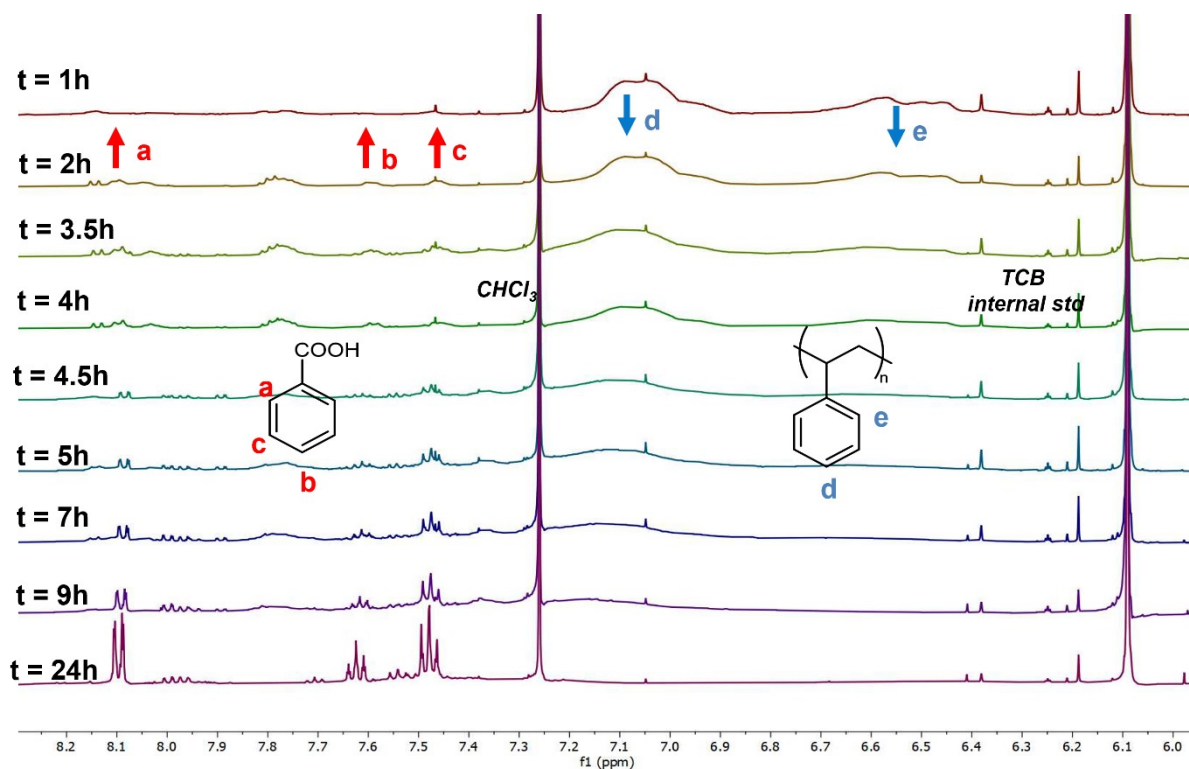
Figure S49. Stacked ^{1}H NMR spectra of time-course experiments (in CDCl$_3$) for degradation of PS resins catalysed by **FPh-Acr-Np**, showing the evolution of benzoic acid and consumption of PS with time.
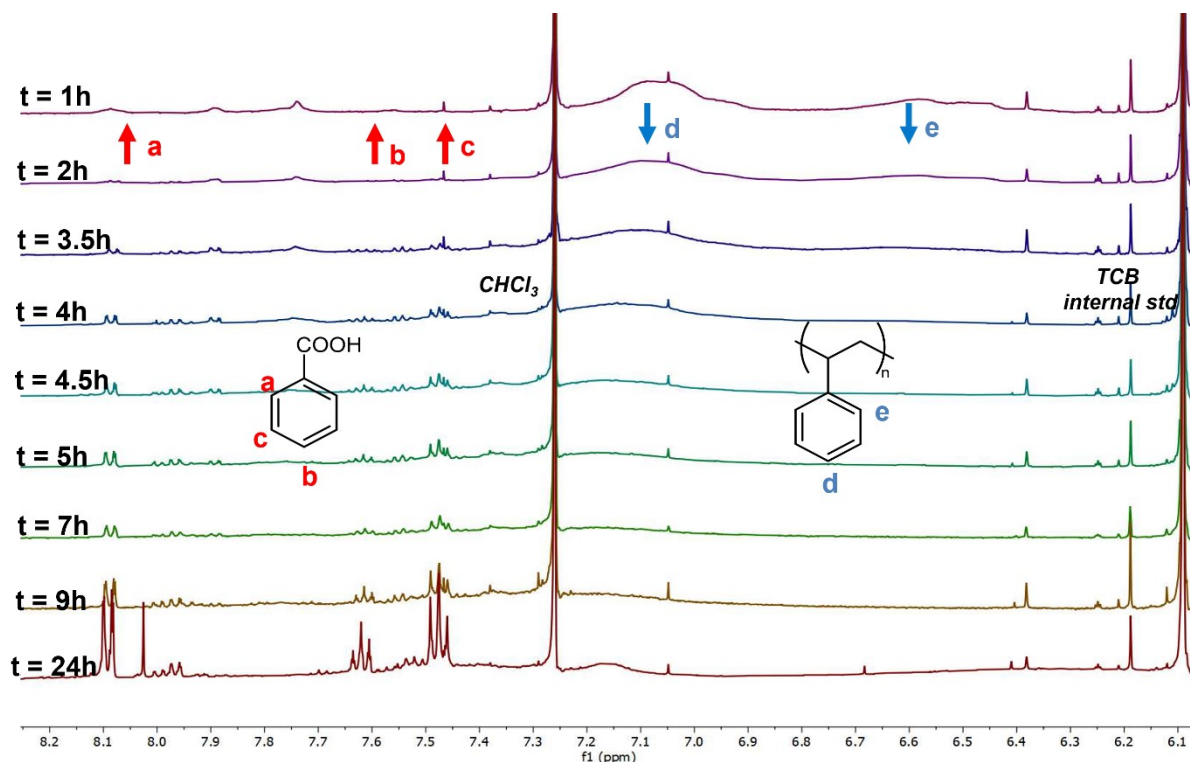
Figure S50. Stacked ^{1}H NMR spectra of time-course experiments (in CDCl$_3$) for degradation of PS resins catalysed by **Ph-Acr-Ph**, showing the evolution of benzoic acid and consumption of PS with time.
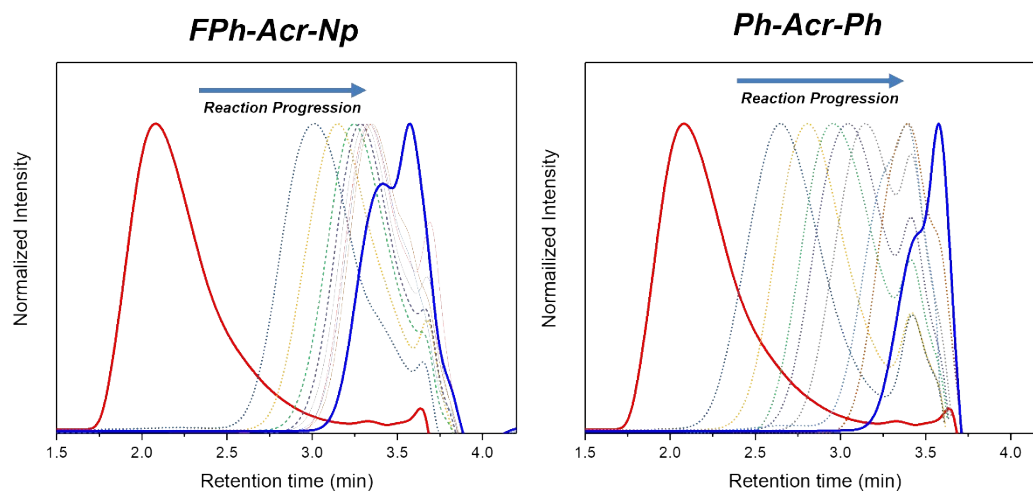
Figure S51. Stacked GPC chromatogram of time-course experiments for degradation of PS resins catalysed by (left) **FPh-Acr-Np** and (right) **Ph-Acr-Ph**, showing decrease in average molecular size of the reaction mixture. Solid red line depicts original PS polymer while solid blue line depicts reaction mixture after 24 h. Average M_n vs reaction time plot can be found in **Figure 3C.**

Characterization of synthesized Acridinium catalysts
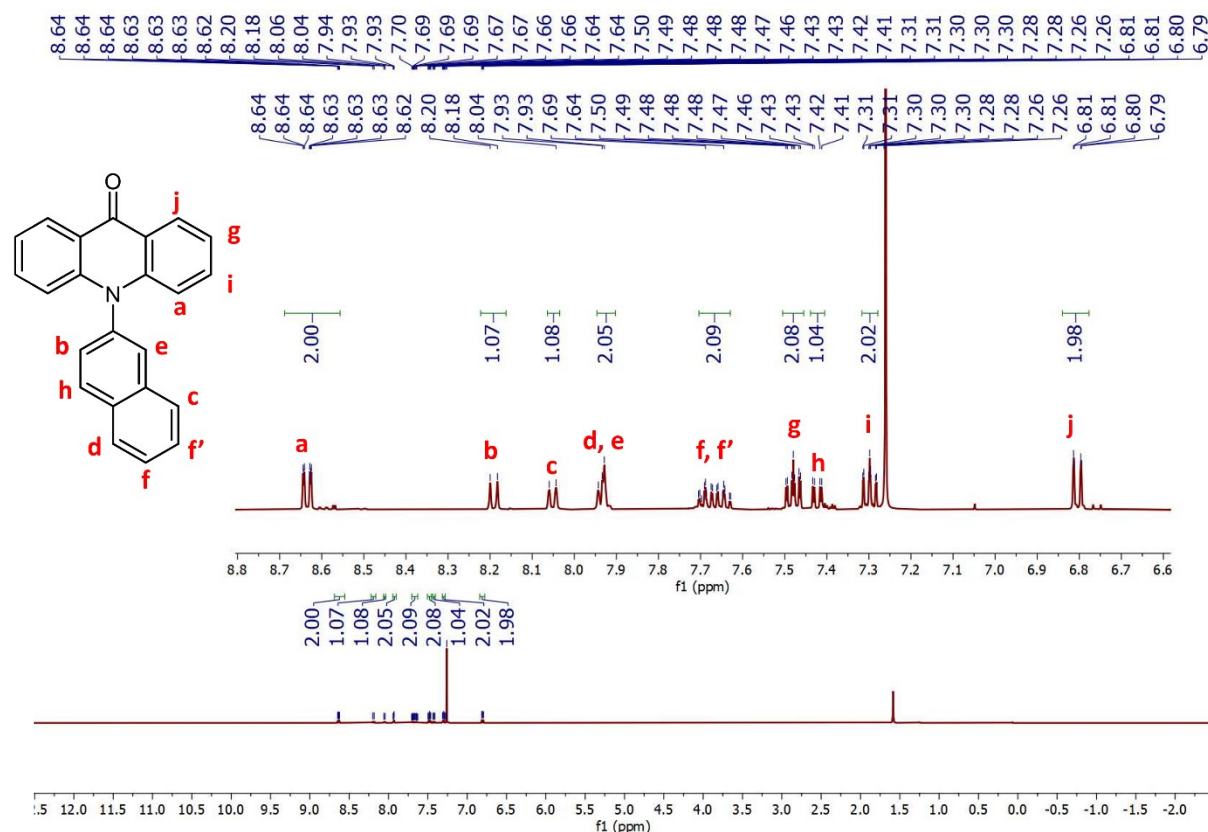
Figure S52. ^{1}H NMR spectra of synthesised **Acridone-Nap** in CDCl$_3$.
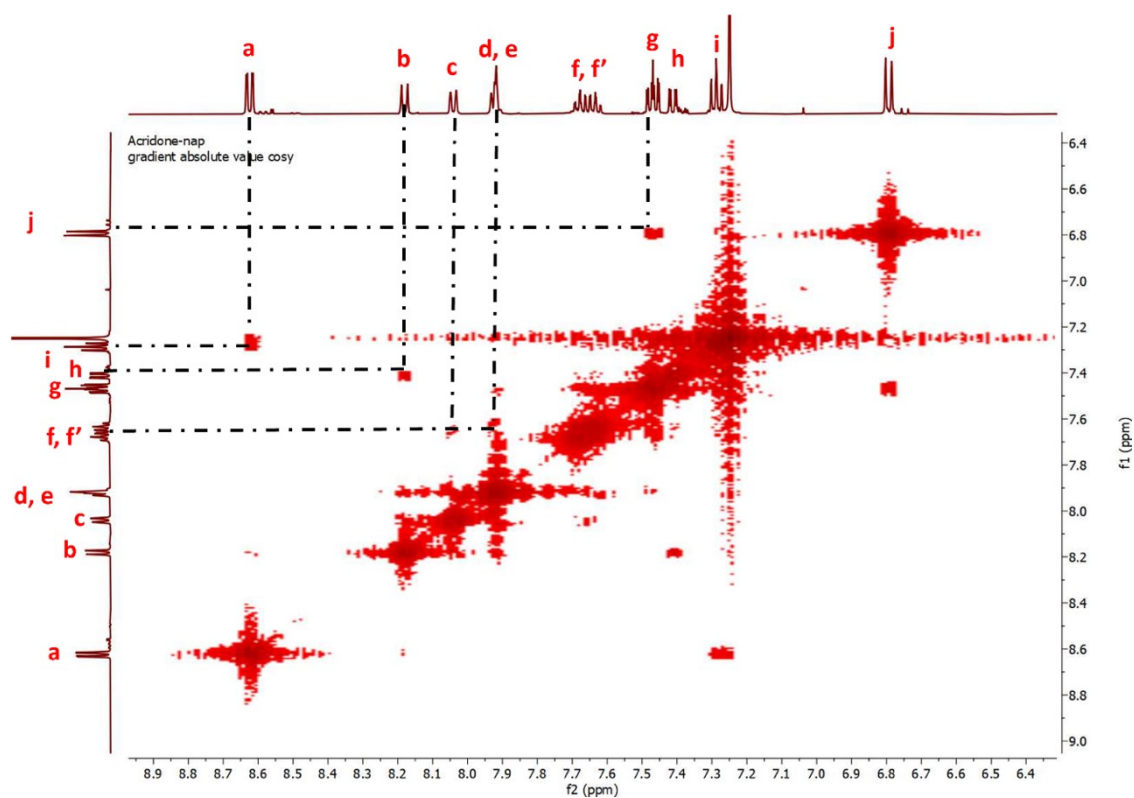
Figure S53. COSY NMR spectra of synthesised **Acridone-Nap** in CDCl$_3$.
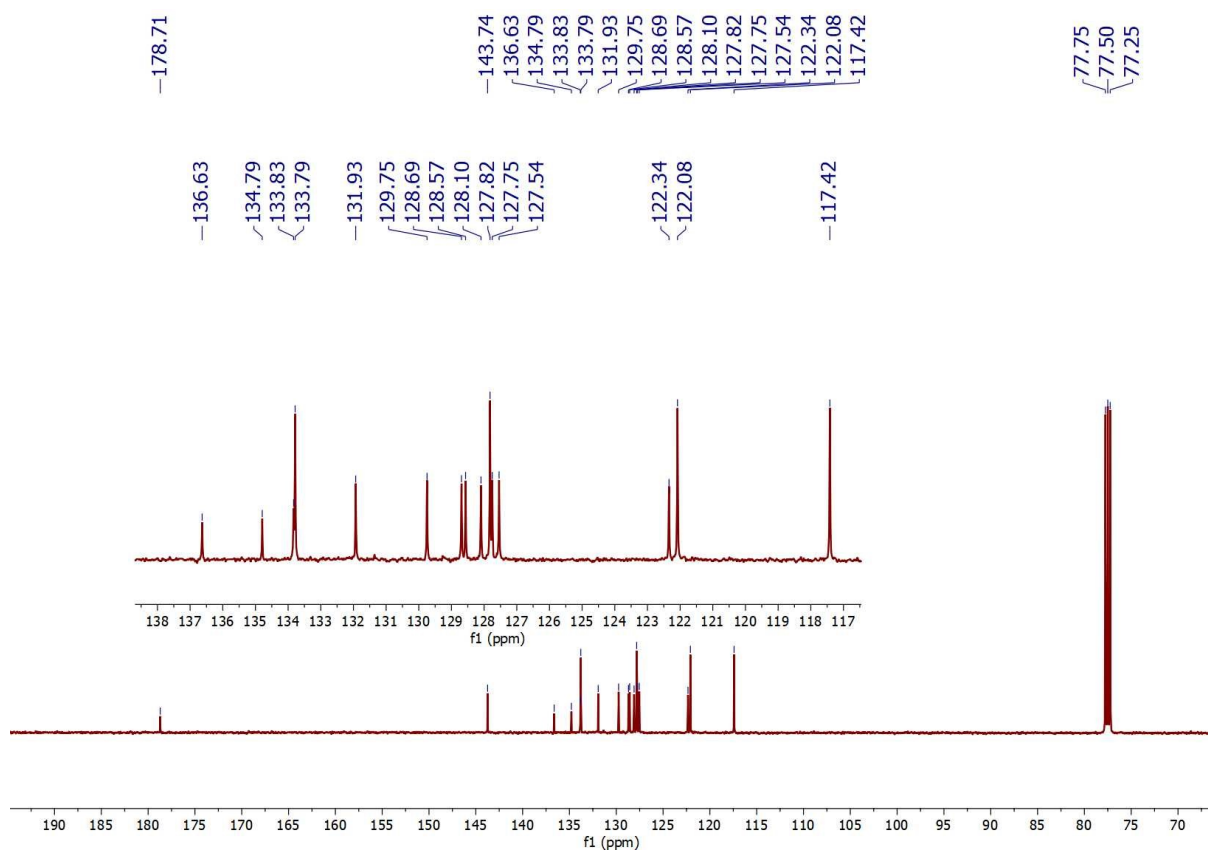
Figure S54. ^{13}C NMR spectra of synthesised **Acridone-Nap** in CDCl$_3$.
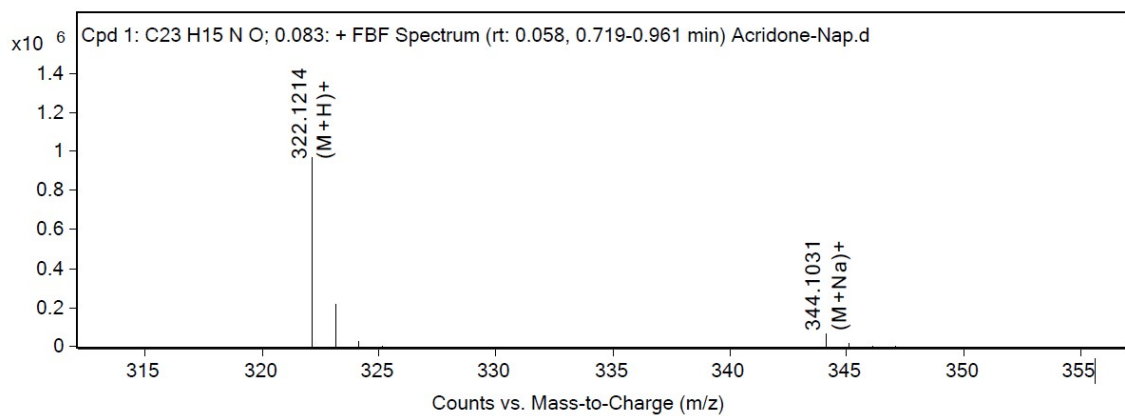
Figure S55. ESI-MS spectrum of **Acridone-Nap** showing the [M+H] peak at m/z = 322.1214 (error: 0.0018 ppm).
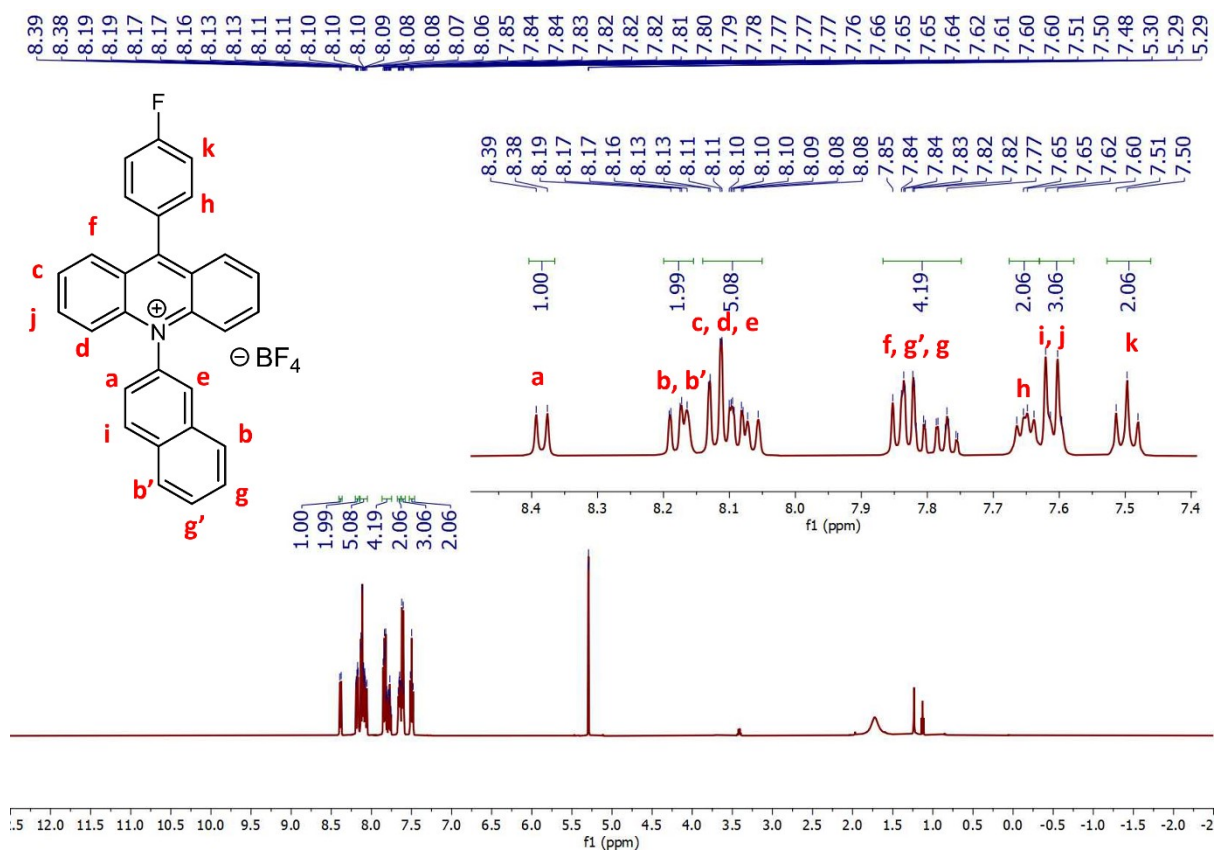
Figure S56. ^{1}H NMR spectra of synthesised **FPh-Acr-Np** in CD$_2$Cl$_2$.
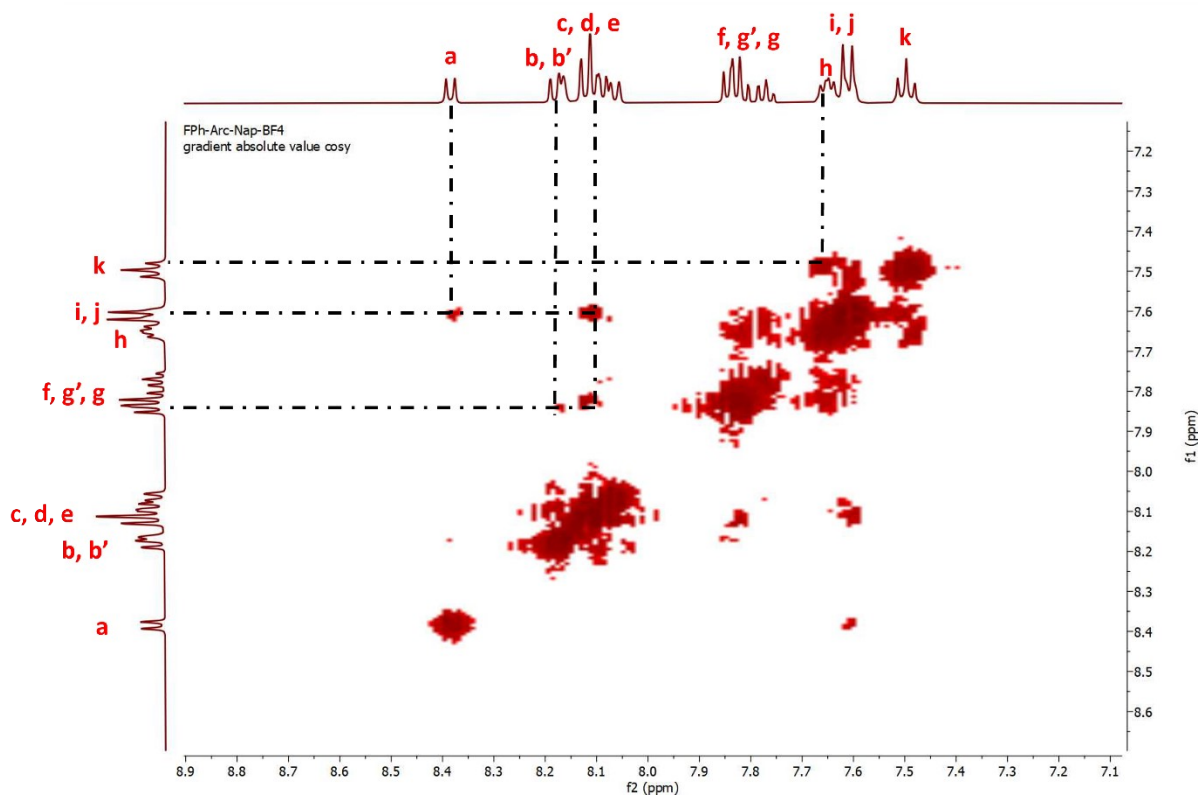
Figure S57. COSY NMR spectra of synthesised **FPh-Acr-Np** in CD$_2$Cl$_2$.
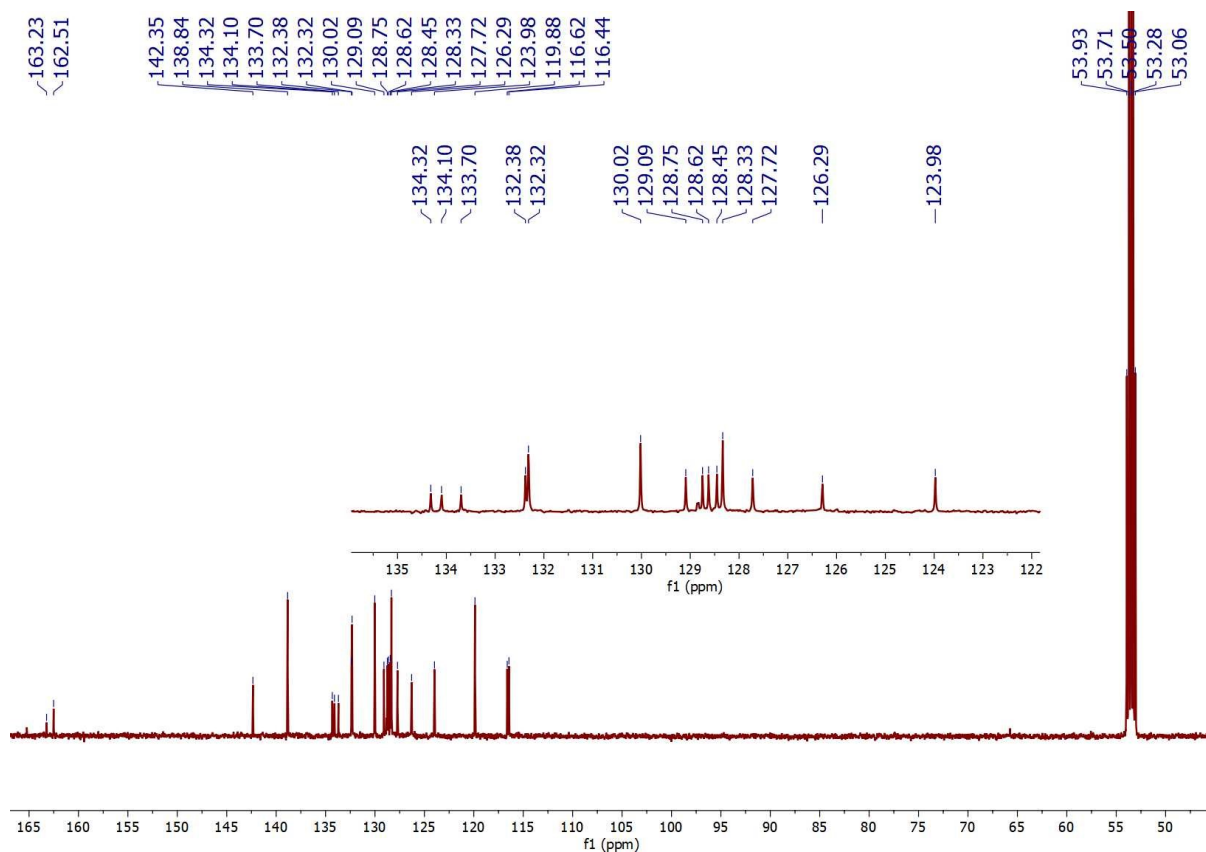
Figure S58. ^{13}C NMR spectra of synthesised **FPh-Acr-Np** in CD_2Cl_2.
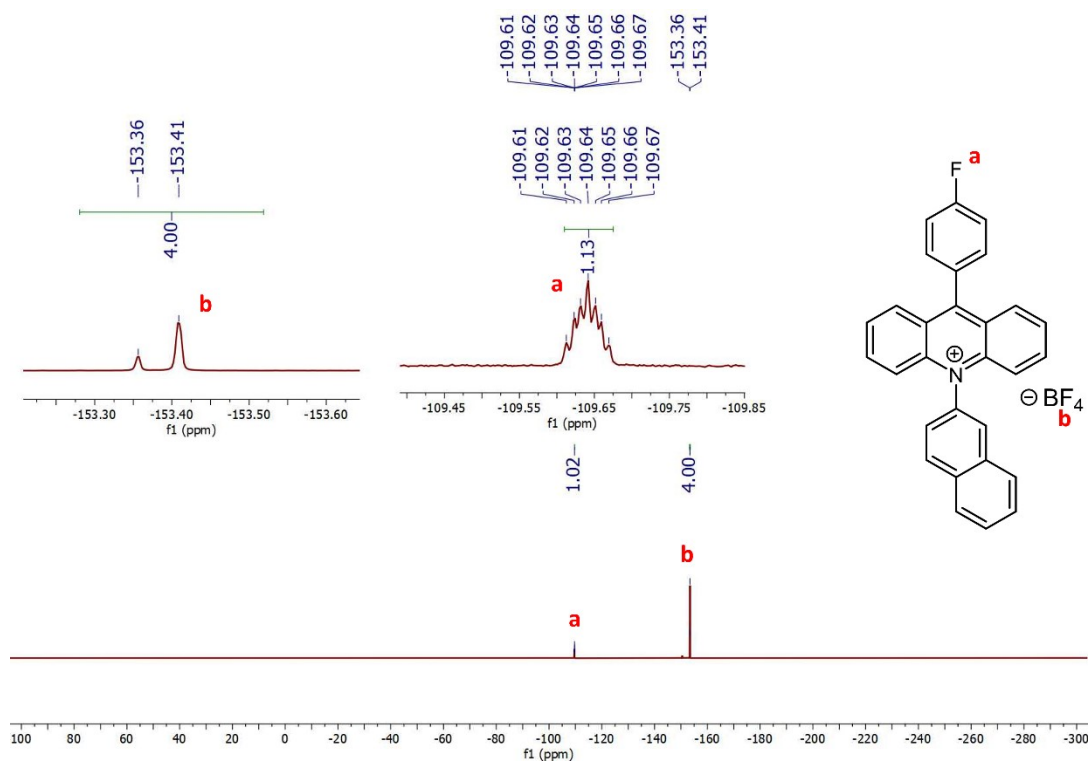
Figure S59. ^{19}F NMR spectra of synthesised **FPh-Acr-Np** in CD_2Cl_2.
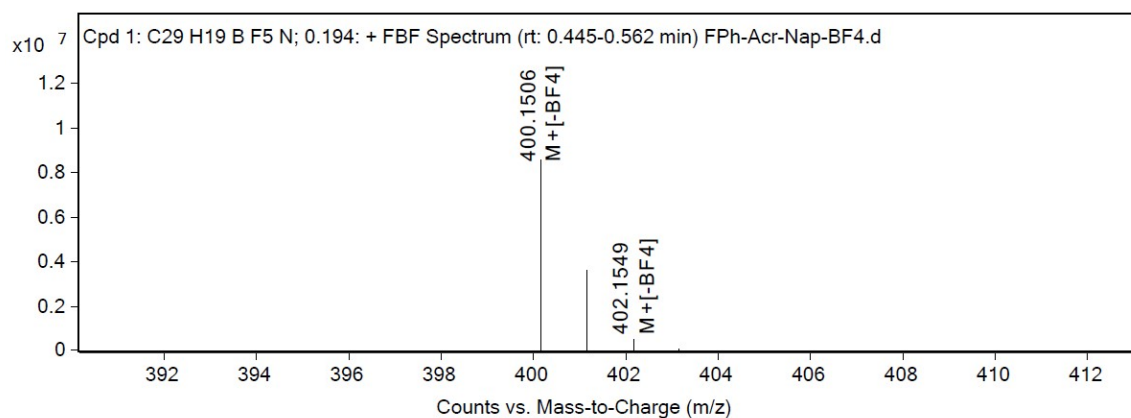
Figure S60. ESI-MS spectrum of **FPh-Acr-Np** showing the [M⁺] (without BF₄⁻) peak at m/*z* = 400.1506 (error: 0.0010 ppm).
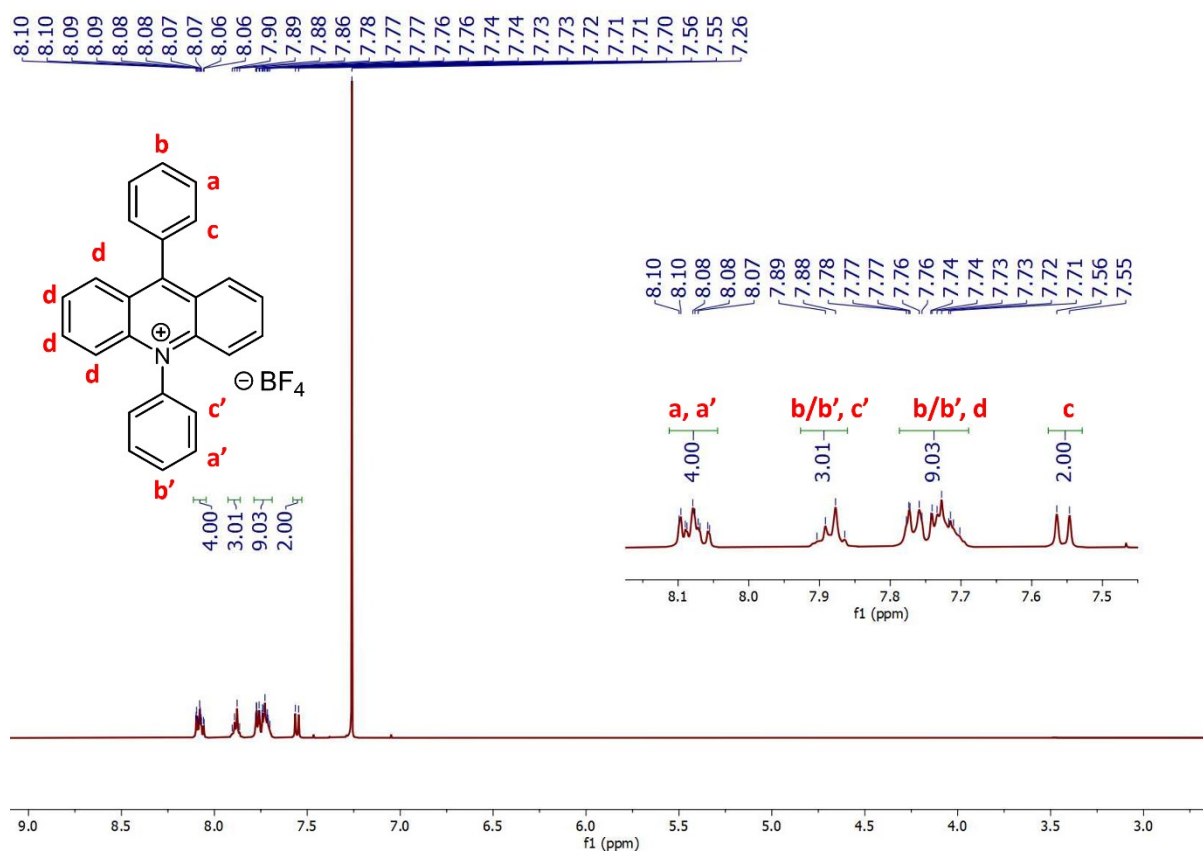
Figure S61. ¹H NMR spectra of synthesised **Ph-Acr-Ph** in CDCl₃.
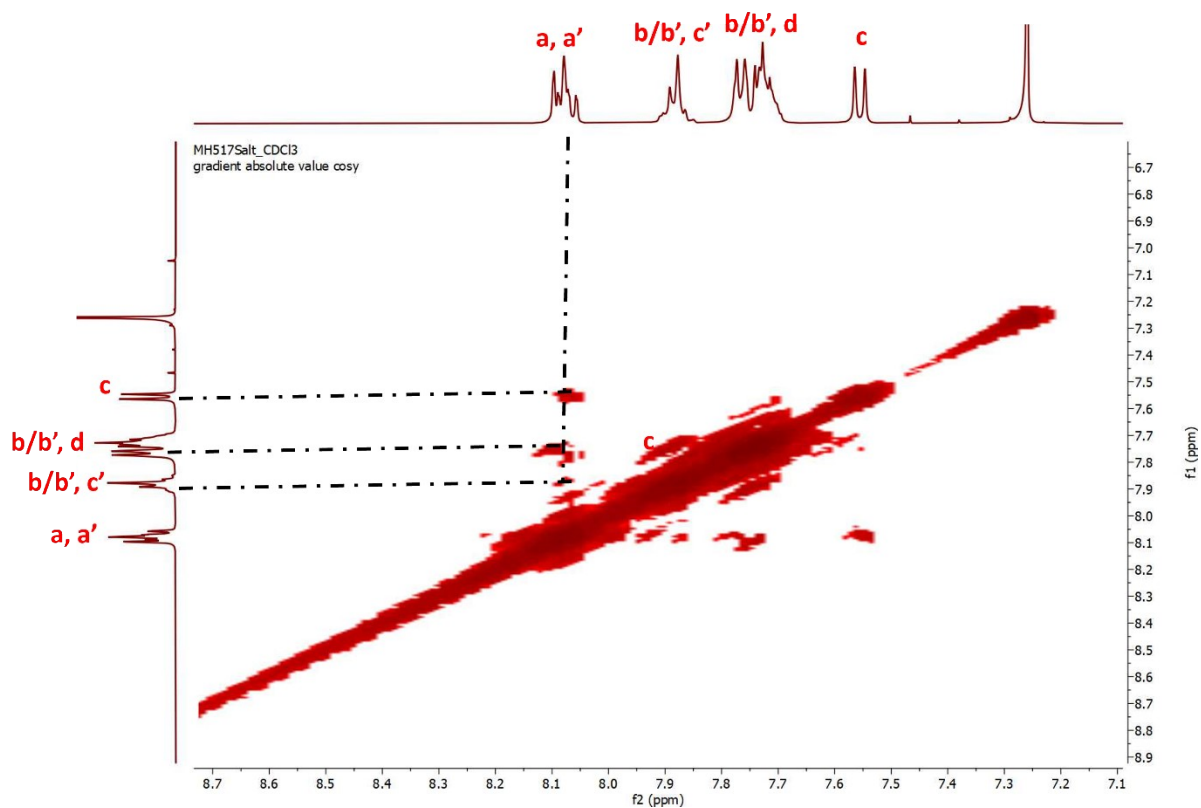
Figure S62. COSY NMR spectra of synthesised **Ph-Acr-Ph** in CDCl₃.
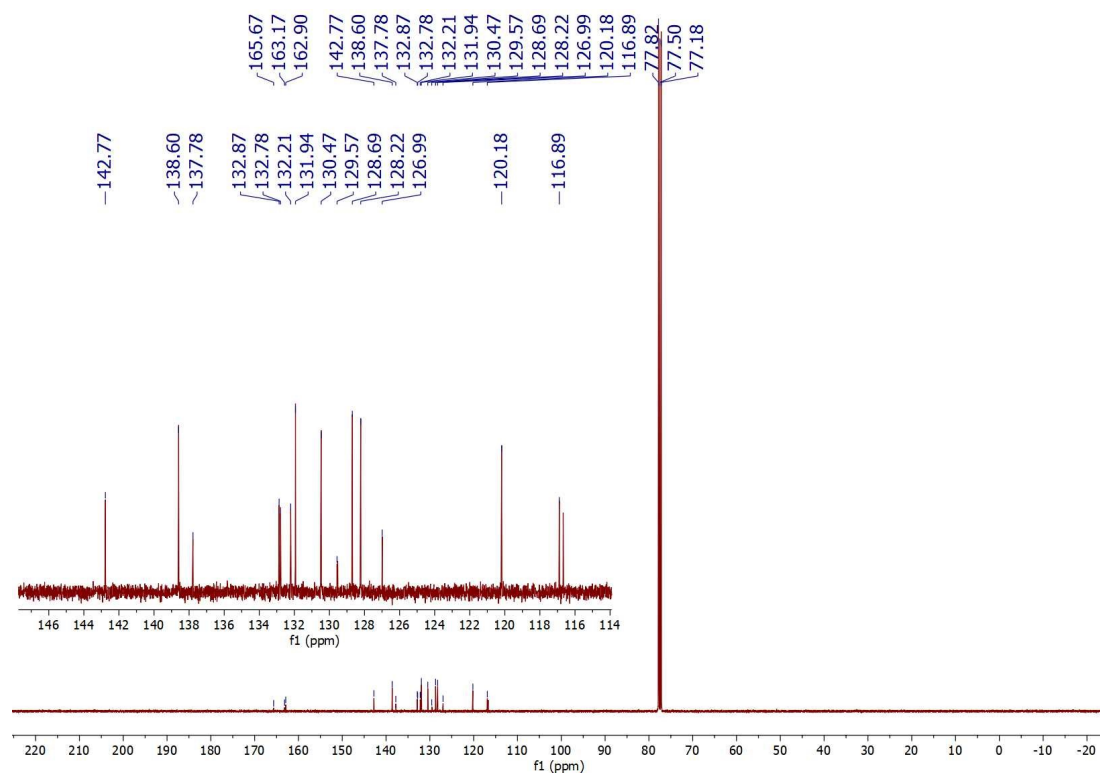
Figure S63. ^{13}C NMR spectra of synthesised **Ph-Acr-Ph** in CDCl₃.
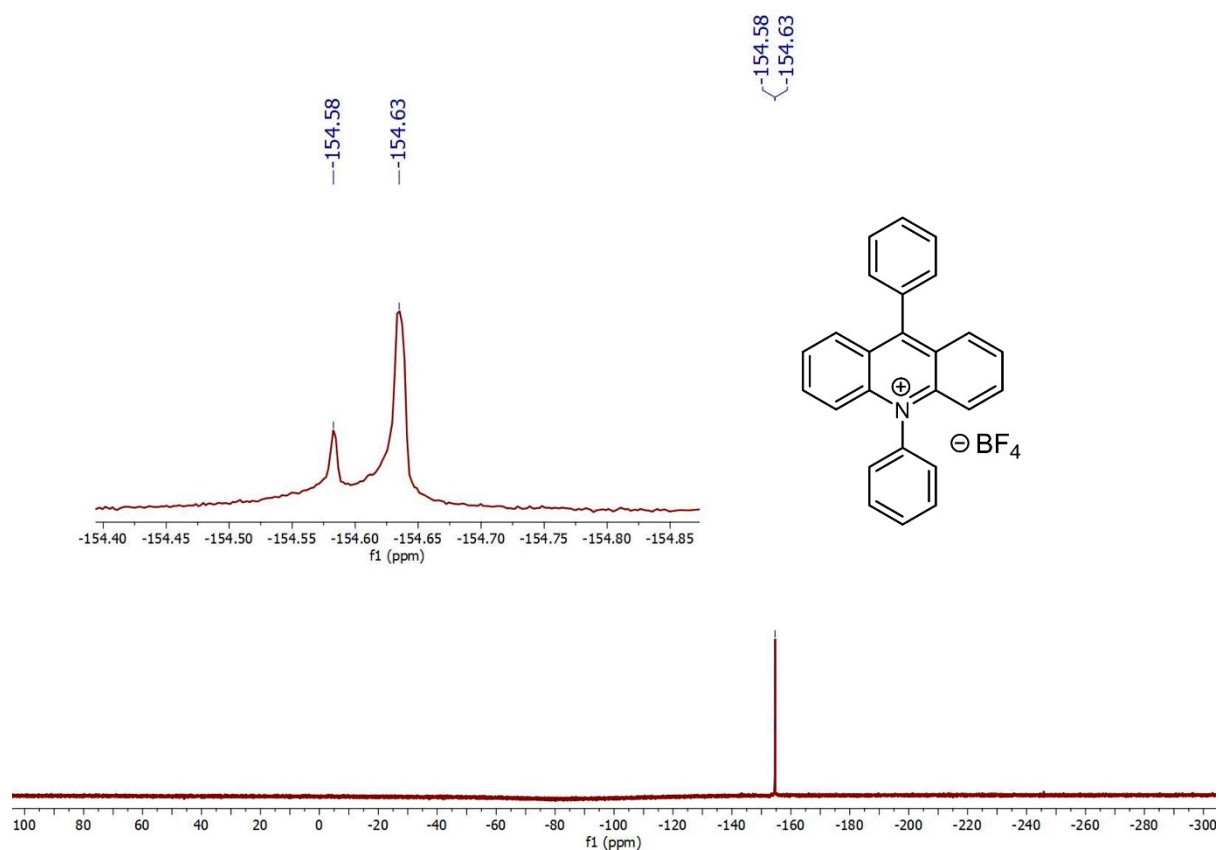
Figure S64. ^{19}F NMR spectra of synthesised **Ph-Acr-Ph** in CDCl$_3$.
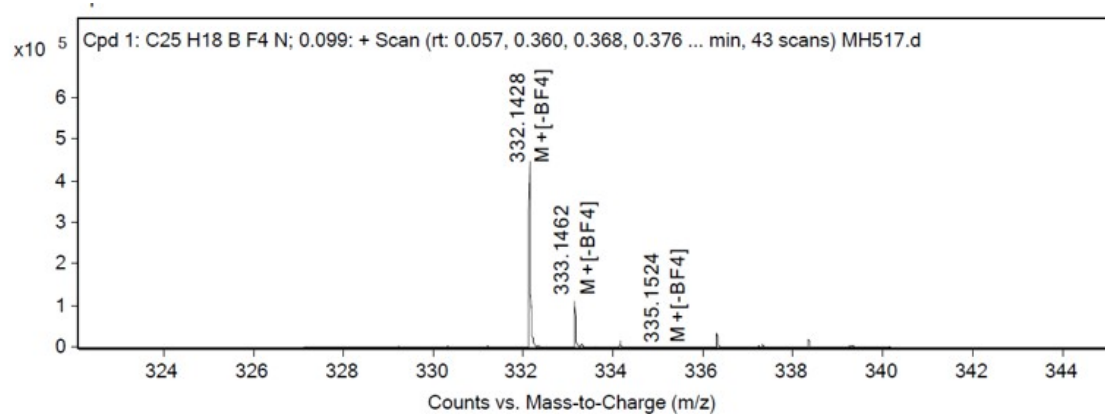
Figure S65. ESI-MS spectrum of **Ph-Acr-Ph** showing the [M$^+$] (without BF$_4^-$) peak at m/z = 332.1428 (error: 0.0006 ppm).
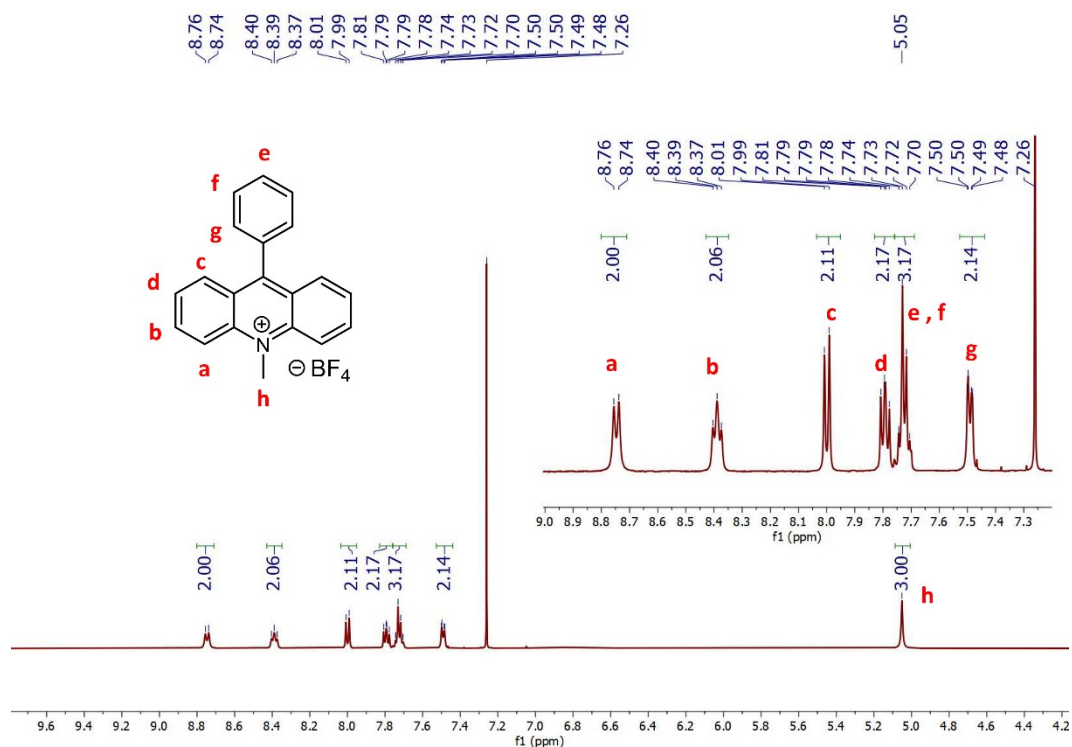
Figure S66. ^{1}H NMR spectra of synthesised **Ph-Acr-Me** in CDCl$_3$.
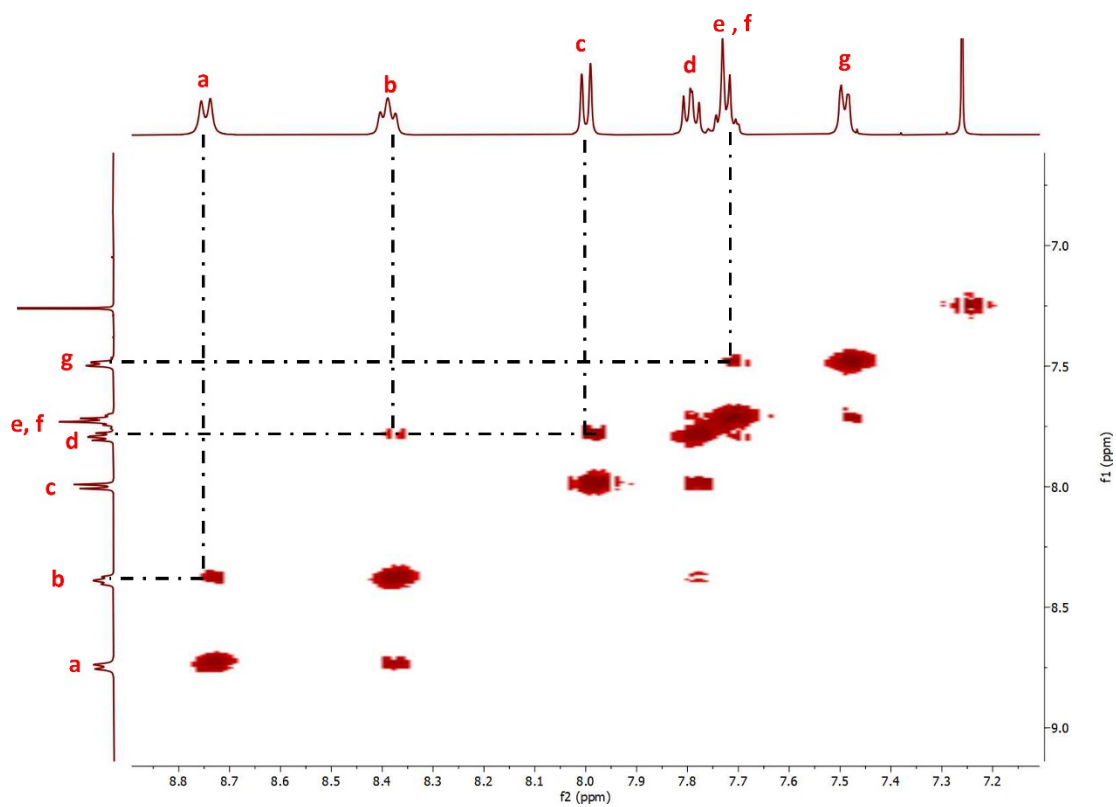
Figure S67. COSY NMR spectra of synthesised **Ph-Acr-Me** in CDCl$_3$.
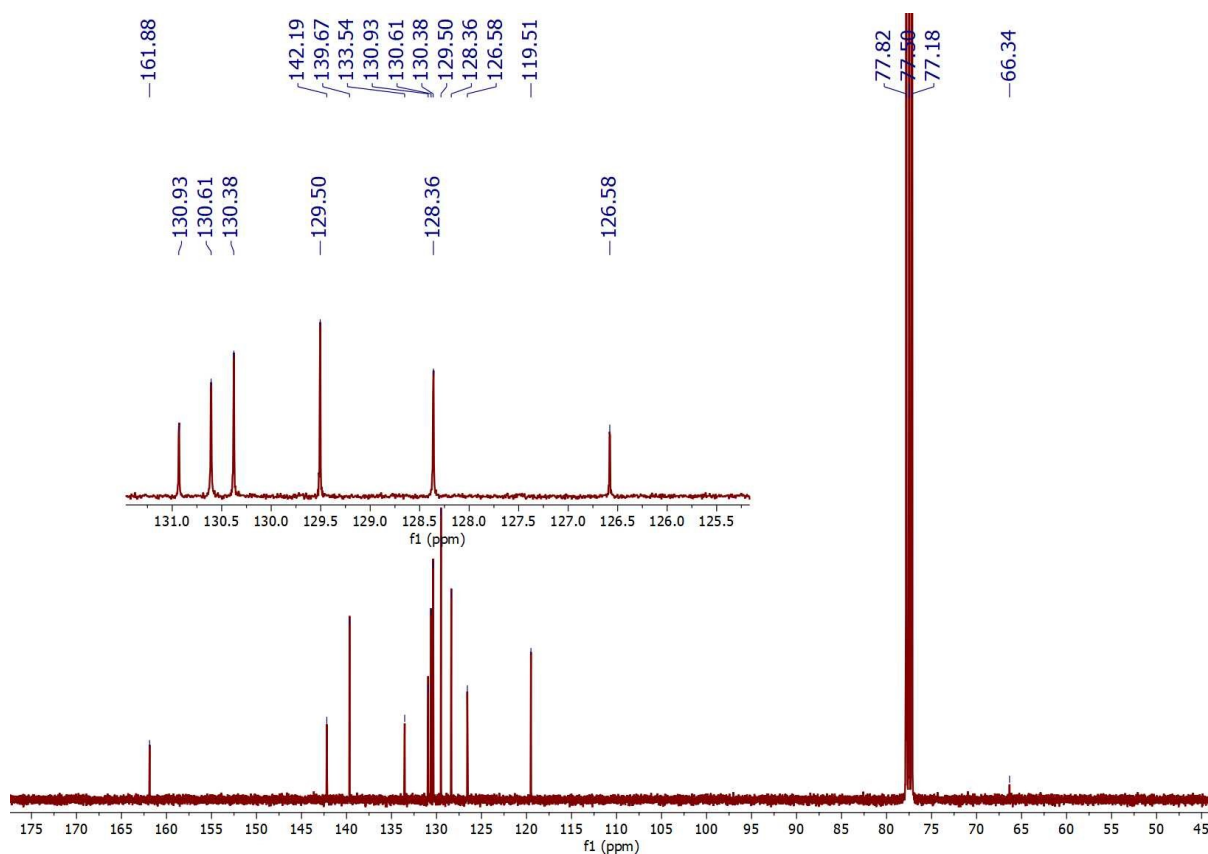
Figure S68. ^{13}C NMR spectra of synthesised **Ph-Acr-Me** in CDCl$_3$.
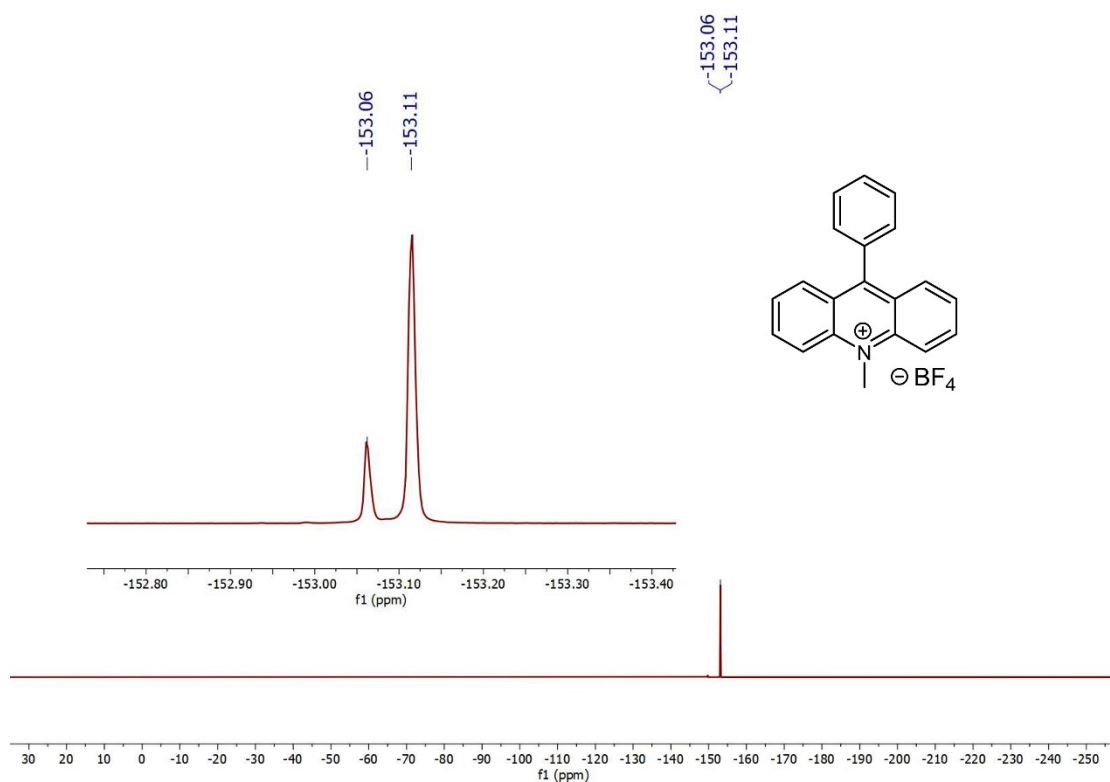
Figure S69. ^{19}F NMR spectra of synthesised **Ph-Acr-Me** in CDCl$_3$.
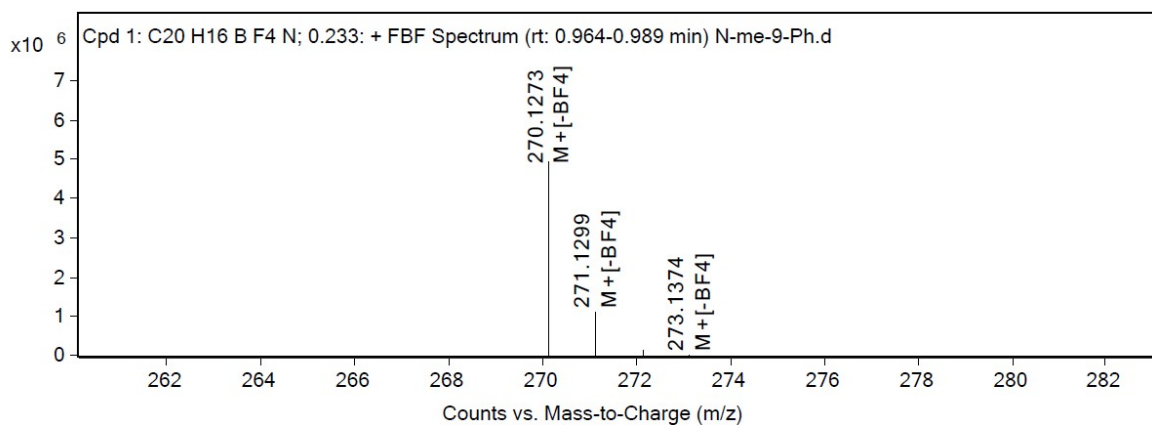
Figure S70. ESI-MS spectrum of **Ph-Acr-Me** showing the [M+] (without BF$_4^-$) peak at m/z = 270.1273 (error: 0.0004 ppm).
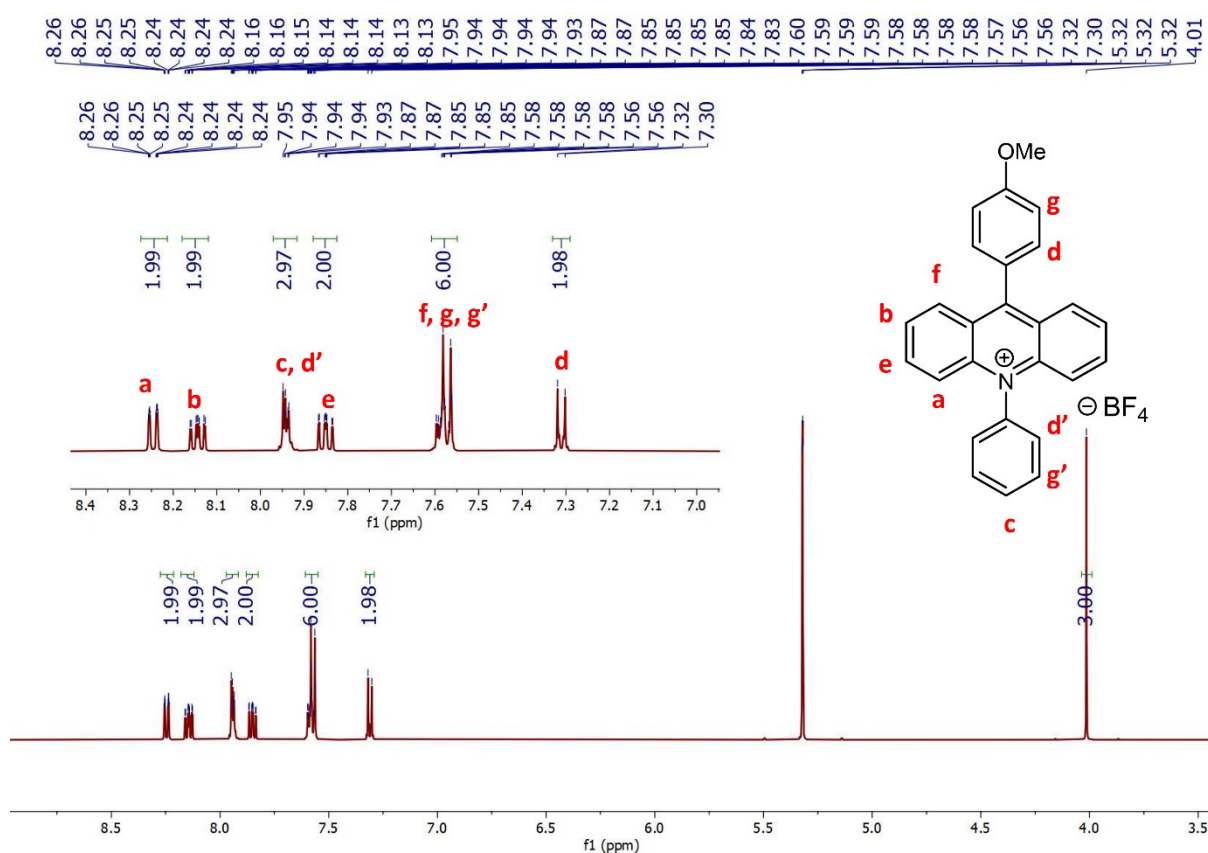
Figure S71. ^{1}H NMR spectra of synthesised **MeOPh-Acr-Ph** in CD$_2$Cl$_2$.
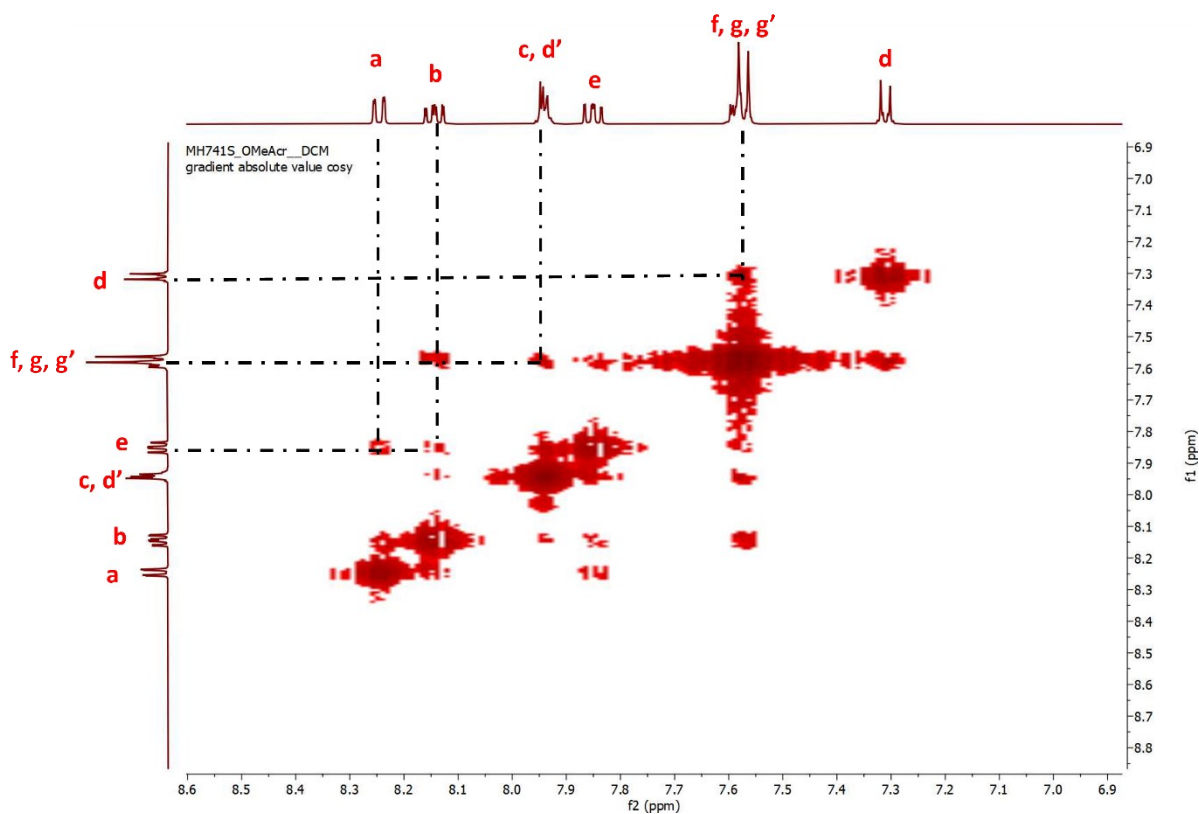
Figure S72. COSY NMR spectra of synthesised **MeOPh-Acr-Ph** in CD_2Cl_2.
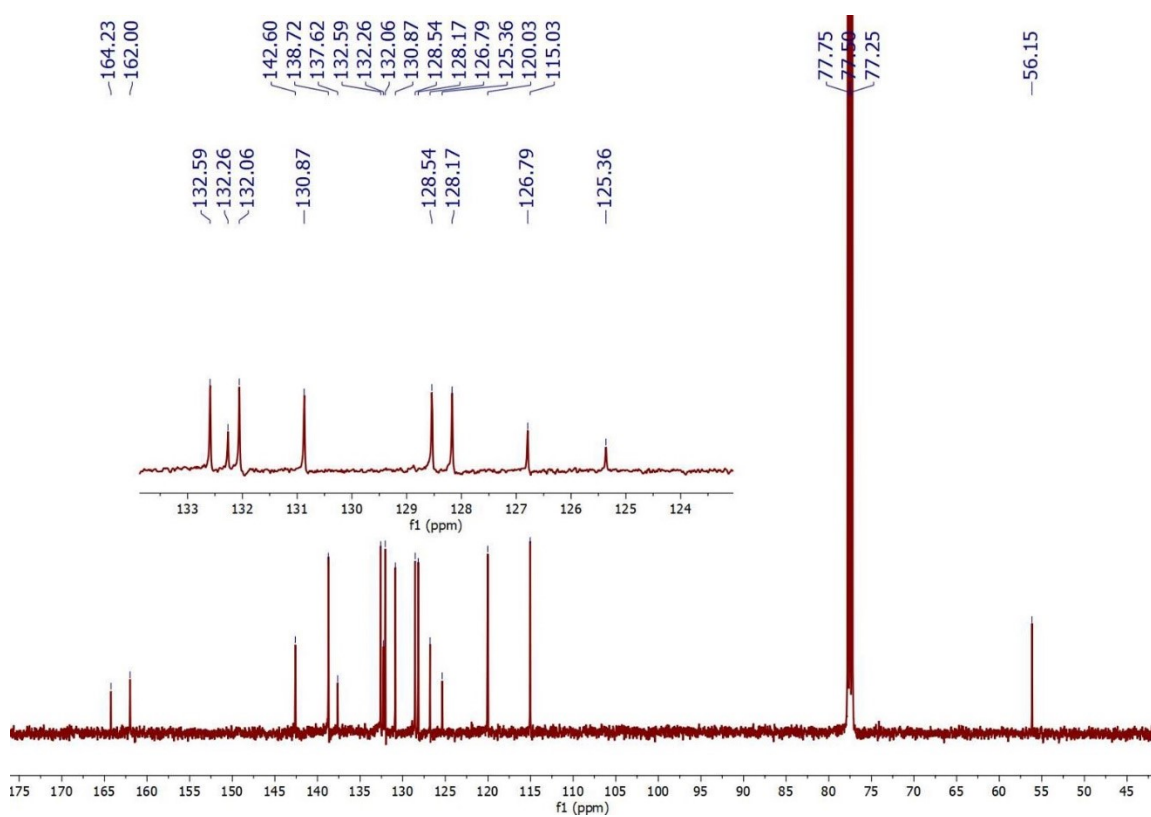
Figure S73. ^{13}C NMR spectra of synthesised **MeOPh-Acr-Ph** in $CDCl_3$.
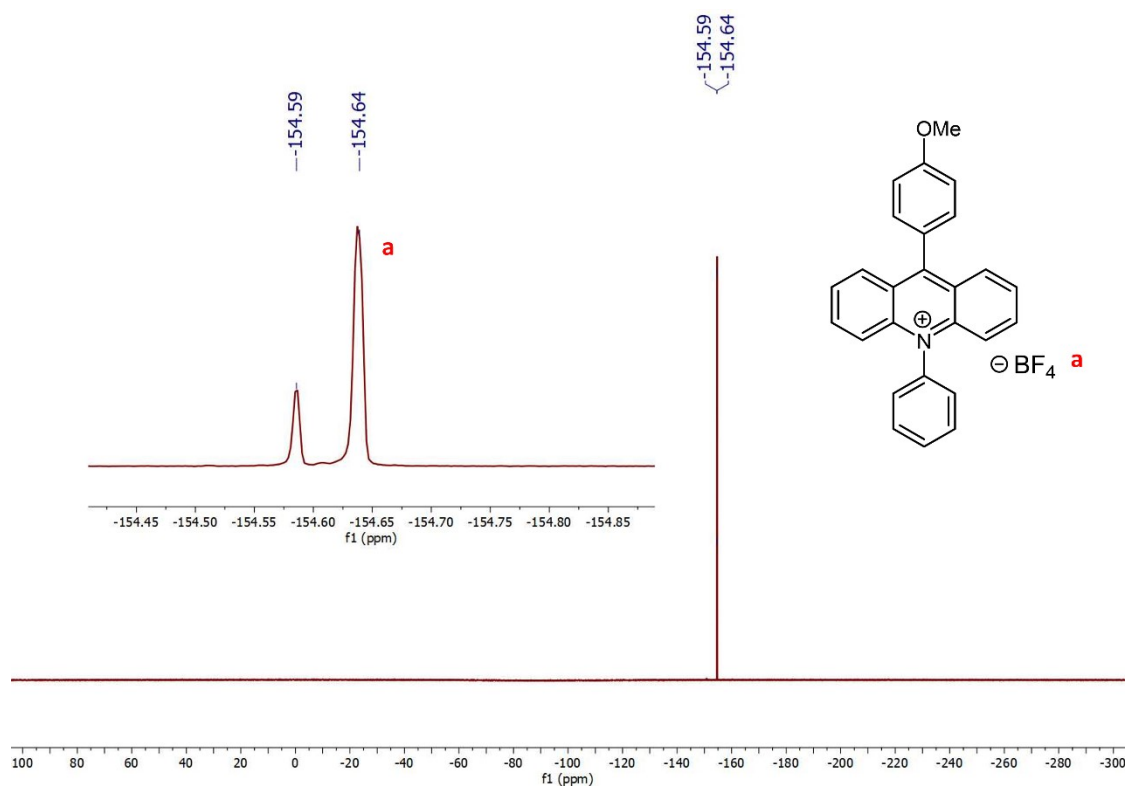
Figure S74. ^{19}F NMR spectra of synthesised **MeOPh-Acr-Ph** in CDCl$_3$
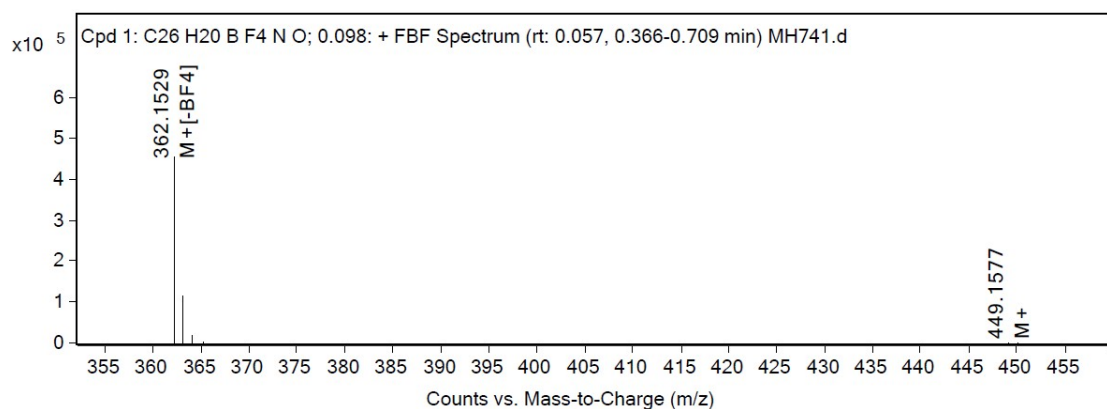
Figure S75. ESI-MS spectrum of **MeOPh-Acr-Ph** showing the [M$^+$] (without BF$_4^-$) peak at m/z = 362.1529 (error: 0.0010 ppm).
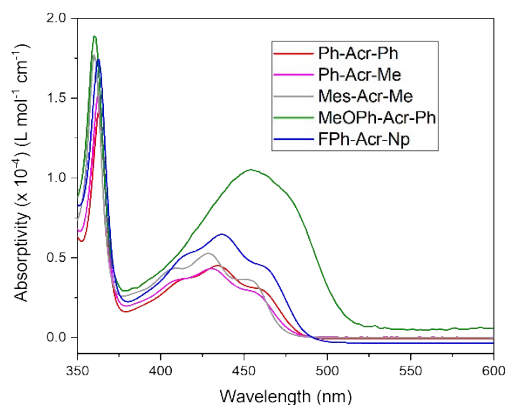
Figure S76. UV – Vis spectra for various acridinium catalysts in DCE
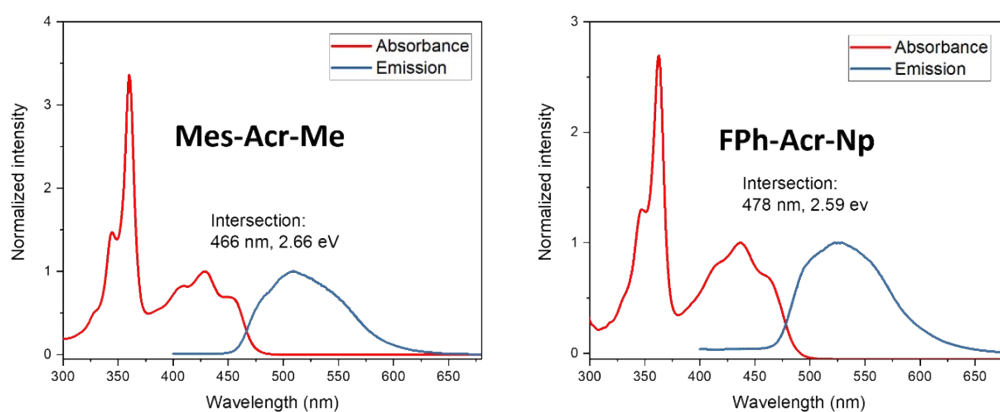
Figure S77. Absorbance spectrum (red) and emission spectra (blue) for the corresponding acridinium catalyst in DCE. Excitation energy $E_{0,0}$ was calculated based on the wavelength of the intersection of absorption and fluorescence spectra normalized to 1, following the procedure reported by Nicewicz[3].
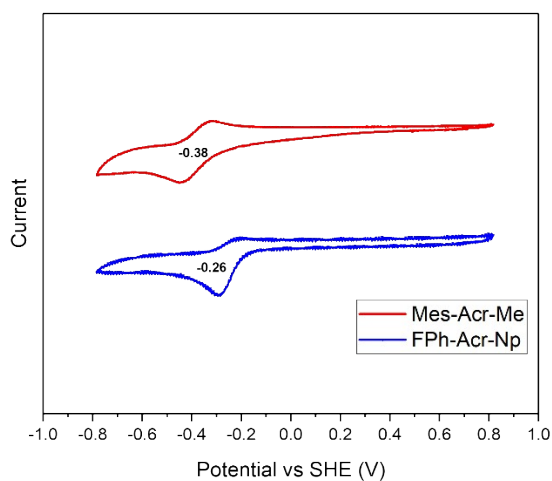
Figure S78. Cyclic voltammograms for the corresponding acridinium catalyst in DCE.
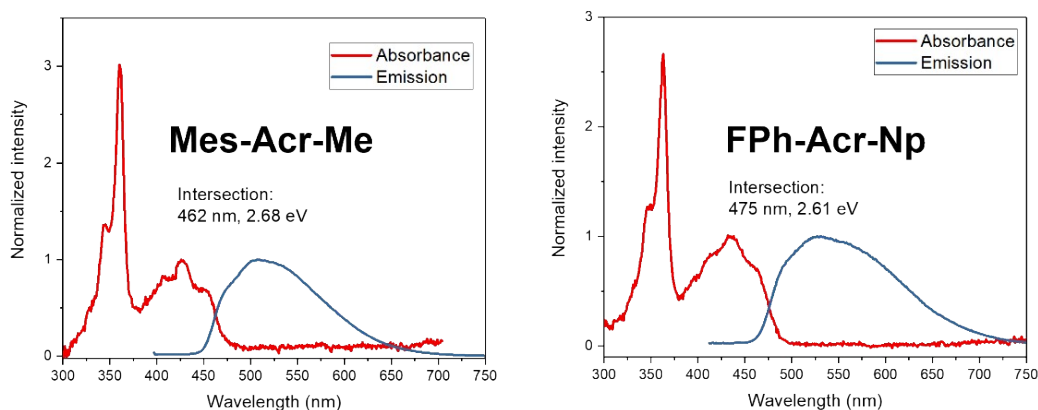
Figure S79. Absorbance spectrum (red) and emission spectra (blue) for the corresponding acridinium catalyst in a solvent mixture of DCE:MeCN (6:1). Excitation energy $E_{0,0}$ was calculated based on the wavelength of the intersection of absorption and fluorescence spectra normalized to 1 following the procedure reported by Nicewicz[3].
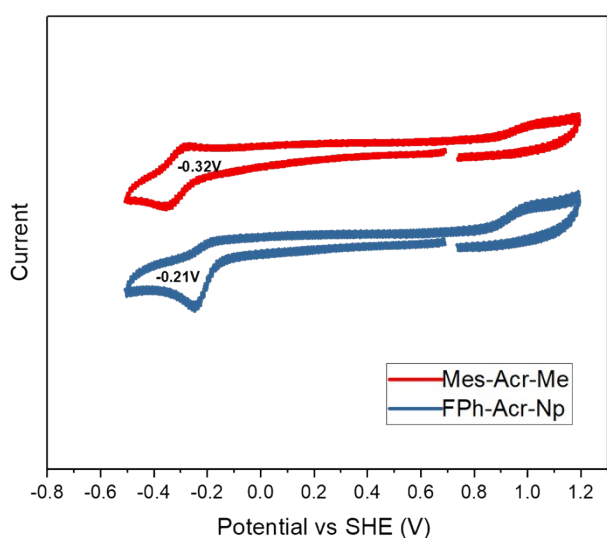
Figure S80. Cyclic voltammograms for the corresponding acridinium catalyst in a solvent mixture of DCE:MeCN (6:1).

E^*_{red} was calculated by employing the following equation[3, 4]:

$$E^*_{red} = E_{red} + E_{0,0}$$

E_{red} : Ground state reduction potential of the catalyst
$E_{0,0}$: Energy gap between the zeroth vibrational levels of the ground and excited states

Table S2: E^*_{red} for corresponding acridinium catalyst under different environments

Catalyst	Calculated E^*_{red} (V vs SHE)	Experimental E^*_{red} in DCE (V vs SHE)	Experimental E^*_{red} in 6:1 DCE: MeCN (V vs SHE)
Mes-Acr-Me	2.331	2.28[a]	2.36
FPh-Acr-Np	2.402	2.33	2.40

[a] Reported value of 2.36 V vs SHE (in MeCN)[3]

S5. Details of computational methods

To generate reasonable starting geometries for DFT optimization, meta-dynamics simulations with the semi-empirical GFN2-xTB Hamiltonian [5] were carried out to locate unique conformers for each acridinium derivative. This was done using the CREST package [6] in conjunction with the analytical linearized Poisson-Boltzmann (ALPB) implicit solvation method [7] using dichloromethane (DCM) as solvent. The lowest energy conformer corresponding to each acridinium derivative evaluated at GFN2-xTB (ALPB: DCM) was used as input geometries for S_0 (singlet), S_1 (singlet) and doublet state (TD-)DFT geometry optimizations. The levels of theory used were MN15/6-31G(d), TD-MN15/6-31G(d) and UMN15/6-31G(d) respectively, all using the SMD implicit solvation model [8] with dichloroethane (DCE) as the solvent. MN15 [9] was chosen for its general reliability in obtaining various properties relevant towards the screening parameters used in the present study [10-12]. The basis set effect was also examined, and the results given in **Table S3**. The effect of changing the basis set is effectively negligible on the difference in electronic energies (ΔE), but is slightly stronger for the TD-DFT excitation energies and oscillator strength (f). Based on its overall agreement to the most expensive aug-cc-pVTZ values, the def2-TZVP basis set was used for the calculations of the excited state properties and E_{red} (see below). All DFT calculations were carried out with Gaussian 16 [13], and the threshold of the SCF convergence was set to be "VeryTight" throughout. Frequency calculations were carried out at the optimized geometries to ensure the absence of any imaginary frequencies, and to obtain the thermodynamic contributions to the Gibbs free energy.

Table S3: Basis set effect on $\Delta E = E_{radical} - E_{S_1}$ (the difference between the electronic energies of the acridinium radical and its S_1 electronic state at their respective optimized geometries), the TD-DFT vertical excitation energies and oscillator strength (f). The vertical excitation energies and f were computed at the excited state optimized geometry of **Ph-Acr-Ph**.

	ΔE (eV)	Excitation energy (eV)	f
6-31G(d)	-0.2354	2.640	0.2553
def2-SVP	-0.2452	2.638	0.2589
def2-TZVP	-0.2431	2.583	0.2440
cc-pVDZ	-0.2413	2.619	0.2520
aug-cc-pVDZ	-0.2436	2.588	0.2438
cc-pVTZ	-0.2423	2.586	0.2437
aug-cc-pVTZ	-0.2426	2.579	0.2422

The excited state reduction potential E_{red} was calculated as:

$$E_{red} = E_{calc}^{abs} - E_{expt,ref}^{abs} = -\frac{\Delta G_{soln, calc}}{nF} - E_{expt,ref}^{abs}$$

where E_{calc}^{abs} is the calculated absolute reduction potential, $E_{expt,ref}^{abs}$ is the experimentally determined absolute reduction potential of the reference electrode (4.281 V for the standard hydrogen electrode (SHE) with the SMD solvation model), n is the number of electrons transferred, F is the Faraday constant, and $\Delta G_{soln,calc}$ is calculated as the difference between the Gibbs free energy of the two solvated species involved. For the acridinium systems, this would be the solvated acridinium radical system ($G_{radical}$) and the excited state cation (G_{S_1}).[14, 15]:

$$\Delta G_{soln,calc} = G_{radical} - G_{S_1}$$

The calculated value of E_{red} (Acr^{+*}) for the Fukuzumi catalyst (**Mes-Acr-Me**) was found to be in excellent agreement with the literature (Present calc. 2.33 V, expt. 2.36 V [3] both with respect to SHE), and supports the computational protocol used in this work. The reduction potential for the pentan-3-nyl

cation used to model PS was calculated similarly using ΔG between the solvated pentan-3-nyl cation ($G_{pentan-3-nyl^+}$) and neutral molecule ($G_{pentan-3-nyl}$):

$$\Delta G_{soln,calc} = G_{pentan-3-nyl^+} - G_{pentan-3-nyl}$$

For the **Cl⁻** anion, ΔG was calculated directly as the difference in electronic energies of the solvated anion (E_{Cl^-}) and the neutral radical ($E_{Cl\cdot}$):
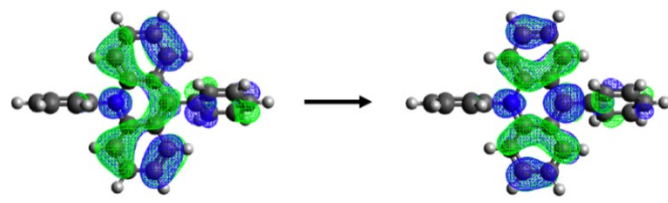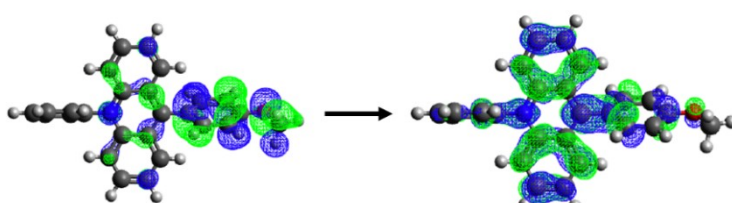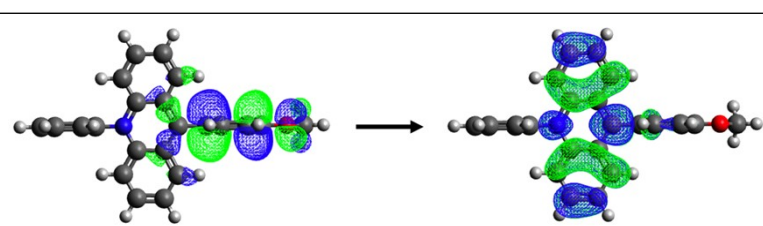
$$\Delta G_{soln,calc} = E_{Cl^-} - E_{Cl\cdot}.$$

A comparison of the TD-DFT results for the initial test set (Entries 1-3 in the **Table S4**) to the experimental UV-vis spectrum reveals that the computational values of λ_{abs} are systematically red-shifted by about 20 nm compared to experiment. Hence, the experimental band maxima can be approximated using the systematic error of the computed value of $\lambda_{abs.}$ and is further validated by the results for the other two acridinium systems examined in this study (Entries 4 and 5).

Table S4: Comparison of the TD-DFT values of λ_{abs} (nm) to the wavelength of the absorption band maxima corresponding to the $S_0 \rightarrow S_1$ electronic transition.

S/N	Acridinium catalyst	Computed λ_{abs} (nm)	Experimental band maximum for (nm)
1	Ph-Acr-Ph	409	434
2	Ph-Acr-Me	407	430
3	Mes-Acr-Me	407	429
4	MeOPh-Acr-Ph	435	454
5	FPh-Acr-Np	412	435

Natural transition orbitals for the S_1 excited state of the acridiniums

Photocatalyst	Excitation type	Natural transition orbitals
Ph-Acr-Ph	Locally excited	
MeOPh-Acr-Ph (S₀ optimized geometry)	Charge transfer	
MeOPh-Acr-Ph (S₁ optimized geometry)	Charge transfer	

Figure S81. Natural transition orbitals corresponding to the S_1 state of **Ph-Acr-Ph** and **MeOPh-Acr-Ph** at the S_0 optimized geometry. The second entry for **MeOPh-Acr-Ph** is for the S_1 optimized geometry.

Results for all molecules screened in the current work
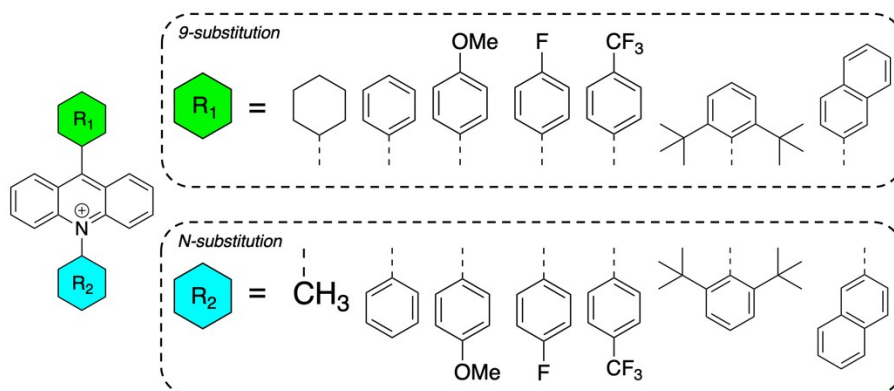
Figure S82: All substituents considered at *9-* and *N-* position for DFT computations for a total of 64 unique acridinium derivatives.

Table S5: DFT/TD-DFT results for λ_{abs} (nm), f_{abs}, and E_{red} (Acr^{+*}) for all molecules examined in the present study

Catalyst	λ_{abs} **(nm)**	f_{abs}	E_{red} **(Acr^{+*}) / V**
Ph-Acr-Ph	409	0.2221	2.343
Ph-Acr-Me	407	0.1840	2.375
Ph-Acr-MeOPh	409	0.2351	2.345
Ph-Acr-FPh	409	0.2214	2.423
Ph-Acr-Mes	409	0.2321	2.417
Ph-Acr-PhditBu	412	0.2125	2.375
Ph-Acr-Np	410	0.2619	2.387
Ph-Acr-CF$_3$Ph	410	0.2274	2.421
Cy-Acr-Ph	400	0.1705	2.382
Cy-Acr-Me	401	0.1414	2.374
Cy-Acr-MeOPh	400	0.1804	2.312
Cy-Acr-FPh	400	0.1685	2.405
Cy-Acr-Mes	400	0.1783	2.377
Cy-Acr-Phditbu	403	0.1571	2.319
Cy-Acr-Np	401	0.2021	2.368
Cy-Acr-CF$_3$Ph	401	0.1724	2.418
MeOPh-Acr-Ph	435	0.3519	2.183
MeOPh-Acr-Me	433	0.3020	2.152
MeOPh-Acr-MeOPh	434	0.3650	2.174
MeOPh-Acr-FPh	436	0.3519	2.189
MeOPh-Acr-Mes	435	0.3618	2.160
MeOPh-Acr-PhditBu	439	0.3518	2.171

MeOPh-Acr-Np	436	0.3953	2.171
MeOPh-Acr-CF$_3$Ph	438	0.3590	2.207
FPh-Acr-Ph	411	0.2337	2.390
FPh-Acr-Me	409	0.1942	2.384
FPh-Acr-MeOPh	411	0.2462	2.353
FPh-Acr-FPh	411	0.2335	2.430
FPh-Acr-Mes	411	0.2435	2.411
FPh-Acr-PhditBu	414	0.2234	2.371
FPh-Acr-Np	412	0.2740	2.402
FPh-Acr-CF$_3$Ph	412	0.2401	2.427
Mes-Acr-Ph	399	0.1666	2.324
Mes-Acr-Me	398	0.1362	2.331
Mes-Acr-MeOPh	399	0.1656	2.303
Mes-Acr-FPh	399	0.1647	2.331
Mes-Acr-Mes	399	0.1740	2.326
Mes-Acr-PhditBu	402	0.1501	2.301
Mes-Acr-Np	400	0.1975	2.243
Mes-Acr-CF$_3$Ph	400	0.1632	2.295
Phditbu-Acr-Ph	406	0.1544	2.433
Phditbu-Acr-Me	404	0.1243	2.456
Phditbu-Acr-MeOPh	405	0.1639	2.383
Phditbu-Acr-FPh	406	0.1526	2.464
Phditbu-Acr-Mes	406	0.1617	2.389
Phditbu-Acr-PhditBu	409	0.1411	2.432
Phditbu-Acr-Np	406	0.1856	2.398
Phditbu-Acr-CF$_3$Ph	407	0.1541	2.526
Np-Acr-Ph	435	0.2301	2.258
Np-Acr-Me	432	0.1886	2.232
Np-Acr-MeOPh	433	0.2448	2.249
Np-Acr-FPh	436	0.2213	2.263
Np-Acr-Mes	434	0.2394	2.215
Np-Acr-Phditbu	437	0.2221	2.246
Np-Acr-Np	435	0.2508	2.245
Np-Acr-CF$_3$Ph	439	0.2126	2.307
CF$_3$Ph-Acr-Ph	408	0.1935	2.400
CF$_3$Ph-Acr-Me	406	0.1604	2.432
CF$_3$Ph-Acr-MeOPh	408	0.2052	2.387
CF$_3$Ph-Acr-FPh	408	0.1919	2.465
CF$_3$Ph-Acr-Mes	408	0.2029	2.464
CF$_3$Ph-Acr-Phditbu	411	0.1868	2.471
CF$_3$Ph-Acr-Np	409	0.2320	2.412
CF$_3$Ph-Acr-CF$_3$Ph	409	0.1963	2.485

Discussion on the photophysical behaviour of MeOPh-Acr-Ph

The TD-DFT results for **MeOPh-Acr-Y** family of catalysts was observed to be quite distinct from the other screened photocatalyst candidates (see **Table S5** above). Although they have the highest

computed values of f_{abs}, their values of λ_{abs} exhibit a red-shift of about 20-30 nm compared to the other acridinium systems examined. Their computed E_{red} (Acr^{+*}) values are also lower than E_{ox}(PS) but is sufficient to oxidise the Cl$^-$ ion.

After synthesis and testing, the observed BA yield of **MeOPh-Acr-Ph** system was found to be zero. In addition, **MeOPh-Acr-Ph*** was observed to only fluoresce in the solid-state, but not in solution. As shown by its experimental absorption spectra (**Figure S76**), **MeOPh-Acr-Ph** is still capable of absorbing light strongly at the wavelength of the exciting lasers used in this project, which shows that the red-shift in λ_{abs} does not affect the photoexcitation of **MeOPh-Acr-Ph**. Thus, the excitation energy in **MeOPh-Acr-Ph*** after absorption must be lost through some other excited state relaxation process besides fluorescence.

First, the absence of fluorescence in solution can be explained by the oscillator strength at the S_1 optimized geometry, which was found to be zero. After electronic excitation to the S_1 state, the C-C bond at the 9- position linking the MeOPh- substituent to the main acridinium ring rotates such that the two rings become perpendicular to each other (**Figure S83**). At this geometry, there is thus negligible overlap between the orbitals involved in the excitation (**Figure S81**), which explains the zero oscillator strength.

However, in the solid phase, the tighter packing of the individual molecules means that the C-C bond at the 9- position cannot rotate freely to reach the perpendicular conformation in **Figure S83**. As a result, **MeOPh-Acr-Ph*** will be able to lose its excitation energy through fluorescence.

	S_0	S_1
Top view		
End view		
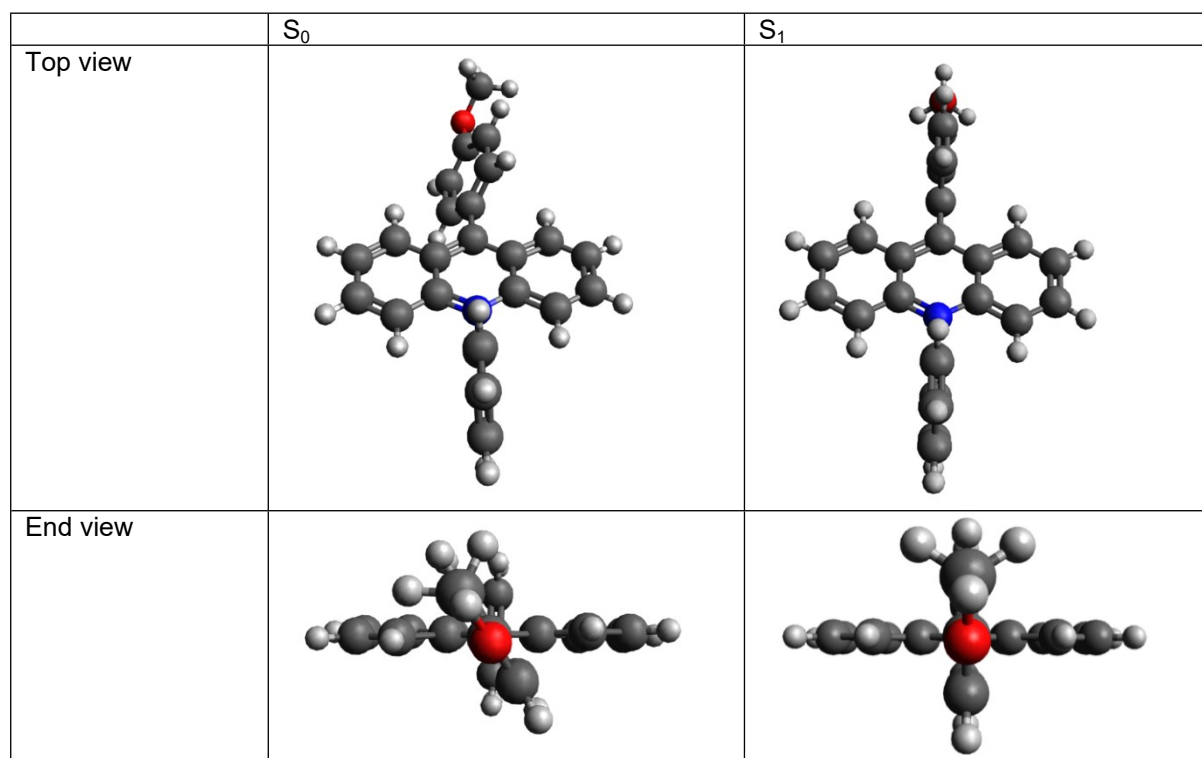
Figure S83. Top and end views of the S_0 and S_1 optimized geometries of **MeOPh-Acr-Ph**

There is still the question of how **MeOPh-Acr-Ph*** loses its excitation energy in solution. Although its calculated value of E_{red} (Acr^{+*}) is lower than E_{ox}(PS), it is still sufficient to oxidize a **Cl$^-$** ion to a **Cl·** radical (Cycle 2), which should be sufficient to trigger the formation of the benzylic radical, and eventually benzoic acid. But the observed 0% BA yield suggests that **MeOPh-Acr-Ph*** does not react at all and loses its energy elsewhere.

To further investigate this, the rates of fluorescence (k_{rad}), intersystem crossing (k_{ISC}), and internal conversion (k_{IC}) of the S_1 state in **MeOPh-Acr-Ph** were calculated using FCclasses 3.0 [16] with the TD formalism and the adiabatic Hessian model.[17] The non-adiabatic coupling between the S_0 and S_1 electronic states was computed at the S_1 minimum geometry using Gaussian 16. The results are given in **Table S6**.

Table S6: Excited state relaxation processes of **MeOPh-Acr-Ph***. All values are in 10^9 s^{-1}. The SOC parameters were computed using ORCA 5.0.3 [18, 19] using the spin-orbit mean-field approximation.[20]

	k_{rad}	k_{ISC} ($S_1{\rightarrow}T_1$)	k_{ISC} ($S_1{\rightarrow}T_2$)	k_{IC}
MeOPh-Acr-Ph	0.0	0.00024	0.000009	6.8

First, the rate of fluorescence for **MeOPh-Acr-Ph*** in solvent is zero because of its zero oscillator strength. Similarly, the rates of intersystem crossing to the lowest two triplet states (T_1 and T_2) were found to be effectively zero too. On the other hand, the rate of internal conversion was found to be fast, on the order of 10^9 s^{-1}. In contrast, literature values for the electron transfer rate between an acridinium catalyst and Cl$^-$ are on the order of 10^8 s^{-1} [21, 22], an order of magnitude smaller than the calculated value of k_{IC}. Hence, the facile internal conversion of **MeOPh-Acr-Ph*** significantly outpaces the electron transfer process between **MeOPh-Acr-Ph*** and the **Cl$^-$** anion, resulting in 0% BA yield.

In summary, because of its lower E_{red} (Acr^{+*}) value, **MeOPh-Acr-Ph** is unable to oxidise PS, only Cl$^-$. However, the rate of electron transfer between **MeOPh-Acr-Ph** and Cl$^-$ is likely to be too slow to compete with internal conversion, which is the main relaxation process of **MeOPh-Acr-Ph*** in solution. Hence, despite being capable of absorbing light strongly, there was no BA yield observed for **MeOPh-Acr-Ph**. This was consistent with GPC analysis whereby PS chain cleavage was still observed, indicating some catalytic activity from the combination of **MeOPh-Acr-Ph** and HCl but no BA was eventually formed (**Figure S43, S45**).

S6. Comparisons of Catalyst Performance

Table S7. Comparison of the catalytic efficacy of different photo-catalysts for PS oxidative degradation to small molecule oxygenated aromatics.

Catalyst[a]	Reaction conditions	T/ °C	Duration/ h	Atm	Organic Products	TON[b]	Ref.
Homogeneous catalysis							
FPh-Acr-Np (5 mol%)	DCE/MeCN 6:1, HCl (200 mol%), 390 nm	R.T.	24	O_2 (1 bar)	BA (55 %)	11	This work
$FeCl_3$ (20 wt% = 12.8 mol%)	Acetone, white LED	R.T.	20	Air (1 bar)	BA + benzoyl chloride + acetophenone (total yield = 11.3 %)	0.88	[23]
NBS (15 mol%), CF_3SO_2Na (50 mol%)	EtOAc, 390 nm	R.T.	16	O_2 (1 bar)	BA (68 %)	4.5	[24]
p-TsOH·H_2O (5 mol%)	Benzene/ MeCN 1:1, 405 nm	R.T.	15	O_2 (1 bar)	BA (50 %)	10	[25]
Fluorenone (20 mol%)	EtOAc, blue LED, H_2SO_4 (100 mol%)	50	48	O_2 (1 bar)	BA (38 ± 3 %)	1.9	[26]
Heterogeneous catalysis							
TiO_2 (50 mg) for 20 mg PS	MeCN, Xe lamp	80	24	Air (1 bar)	BA + acetophenone + benzaldehyde (13 ± 1 % conversion)	-	[27]
ZnO (50 mg) for 20 mg PS	MeCN, Xe lamp	80	24	Air (1 bar)	BA + acetophenone + benzaldehyde (21 ± 2 % conversion)	-	[27]
ZnS (50 mg) for 20 mg PS	MeCN, Xe lamp	80	24	Air (1 bar)	BA + acetophenone + benzaldehyde (12 ± 1 % conversion)	-	[27]
Graphitic carbon nitrite (C_3N_4) (40 wt%)	MeCN, Xe lamp	150	20 cycles x 8 h/cycle	O_2 (10 bar)	BA (74 %) + acetophenone (15 %) + benzaldehyde (11 %)	-	[27]
Potassium stearate-modified TiO_2 (10 mg for 10.4 mg PS)	DCM, 370 nm	R.T.	4	O_2 (1 bar)	BA (43.5 %)	-	[28]

[a] All mol% loadings are w.r.t. the number of moles of styrene monomer units present.

[b] Calculated using

$$TON = \frac{No.\ of\ moles\ of\ oxygenated\ aromatic\ products\ (i.e.\ percentage\ yield)}{catalyst\ loading\ (mol\ \%)}$$

S7. References

1.   Dubrovskiy, A. V.; Larock, R. C., Synthesis of o-(Dimethylamino)aryl Ketones, Acridones, Acridinium Salts, and 1H-Indazoles by the Reaction of Hydrazones and Arynes. *The Journal of Organic Chemistry* **2012,** *77* (24), 11232-11256.

2.   Cao, Y. X.; Zhu, G.; Li, Y.; Le Breton, N.; Gourlaouen, C.; Choua, S.; Boixel, J.; Jacquot de Rouville, H. P.; Soule, J. F., Photoinduced Arylation of Acridinium Salts: Tunable Photoredox Catalysts for C-O Bond Cleavage. *J Am Chem Soc* **2022,** *144* (13), 5902-5909.

3.   Romero, N. A.; Nicewicz, D. A., Mechanistic insight into the photoredox catalysis of anti-markovnikov alkene hydrofunctionalization reactions. *J Am Chem Soc* **2014,** *136* (49), 17024-35.

4.   Jr., W. E. J.; Fox, M. A., Determination of Excited-State Redox Potentials by Phase-Modulated Voltammetry. *J. Phys. Chem.* **1994,** *98*, 5095–5099.

5.   C. Bannwarth, S. E., S. Grimme, GFN2-xTB—An Accurate and Broadly Parametrized Self-Consistent Tight-Binding Quantum Chemical Method with Multipole Electrostatics and Density-Dependent Dispersion Contributions. *J. Chem. Theory Comput.* **2019,** *15*, 1652–1671.

6.   Pracht, P.; Bohle, F.; Grimme, S., Automated exploration of the low-energy chemical space with fast quantum chemical methods. *Phys Chem Chem Phys* **2020,** *22* (14), 7169-7192.

7.   S. Ehlert, M. S., S. Spicher and S. Grimme, Robust and Efficient Implicit Solvation Model for Fast Semiempirical Methods. *J. Chem. Theory Comput.* **2021,** *17*, 4250–4261.

8.   A. V. Marenich, C. J., Cramer, D. G. Truhlar, Universal Solvation Model Based on Solute Electron Density and on a Continuum Model of the Solvent Defined by the Bulk Dielectric Constant and Atomic Surface Tensions. *J. Phys. Chem. B* **2009,** *113*, 6378–6396.

9.   H. S. Yu, X. H., S. L. Li, D. G. Truhlar, MN15: A Kohn-Sham global-hybrid exchange-correlation density functional with broad accuracy for multi-reference and single-reference systems and noncovalent interactions. *Chem. Sci.* **2016,** *7*, 5032–5051.

10.   Liang, J.; Feng, X.; Hait, D.; Head-Gordon, M., Revisiting the Performance of Time-Dependent Density Functional Theory for Electronic Excitations: Assessment of 43 Popular and Recently Developed Functionals from Rungs One to Four. *J Chem Theory Comput* **2022,** *18* (6), 3460-3473.

11.   Mardirossian, N.; Head-Gordon, M., Thirty years of density functional theory in computational chemistry: an overview and extensive assessment of 200 density functionals. *Molecular Physics* **2017,** *115* (19), 2315-2372.

12.   Mardirossian, N.; Head-Gordon, M., How Accurate Are the Minnesota Density Functionals for Noncovalent Interactions, Isomerization Energies, Thermochemistry, and Barrier Heights Involving Molecules Composed of Main-Group Elements? *J Chem Theory Comput* **2016,** *12* (9), 4303-25.

13.   M. J. Frisch, G. W. T., H. B. Schlegel, G. E. Scuseria, M. A. Robb, J. R. Cheeseman, G. Scalmani, V. Barone, G. A. Petersson, H. Nakatsuji, X. Li, M. Caricato, A. V. Marenich, J. Bloino, B. G. Janesko, R. Gomperts, B. Mennucci, H. P. Hratchian, J. V. Ortiz, A. F. Izmaylov, J. L. Sonnenberg, D. Williams-Young, F. Ding, F. Lipparini, F. Egidi, J. Goings, B. Peng, A. Petrone, T. Henderson, D. Ranasinghe, V. G.; Zakrzewski, J. G., N. Rega, G. Zheng, W. Liang, M. Hada, M. Ehara, K. Toyota, R. Fukuda, J. Hasegawa, M. Ishida, T. Nakajima, Y. Honda, O. Kitao, H. Nakai, T. Vreven, K. Throssell, J. A. Montgomery, Jr., J. E. Peralta, F. Ogliaro, M. J. Bearpark, J. J. Heyd, E. N. Brothers, K. N. Kudin, V. N. Staroverov, T. A. Keith, R. Kobayashi, J. Normand, K. Raghavachari, A. P. Rendell, J. C. Burant, S. S. Iyengar, J. Tomasi, M. Cossi, J. M. Millam, M. Klene, C. Adamo, R. Cammi, J. W. Ochterski, R. L. Martin, K. Morokuma, O. Farkas, J. B. Foresman, D. J. Fox Gaussian 16 Revision B.01, Gaussian Inc., Wallingford CT. **2016**.

14.   Choi, J.; Kim, H., Spin-Flip Density Functional Theory for the Redox Properties of Organic Photoredox Catalysts in Excited States. *J Chem Theory Comput* **2021,** *17* (2), 767-776.

15.   Ho, J., Are thermodynamic cycles necessary for continuum solvent calculation of pKas and reduction potentials? *Phys Chem Chem Phys* **2015,** *17* (4), 2859-68.

16.   Cerezo, J.; Santoro, F., FCclasses3: Vibrationally-resolved spectra simulated at the edge of the harmonic approximation. *J Comput Chem* **2023,** *44* (4), 626-643.

17.   Avila Ferrer, F. J.; Santoro, F., Comparison of vertical and adiabatic harmonic approaches for the calculation of the vibrational structure of electronic spectra. *Phys Chem Chem Phys* **2012,** *14* (39), 13549-63.

18.   Neese, F., The ORCA Program System. *Wiley Interdiscip. Rev.: Comput. Mol. Sci.* **2012,** *2*, 73–78.

19.   Neese, F., Software update: The ORCA program system—Version 5.0. *WIREs Computational Molecular Science* **2022,** *12* (5).

20.   Neese, F., Efficient and accurate approximations to the molecular spin-orbit coupling operator and their use in molecular g-tensor calculations. *J Chem Phys* **2005,** *122* (3), 34107.

21.   Ohkubo, K.; Fujimoto, A.; Fukuzumi, S., Metal-free oxygenation of cyclohexane with oxygen catalyzed by 9-mesityl-10-methylacridinium and hydrogen chloride under visible light irradiation. *Chem Commun (Camb)* **2011,** *47* (30), 8515-7.

22.   Ohkubo, K.; Mizushima, K.; Fukuzumi, S., Oxygenation and chlorination of aromatic hydrocarbons with hydrochloric acid photosensitized by 9-mesityl-10-methylacridinium under visible light irradiation. *Res. Chem. Intermed.* **2013,** *39*, 205–220.

23.   Oh, S.; Stache, E. E., Chemical Upcycling of Commercial Polystyrene via Catalyst-Controlled Photooxidation. *J. Am. Chem. Soc.* **2022,** *144* (13), 5745-5749.

24.   Qin, Y.; Zhang, T.; Ching, H. Y. V.; Raman, G. S.; Das, S., Integrated strategy for the synthesis of aromatic building blocks via upcycling of real-life plastic wastes. *Chem* **2022,** *8* (9), 2472-2484.

25.   Huang, Z.; Shanmugam, M.; Liu, Z.; Brookfield, A.; Bennett, E. L.; Guan, R.; Vega Herrera, D. E.; Lopez-Sanchez, J. A.; Slater, A. G.; McInnes, E. J. L.; Qi, X.; Xiao, J., Chemical Recycling of Polystyrene to Valuable Chemicals via Selective Acid-Catalyzed Aerobic Oxidation under Visible Light. *J. Am. Chem. Soc.* **2022,** *144* (14), 6532-6542.

26.   Li, T.; Vijeta, A.; Casadevall, C.; Gentleman, A. S.; Euser, T.; Reisner, E., Bridging Plastic Recycling and Organic Catalysis: Photocatalytic Deconstruction of Polystyrene via a C–H Oxidation Pathway. *ACS Catal* **2022,** *12* (14), 8155-8163.

27.   Cao, R.; Zhang, M.-Q.; Hu, C.; Xiao, D.; Wang, M.; Ma, D., Catalytic oxidation of polystyrene to aromatic oxygenates over a graphitic carbon nitride catalyst. *Nat Commun.* **2022,** *13* (1), 4809.

28.   Peng, Z.; Chen, R.; Li, H., Heterogeneous Photocatalytic Oxidative Cleavage of Polystyrene to Aromatics at Room Temperature. *ACS Sustainable Chem. Eng.* **2023,** *11* (29), 10688-10697.